Title

Selective Oxide Pulsed Chemical Vapor Deposition for Dielectric on Metal and Dielectric on Dielectric

Author

Huang, James

Publication Date

2023

Peer reviewed|Thesis/dissertation

UNIVERSITY OF CALIFORNIA SAN DIEGO

Selective Oxide Pulsed Chemical Vapor Deposition for Dielectric on Metal and Dielectric on Dielectric

A Dissertation submitted in partial satisfaction of the requirements
for the degree Doctor of Philosophy

in

Materials Science and Engineering

by

James Huang

Committee in charge:

Professor Andrew C. Kummel, Chair
Professor Prabhakar Bandaru
Professor Michael Burkart
Professor Yu-Hwa Lo

2023

The Dissertation of James Huang is approved, and it is acceptable in quality and form for publication on microfilm and electronically.

University of California San Diego

2023

DEDICATION

I dedicate this thesis to my parents and mentors for their love and support, with the hope that this achievement fills them with pride.

TABLE OF CONTENTS

LIST OF FIGURES

ACKNOWLEDGEMENTS

I would like to convey my deep appreciation to Professor Andrew C. Kummel, whose mentorship and guidance have been of immeasurable value throughout the years. I am grateful for the abundant learning opportunities (equipment training, conferences, etc.) you have offered. I hold a deep appreciation for your exceptional talent in extrapolating valuable applications from our less favorable results, and I am steadfastly committed to maintaining a strong work ethic under your influential mentorship.

I would also like to extend my gratitude to my senior student, Yunil Cho, for his guidance and support during my initiation into selective oxide chemical vapor depositions. I would like to extend a similar expression of gratitude to my junior student, Jing Mu, for his diligent work and dedication. Thanks to his hard work, I was able to complete my third paper within the designated timeframe.

Similar appreciation goes towards all my lab mates with whom I have had the pleasure of working together: Dr. Christopher Ahles, Dr. Scott T. Ueda, Dr. Yunil Cho, Dr. Seongyuk Yun, Dr. Dohyun Go, Dr. Dipayan Pal, Dr. Zichen Zhang, Dr. Aaron Mcleod, Jing Mu, Xinyu Wang, Jimmy Kuo, Jannick Fammels, Harshil Kashyap, Ping-Che Lee, Jacob Watson, and Emily Thomson. Special thanks to Victor Wang, thank you for your friendship and support throughout my Ph.D. studies. Thank you for your introduction to the lab on the first day I joined the group. I look forward to working together with you next January.

The completion of this comprehensive research project was made possible through the generous support of our industry partner, Applied Materials. Finally, I would like to extend my sincere appreciation to my esteemed committee members: Dr. Prabhakar Bandaru, Dr. Michael Burkart, and Dr. Yu-Hwa Lo, for their active involvement and flexibility in ensuring

a seamless scheduling of my examinations. Their invaluable guidance and insightful critiques of my work have greatly contributed to its quality.

Chapter 1, in full, is a reprint of the material as it appears in the following publication:

Huang, J.; Cho, Y.; Zhang, Z.; Jan, A.; Wong, K. T.; Nemani, S. D.; Yieh, E.; Kummel, A. C. (2022). Selective Pulsed Chemical Vapor Deposition of Water-Free TiO2/Al2O3 and HfO2/Al2O3 Nanolaminates on Si and SiO_2 in Preference to SiCOH. ACS Applied Materials and Interfaces, 14(13), 15716–15727. https://doi.org/10.1021/acsami.1c19810.

The dissertation author was the primary investigator and author of this paper.

Chapter 2, in full, is a reprint of the material as it appears in the following publication:

Huang, J., Cho, Y., Wang, V., Zhang, Z., Mu, J., Yadav, A., Wong, K., Nemani, S., Yieh, E., & Andrew, K. (2023). Dielectric-on-Dielectric Achieved on SiO_2 in Preference to W by Water-free Chemical Vapor Depositions with Aniline Passivation. *ACS Applied Materials & Interfaces*, *15*(21), 26128–26137. https://doi.org/10.1021/acsami.3c02278.

The dissertation author was the primary researcher and author of this paper.

Chapter 3, in full, is a reprint of the material which has been submitted to ACS Applied Materials & Interfaces for publication:

Huang, J., Mu, J., Cho, Y., Winter, C., Wang, V., Zhang, Z., Wang, K., Kim, C., Yadav, A., Wong, K., Nemani, S., Yieh, E., & Kummel, A. (2023). Low-k SiOx/AlOx Nanolaminate Dielectric on Dielectric Achieved by Hybrid Pulsed Chemical Vapor Deposition. *ACS Applied Materials & Interfaces*, *0*(0). https://doi.org/10.1021/acsami.3c13973

The dissertation author was the primary researcher and author of this paper.

VITA

2017 Bachelor of Engineering in Materials Engineering, University of Toronto

2019 Master of Science in Materials Engineering, Columbia University

2023 Doctor of Philosophy in Materials Science and Engineering, University of California San Diego

PUBLICATIONS

Huang, J.; Cho, Y.; Zhang, Z.; Jan, A.; Wong, K. T.; Nemani, S. D.; Yieh, E.; Kummel, A. C. (2022). Selective Pulsed Chemical Vapor Deposition of Water-Free TiO2/Al2O3 and HfO2/Al2O3 Nanolaminates on Si and SiO_2 in Preference to SiCOH. ACS Applied Materials and Interfaces, 14(13), 15716–15727. https://doi.org/10.1021/acsami.1c19810.

Huang, J., Cho, Y., Wang, V., Zhang, Z., Mu, J., Yadav, A., Wong, K., Nemani, S., Yieh, E., & Kummel, A. (n.d.). Dielectric-on-Dielectric Achieved on SiO_2 in Preference to W by Water-free Chemical Vapor Depositions with Aniline Passivation. *ACS Applied Materials & Interfaces*, *15*(21), 26128–26137. https://doi.org/10.1021/acsami.3c02278.

Huang, J., Mu, J., Cho, Y., Winter, C., Wang, V., Zhang, Z., Wang, K., Kim, C., Yadav, A., Wong, K., Nemani, S., Yieh, E., & Kummel, A. (2023). Low-k SiOx/AlOx Nanolaminate Dielectric on Dielectric Achieved by Hybrid Pulsed Chemical Vapor Deposition. *ACS Applied Materials & Interfaces*, *0*(0). https://doi.org/10.1021/acsami.3c13973

Kuo, C.-H., McLeod, A., Lee, P., **Huang, J.**, Kashyap, H., Wang, V., Yun, S., Zhang, Z., Spiegelman, J., Kanjolia, R., Moinpour, M., & Kummel, A. (n.d.). Low-Resistivity Titanium Nitride Thin Films Fabricated by Atomic Layer Deposition with $TiCl_4$ and Metal–Organic Precursors in Horizontal Vias. *ACS Applied Electronic Materials*, *5*(8), 4094–4102. https://doi.org/10.1021/acsaelm.3c00245.

Cho, Y., **Huang, J.**, Ahles, C. F., Zhang, Z., Wong, K., Nemani, S., Yieh, E., & Kummel, A. C. (2022). Inherent selective pulsed chemical vapor deposition of amorphous hafnium oxide / titanium oxide nanolaminates. *Applied Surface Science*, *600*, 154010. https://doi.org/10.1016/J.APSUSC.2022.154010.

Cho, Y., Ahles, C., Choi, J. Y., **Huang, J.**, Jan, A., Wong, K., Nemani, S., Yieh, E., & Kummel, A. (n.d.). Inherently Selective Water-Free Deposition of Titanium Dioxide on the Nanoscale: Implications for Nanoscale Patterning. *ACS Applied Nano Materials*, *5*(1), 476–485. https://doi.org/10.1021/acsanm.1c03311.

Cho, Y., **Huang, J.**, Zhang, Z., Wang, K., Lee, P., Kim, C., Wong, K., Nemani, S., Yieh, E., & Kummel, A. C. (2023). Inherent selective pulsed chemical vapor deposition of aluminum

oxide in nm scale. *Applied Surface Science*, *622*, 156824. https://doi.org/10.1016/j.apsusc.2023.156824.

Zhang, Z., Passlack, M., Pitner, G., Kuo, C.-H., Ueda, S., **Huang, J.**, Kashyap, H., Wang, V., Spiegelman, J., Lam, K.-T., Liang, Y.-C., Liew, S., Hsu, C., Kummel, A., & Bandaru, P. (n.d.). Sub-Nanometer Interfacial Oxides on Highly Oriented Pyrolytic Graphite and Carbon Nanotubes Enabled by Lateral Oxide Growth. *ACS Applied Materials & Interfaces*, *14*(9), 11873–11882. https://doi.org/10.1021/acsami.1c21743.

S. Kahn, J., Xiong, Y., **Huang, J.**, & Gang, O. (2022). Cascaded Enzyme Reactions over a Three-Dimensional, Wireframe DNA Origami Scaffold. *JACS Au*, *2*(2), 357–366. https://doi.org/10.1021/jacsau.1c00387.

Xiong, Y., **Huang, J.**, Wang, S.-T., Zafar, S., & Gang, O. (2020). Local Environment Affects the Activity of Enzymes on a 3D Molecular Scaffold. *ACS Nano*, *14*(11), 14646–14654. https://doi.org/10.1021/acsnano.0c03962.

FIELD OF STUDY

Major Field: Materials Science and Engineering
Studies in Selective Oxide Deposition
Professor Andrew C. Kummel

ABSTRACT OF THE DISSERTATION

Selective Oxide Pulsed Chemical Vapor Deposition for Dielectric on Metal and Dielectric on Dielectric

by

James Huang

Doctor of Philosophy in Materials Science and Engineering

University of California San Diego, 2023

Professor Andrew C. Kummel, Chair

The semiconductor industry continues to pursue the scaling of three-dimensional integrated circuits (ICs), achieved by reducing the size of devices and interconnects. This downsizing of IC components enhances performance and reduces power consumption by shortening interconnect lengths. However, as ICs scale down to nanometer dimensions, issues related to patterning mask misalignment and interconnect misalignment become prominent. Mask misalignment can cause mask pattern transfer defects and pattern transfer in low

resolution. In order to address the problem of mask misalignment, Bencher et al. introduced the concept of self-aligned chemical vapor deposition (CVD), also known as area-selective CVD [1]. This method has since evolved into a self-aligned quadruple patterning technique in recent years [2]. The core idea involves selectively depositing a spacer or etch stop material onto the preferred locations within a pre-etched structure, effectively halving the pitch of the integrated circuit. Interconnect misalignment can result in undesired short-circuits and capacitive coupling between vias and metal lines. Chen et al. have shown that the issue of misalignment can be effectively resolved using the dielectric on dielectric (DOD) deposition method [3]. This process requires selective deposition of a dielectric buffer layer onto the existing dielectric, giving it preference over the metal component. The selective dielectric layer effectively increases the separation between misaligned vias and the adjacent metal lines, thereby enhancing performance in terms of reducing short-circuits, capacitive coupling, and mitigating time-dependent dielectric breakdown (TDDB) [3].

In Chapter 1, this work is an extension of our prior research efforts. Selective TiO_2/Al_2O_3 and HfO_2/Al_2O_3 pulsed CVD were investigated on Si, SiO2 and SiCOH substrates, where SiCOH is a methyl terminated Si substrate provided by Applied Materials. In this study, TMA was discovered to improve the selectivity of both nanolaminates on Si, SiO_2 in preference to SiCOH. Dielectric on metal was also achieved on the copper region of a nanoscale copper/SiCOH patterned sample. These selective nanolaminates can be a strong candidate for the spacer or etch stop layer in self-aligned double or quadruple patterning method.

In Chapter 2, with the help of aniline, TiO_2, HfO_2, and Al_2O_3 were able to selectively deposit on SiO_2 substrate in preference to W substrate. Selective deposition at the nanoscale was also demonstrated on a patterned W/SiO_2 sample with a pitch size of 55 nanometers. The

deposited thin films exhibit a consistent smoothness and uniformity across the entire sample. The selection between HfO_2 and Al_2O_3 processes for dielectric on dielectric (DOD) can be customized based on the intended application and the specific target dielectric constant (k value).

Chapter 3 describes selective nanolaminate pulsed CVD using Aluminum-tri-sec-butoxide (ATSB) together with Tris(tert-butoxy) Silanol (TBS) to achieve AlO_x/SiO_x nanolaminate DOD on SiO2 substrate in preference to W substrate. 3 nanometer selectivity was achieved with 50 pulses ATSB at 330°C and 60s TBS at 200°C per supercycle. By following this supercycle procedure, a 28-nanometer low-k nanolaminate was obtained after 14 supercycles, resulting in a dielectric constant of 3.3. With 25 pulses ATSB at 330°C and 60s TBS at 200°C per supercycle, a low k nanolaminate with a dielectric constant of 2.5 was achieved.

1. Bencher, C.; Chen, Y.; Dai, H.; Montgomery, W.; Huli, L. 22nm Half-Pitch Patterning by CVD Spacer Self Alignment Double Patterning (SADP). *Opt. Microlithogr. XXI* **2008**, *6924* (March 2008), 69244E. https://doi.org/10.1117/12.772953.

2. Juncker, A.; Clark, W.; Vincent, B.; Franke, J.-H.; Halder, S.; Lazzarino, F.; Murdoch, G. Self-Aligned Block and Fully Self-Aligned via for IN5 Metal 2 Self-Aligned Quadruple Patterning. *SPIE Adv. Lithogr.* **2018**, No. March 2018, 29. https://doi.org/10.1117/12.2298761.

3. Chen, H.; Wu, Y.; Huang, H.; Tsai, C.; Lee, S.; Lee, C.; Wei, T.; Yao, H.; Wang, Y.; Liao, C.; Chang, H.; Lu, C.; Shue, W.; Cao, M. Fully Self-Aligned Via Integration for Interconnect Scaling Beyond 3nm Node. *2021 IEEE International Electron Devices Meeting (IEDM)*, 2021, pp. 22.1.1-22.1.4, doi: 10.1109/IEDM19574.2021.9720600.

Chapter 1 Selective Pulsed Chemical Vapor Deposition of Water-free TiO_2/Al_2O_3 and HfO_2/Al_2O_3 Nanolaminates on Si and SiO_2 in Preference to SiCOH

1.1 Introduction

Ultraviolet (UV) photolithography technology is one of the key components in the semiconductor industry. Advancement in transistor density of integrated circuits (ICs) can be partially attributed to the improvement in the UV photolithography process [1-2]. When scaling down the size of a metal oxide semiconductor field effect transistor (MOSFET), mask misalignment became one of the major limitations of UV photolithography [3-6]. To solve the issue of mask misalignment, Bencher et al. proposed the self-aligned chemical vapor deposition (CVD) (or area-selective CVD) spacer double patterning method which has evolved to a self-aligned quadruple patterning method in recent years [7-8]. The spacer or etch stop material when selectively deposited onto the preferred locations of a pre-etched structure, allows the pitch of the IC to be reduced by half. Since then, area-selective CVD (AS-CVD) has garnered attention as an alternative patterning method.

Previously, TiO_2 HfO_2 and Al_2O_3 were demonstrated to be possible spacers or etch stop layers in self-aligned patterning [9]. HfO_2 and Al_2O_3 can also act as diffusion barriers for Cu interconnects as demonstrated by Majumder et al. [10]. In recent study by Chen et al., TiO_2 is reported to be a strong candidate for dielectric-on-dielectric CVD to achieve self-aligned via integration with alkanethiol self-assembly monolayers (SAMs) for selective deposition [11].

CVD process normally involves one or more gas phase precursors reacting near the substrate surface [12]. For thermal CVD, the focus of the present study, gas phase precursors physisorb onto the substrate surface and potentially chemisorb with a reactive site such as a hydroxyl group (OH^-). Due to high surface temperature, the chemisorbed precursors will undergo

decomposition and may form new reactive (OH^-) sites. This leads to continuous deposition without a self-limiting step, but pulsed CVD can result in self-limiting adsorption since the physisorption process can be limited to a single monolayer.

AS-CVD can be achieved by three methods: inherent selectivity, selective passivation, and selective activation [13-15]. Inherent selectivity is the most desired since it is economically feasible and undemanding; in this process, selectivity was achieved by the difference in reactivity between two substrate surfaces. Conversely, selective passivation and selective activation require one extra step of passivant (or activant) deposition.

In the present study, inherently AS-CVD was achieved by utilizing the difference in surface reactivity (for example, the number of Si-OH or Si-H sites) between Si, SiO_2 and alkyl (CH_3^-) terminated Si (SiCOH). Selectivity was defined by the following equation and evaluated when the film thickness on SiCOH approached 0.3 nm, which is less than one monolayer [16] :

$$Selectivity = \frac{film\ thickness\ on\ Si}{film\ thickness\ on\ SiCOH}$$

In our earlier works, selective water-free single precursor TiO_2 and HfO_2 pulsed CVD deposition on Si, SiO_2, and SiCOH were studied [17,18]. SiCOH is an unreactive surface but requires a water-free process to avoid hydroxylation which can result in both loss of selectivity and substrate oxidation.

At 300 °C, water-free TiO_2 pulsed CVD was achieved by pulsed dosing of titanium isopropoxide ($Ti(O^iPr)_4$) precursor instead of continuous flow. HfO_2 water-free pulsed CVD at 300 °C has been studied by Cho et al. using hafnium tert-butoxide ($Hf(O^tBu)_4$) as the single precursor. When pulsed gas-phase $Ti(O^iPr)_4$ precursor adsorbs onto the substrate surface, it decomposes into TiO/TiOH and OiPr/iPr ligand. TiO/TiOH will chemisorb onto the substrate (OH^-) and (H^+) sites while remaining ligands will be removed during the nitrogen gas purging ½ cycle.

Sequential pulses of $Ti(O^iPr)_4$ are expected to follow the same mechanism and form TiO_2 layers. The use of multiple short pulses instead of longer pulses affords the ligands time to desorb and the physisorbed precursor on non-reactive surfaces time to desorb.

Optimization of the pulsed single precursor CVD process (substrate time and pulse lengths) increases selectivity and prevents gas phase reaction and uncontrollable growth rate [18]. Around 17 nm and 40 nm TiO_2 were selectively deposited on Si and SiO_2 in preference to SiCOH ($\leq$0.5 nm) with a selectivity of 34 on the Si surface [17]. Pulsed water-free $Hf(O^tBu)_4$ CVD proceeds by a similar mechanism and deposited 1.8 nm and 5 nm of HfO_2 on Si and SiO_2 in preference to SiCOH (0.13 nm) with a selectivity of 14 on Si vs SiCOH [18]. Note, the selectivity was greater for SiO_2 vs Si but was quantified for Si vs SiCOH since the thickness was more accurately measured by ellipsometry on Si. However, despite of the superior selectivity, the deposited TiO_2 films showed high surface roughness due to crystallization (shown in Fig. 1.13). This is non-ideal for high-density MOSFET devices.

A TiO_2/Al_2O_3 nanolaminate structure on Si was previously demonstrated by Testoni et al. to be free of nanocrystallites because Al_2O_3 cannot crystalize at normal ALD or CVD temperatures and crystallization is impeded for TiO_2 [19]. This nanolaminate structure was accomplished by employing atomic layer deposition (ALD) supercycles of $Ti(O^iPr)_4$ with H_2O and trimethyl aluminum (TMA) with H_2O [19]. Later, Ylivaara et al. studied the growth and mechanical properties of TiO_2/Al_2O_3 nanolaminate ALD using $TiCl_4$ and TMA with H_2O as the co-reactant [20]. Yang et al. showed that HfO_2/Al_2O_3 nanolaminate had better electrical properties than just pure HfO_2 or Al_2O_3 [21].

Even though there have been many studies about the electrical, mechanical, and even optical properties of TiO_2, HfO_2 and their nanolaminates with Al_2O_3, little is known about the

water-free TiO_2/Al_2O_3 and HfO_2/Al_2O_3 nanolaminates pulsed AS-CVD processes and their selectivity performance [22-27]. Our group previously reported the selectivity and surface smoothness of a water-free HfO_2/TiO_2 nanolaminate pulsed CVD [28]. The nanolaminate structure was found to be the key factor that can impede the formation of nanocrystallites if the sublayer is about 1.5 nm (a schematic nanolaminate illustration is shown in Fig. 1.1) [28]. However, there was a large selectivity difference between pure HfO_2 and pure TiO_2 pulsed CVD deposition which leads to a reduced (~16 nm with highest TiO_2 ratio) selective HfO_2/TiO_2 nanolaminate deposition on Si in preference to SiCOH [28].

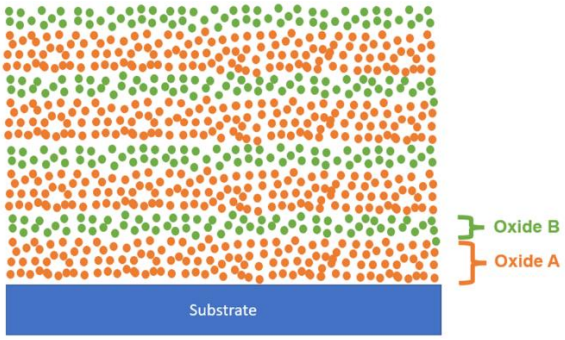

Figure 1.1 A schematic diagram showing a nanolaminate structure with alternating oxide A and oxide B sublayers.

TMA is a well-studied precursor used with an oxidant co-reactant for Al_2O_3 CVD [29]. Al in TMA is a strong electron donor which favors bond formation with oxygen, a strong electron acceptor [19, 30]. TMA can act as an oxygen ((OH^-) group) scavenger and is a possible solution to achieve both high selectivity and film smoothness [31]. In the present study, it is shown that TMA enhances the selectivity and film smoothness of both TiO_2 and HfO_2 water-free pulsed CVD in nanolaminate stacks. Experiments were carried out at 300 °C which is the optimized dosing temperature calibrated for HfO_2 and TiO_2 thermal CVD processes [17, 18]. At 300 °C, both TiO_2/Al_2O_3 and HfO_2/Al_2O_3 nanolaminates were deposited by supercycles of $Ti(O^iPr)_4/Hf(O^tBu)_4$ with TMA subcycles. The sublayers are designed to be about 1 nm in thickness to prevent

nanocrystallite formation in the HfO_2 or TiO_2 sublayers. The optimal supercycles consisted of 200 pulses $Ti(O^iPr)_4$ with 1 pulse of TMA and 12 pulses $Hf(O^tBu)_4$ with 1 pulse of TMA. Compared with single precursor TiO_2 pulsed CVD, for TiO_2/Al_2O_3 nanolaminates, selectivity on hydrofluoric acid (HF) cleaned Si vs SiCOH increased from 34 to 44 while RMS roughness of the film decreased from 2.8 nm to 0.38 nm. For HfO_2/Al_2O_3 nanolaminates, the selectivity for Si vs SiCOH increased from 13.8 to 73 and the films roughness was 0.78 nm. With the above supercycle recipes, nanoselectivity was also demonstrated on a Cu/SiCOH patterned sample.

The novelty of this paper is that a nanolaminate structure is used not only to mitigate nanocrystallites formation but also to improve the selectivity with the help of TMA. TMA is not just used as a precursor in this research but an additive to enhance smoothness and selectivity. This opens up the possibility for future dielectric nanolaminate fabrication.

1.2 Experimental Section

B-doped Si (0 0 1), SiO_2, SiCOH and a Cu/SiCOH patterned samples were used as the substrate materials. All substrates underwent a degreasing process using acetone, methanol and HPLC water sequentially for 10 s each. A N_2 air gun was used to remove residual aqueous solution on the substrate surface. For Si and SiO_2, after the degreasing process, an extra 30 s 0.5% hydrofluoric acid (HF) clean followed by a HPLC water rinse was conducted. Afterwards, the samples were loaded via a load lock into the deposition system.

SiCOH and Cu/SiCOH samples were obtained from Applied Materials (black diamond trade name). This SiCOH is a non-porous insulator. The SiCOH employed the present study had 70 nm (80 nm before CMP) thickness, a dielectric constant of 2.9, 20% carbon content and ALD TaN with Co as the diffusion barrier material. The water contact angle for SiCOH was 82 degrees before passivation and 88 degrees after passivation (see below).

For the Cu/SiCOH samples received from Applied Materials, the pitch size was ~90 nm and the average linewidth was ~45nm. Patterned SiCOH surface methyl groups can be damaged by plasma etching, UV lithrography, and even diffusion barrier sputtering processes which results in formation of Si-H, Si-OH and Si dangling bonds on the surface [32-36]. Similar to the silylation repair (forming a Si-O-CH_3 bond) demonstrated by Oszinda et al., passivation (damage repair) was performed using a proprietary process from Applied Materials to restore surface methyl concentration [36]. Degreased SiCOH samples were also passivated by this method as controls.

A custom-built vacuum chamber system was used for the CVD study (see chamber schematic diagram Fig. 1.12). It consists of four vacuum chambers: load-lock chamber (for sample loading), CVD reaction chamber, and two ultra-high vacuum (UHV) chambers. Two or three samples (i.e. passivated Cu/SiCOH and passivated SiCOH or HF-cleaned Si, SiO_2 and degreased only SiCOH) were simultaneously loaded into the load-lock chamber. Therefore, a direct comparison of the nanolaminate CVD deposition thickness can be achieved for accurate selectivity measurements. A reaction chamber with a base pressure of $3x10^{-7}$ Torr was used for all the experiments. This reaction chamber was pumped by a Pfeiffer TPU 062 turbo pump with backing by an Edwards RV3 rotary pump. There was a manipulator with a copper sample holder mounting platform inside the reaction chamber. A cartridge heater was inserted into this manipulator and used as a heat source during the CVD process. A N_2 purge line, TMA dosing line, $Hf(O^tBu)_4$ dosing line and $Ti(O^iPr)_4$ dosing line were connected to the reaction chamber and pointed at the sample stage at a distance of 3 inches. Hafnium *tert*-butoxide ($Hf(O^tBu)_4$, 99.99%) and Titanium isopropoxide ($Ti(O^iPr)_4$, 99.99%), were both purchased from Sigma Aldrich. Trimethyl aluminum (TMA, 98%) was purchased through Strem Chemicals.

Each dosing line contains at least one pneumatic ALD valve and a shut off valve. $Hf(O^tBu)_4$ dosing line used two pneumatic to form a fixed volume to have better pressure control. For the N_2 purge line with a mass flow controller, an extra leak valve was installed to control its pressure. Reaction chamber wall and the dosing lines were wrapped with heat tape and kept at 150 °C. No push gas was employed for any of the precursors. Samples were pre-annealed to 300 °C in UHV chamber before transferring to the ALD/CVD reaction chamber.

For the TiO_2/Al_2O_3 CVD reaction, the sample stage was heated up to 300 °C. The $Ti(O^iPr)_4$ precursor bottle was kept at room temperature. For a supercycle, after a desired number of $Ti(O^iPr)_4$ pulses, one pulse of TMA was dosed. During the CVD process, continuous flow of N_2 purge gas was implemented. There were 60 s purge before and after each TMA pulse to prevent gas phase reactions. In addition, continuous flow of N_2 purge gas was also implemented.

For the HfO_2/Al_2O_3 CVD reaction at 300 °C, the $Hf(O^tBu)_4$ precursor bottle was heated to 36 °C. The $Hf(O^tBu)_4$ source had two pneumatic valves to reduce the dose pressure. Both pneumatic valves have an opening time of 500 ms. After the first pneumatic valve opening, $Hf(O^tBu)_4$ gas flowed into a constant volume container; afterward, the first pneumatic valve was closed, and the gas was trapped for 10 s followed by the second pneumatic valve opening. Between each constant volume pulse, there is a 60 s N_2 purge in the reaction chamber. After desired number of $Hf(O^tBu)_4$ pulses, there was a 60 sec N_2 purge, a 15 ms TMA dose, and a 60 sec N_2 purge. In addition, continuous flow of N_2 purge gas was also implemented.

After deposition, samples were transferred *in-vacuo* to the UHV chamber where the X-ray photoelectron spectroscopy (XPS) was performed. For the XPS, a monochromatic Al Kα X-ray source (E = 1487 eV) and a hemispherical analyzer (XM 1000 MkII/SPHERA, Omicron Nanotechnology) with a pass energy of 50 eV was employed. The XPS anode voltage was set to

10 kV, and the filament emission current was set to 25 mA. For surface characterization, the XPS detector was aligned to 60° (glancing angle) from the sample surface normal. This angle was changed to 30° (normal angle) for bulk deposition compositional analysis. All XPS data was collected and analyzed by Casa XPS v2.3 program. *Ex-situ* atomic force microscopy (AFM – Agilent 5500) was employed to study the sample surface morphology. For cross-sectional studies, samples focus ion beam (FIB) and transmitted electron microscopy (TEM) were performed.

1.3 Results and Discussion

TMA as reactive site scavenger and selectivity promoter

Water-free TiO_2/Al_2O_3 and HfO_2/Al_2O_3 pulsed CVD were performed on HF cleaned Si, HF cleaned SiO_2 and degreased SiCOH samples. HF-cleaned Si had its surface native oxide removed and had an Si-H terminated surface [37]. HF-cleaned SiO_2 and degreased SiCOH had Si-OH terminated and Si-CH_3 terminated surfaces respectively [18]. From previous HfO_2/TiO_2 nanolaminate studies, thinner sublayers were known to prevent nanocrystallites formation [28]. A monolayer thickness of TiO_2 sublayer requires approximately 30 pulses of $Ti(O^iPr)_4$ (0.009 nm/pulse was calculated based on the single precursor TiO_2 pulsed CVD shown in Fig. 1.13) [17]. Consequently, the initial supercycle was composed of 30 pulses of $Ti(O^iPr)_4$ followed by 1 pulse of TMA 300 °C.

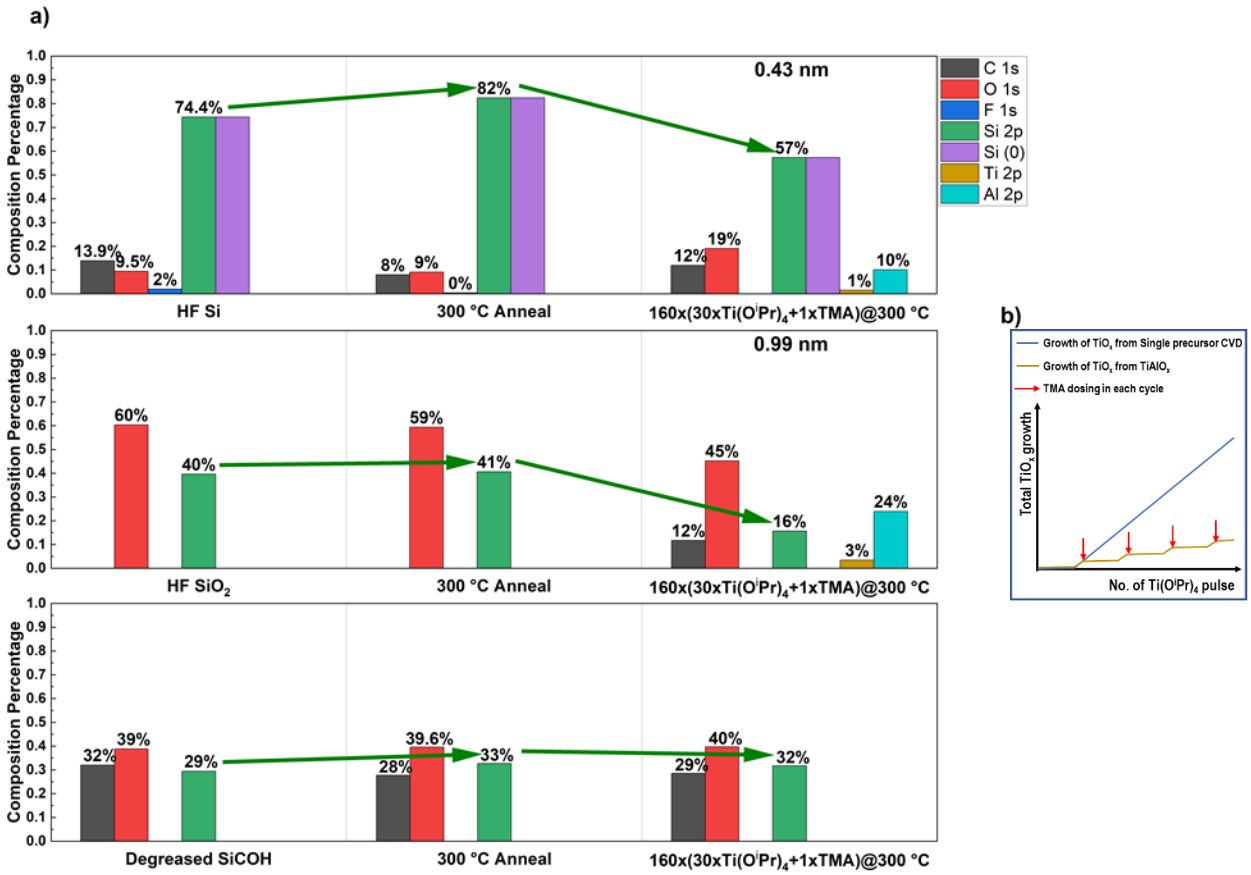

Figure 1.2. XPS study of nucleation for Ti/AlO_x pulsed CVD. (a) XPS shows little to no growth of Ti/AlO_x CVD with 30 pulses of $Ti(O^iPr)_4$ followed by 1 pulse of TMA as a supercycle on HF-cleaned Si, SiO_2 and degreased SiCOH samples. XPS raw data can be found in support information Fig. 1.14. (b) Heuristic model of the TiO_2 growth shows that TMA acting as a passivant in each supercycle suppressing the growth rate. Note these growth rates are just rough approximations for illustration.

Fig. 1.2 (a) shows the XPS chemical composition of HF cleaned Si, SiO_2 and degreased SiCOH as loaded, after 300 °C rapid anneal, and after the pulsed CVD deposition. Since all samples were pre-annealed to the CVD temperature before deposition, a 300 °C 1 second rapid anneal was conducted and studied to determine the change in chemical composition by XPS. After the 300 °C rapid anneal, XPS data showed that carbon percent for HF-cleaned Si and degreased SiCOH decreased from 14% to 8% and 32% to 28%, respectively. This indicates partial desorption of surface carbon. With less surface carbon, the Si signal from HF-cleaned Si and degreased SiCOH increases.

After 160 supercycles of 30 pulses of $Ti(O^iPr)_4$ followed by 1 pulse of TMA, the Si decreases from 82% to 57%, 41% to 16% on HF-cleaned Si and SiO_2 respectively while degreased SiCOH shows no attenuation of the Si signal. XPS also shows ~10% and ~24% of Al, ~1% and ~3% of Ti on HF-cleaned Si and SiO_2. Based on the equation between the inelastic mean free path and the attenuation length of an electron from the Si substrate (Si signal attenuation), around 0.43 nm and 0.99 nm TiO_2/Al_2O_3 were calculated to have been deposited on HF-cleaned Si and SiO_2. The TiO_2/Al_2O_3 thicknesses are much less than the thickness estimated from TiO_2 single precursor pulsed CVD with the same $Ti(O^iPr)_4$ total pulse length. The data is consistent with TMA being the cause for this nucleation prolongation; a simplified model is shown in Fig 1.2 (b).

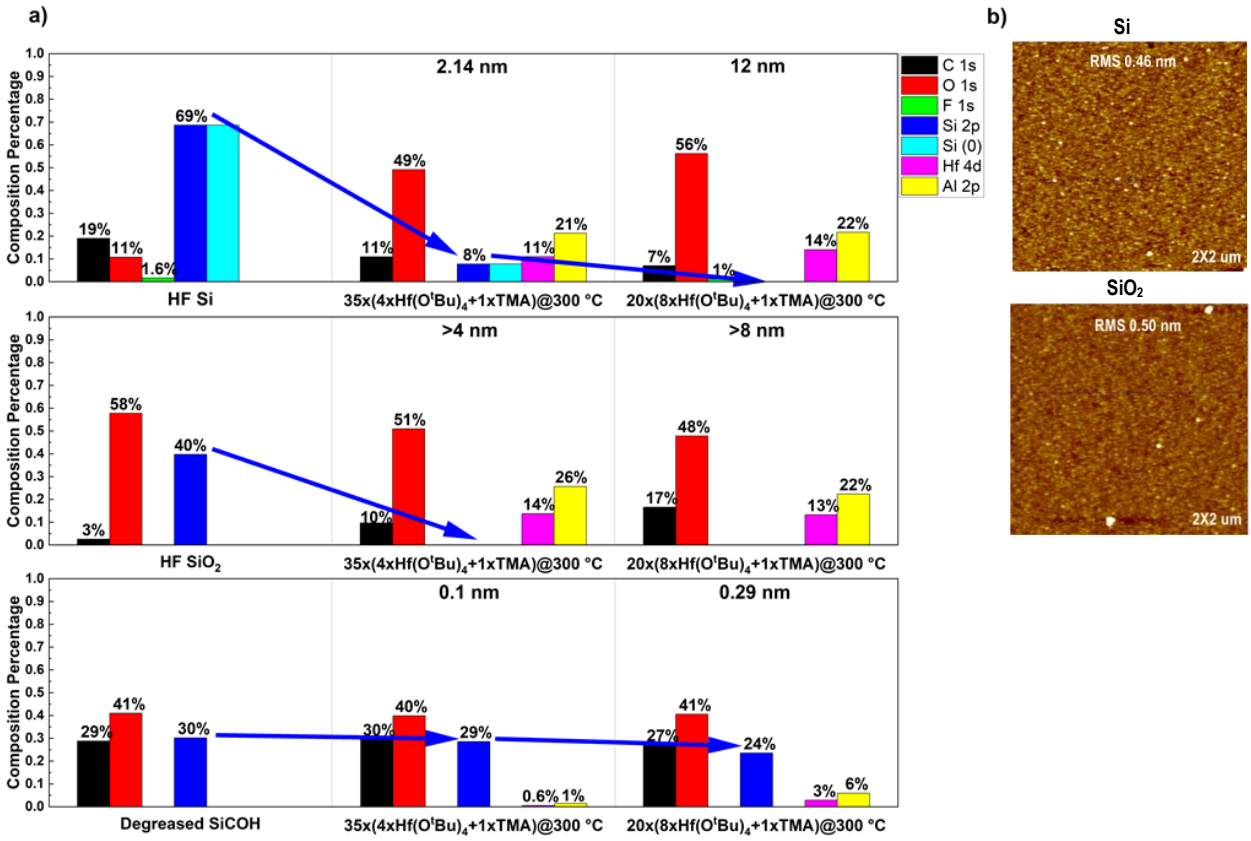

Figure 1.3. XPS study of nucleation for Hf/AlO_x pulsed CVD. (a) XPS shows the growth suppression by TMA with 4 pulses of $Hf(O^tBu)_4$ in each supercycle while 8 pulses of $Hf(O^tBu)_4$ per supercycle renders a higher selectivity than pure HfO_2 single precursor CVD. Raw data is shown in supplementary information Fig. 1.15. (b) Both AFM images on Si and SiO_2 samples show generally smooth film surfaces with RMS roughness of 0.46 nm and 0.50 nm, respectively.

For HfO_2/Al_2O_3, the initial supercycle had 4 pulses of $Hf(O^tBu)_4$ followed by 1 pulse of TMA. XPS of HfO_2/Al_2O_3 on HF-cleaned Si, SiO_2 and degreased SiCOH is shown in Fig. 1.3 (a). After a total of 35 supercycles (equivalent of 140 Hf pulses), around 2.14 nm, >4 nm and only 0.1 nm of HfO_2/Al_2O_3 were deposited on HF-cleaned Si, SiO_2 and degreased SiCOH, respectively. Compared with previous HfO_2 300 °C pulsed CVD selectivity study (shown in Fig. 1.16), the same total pulse length of $Hf(O^tBu)_4$ results in a thinner film with TMA as a co-reactant. Next, 20 supercycles were deposited consisting of 8 pulses of $Hf(O^tBu)_4$ followed by 1 pulse of TMA to increase the Hf/Al ratio. Around 12 nm, >8 nm and only 0.29 nm of HfO_2/Al_2O_3 were deposited on HF-cleaned Si, SiO_2 and degreased SiCOH. Selectivity of the deposition increased significantly from 14 (pure HfO_2) to 41 on HF-cleaned Si with TMA co-dosing. Results indicate that TMA acts as a reactive site eliminator and a selectivity promoter. AFM was also employed to study the film surface roughness, 0.46 nm and 0.50 nm RMS roughness were measured on Si and SiO_2 in Fig. 1.3 (b) which showed a smooth film surface.

Selectivity study of TiO_2/Al_2O_3 and HfO_2/Al_2O_3 nanolaminates

Based on the two novel properties of TMA found in the preliminary study, a detailed selectivity study of both TiO_2/Al_2O_3 and HfO_2/Al_2O_3 nanolaminates on HF-cleaned Si, SiO_2 and degreased SiCOH were conducted. Considering 30 pulses of $Ti(O^iPr)_4$ per supercycle result in a nucleation delay, a larger number of $Ti(O^iPr)_4$ pulses per supercycle such as 50 and 200 were tested to provide enough reactive sites to initiate the CVD process (shown in Fig. 1.17). With 50 $Ti(O^iPr)_4$ pulses per supercycle, an Al-rich layer was formed and only around 1 nm of deposition was observed on Si after 45 supercycles (Fig. 1.17) .

The number of $Ti(O^iPr)_4$ pulses per supercycle was increased to 200 to check the upper limit of TiO_2 layer thickness before inducing nanocrystallite formation. With an addition of 15

supercycles, a 31 nm TiO_2/Al_2O_3 nanolaminate was deposited on HF-cleaned Si and only 0.95 nm was deposited on degreased SiCOH (shown in Fig. 1.17 (a)). Around 3 nm/supercycle saturated growth rate on Si can be calculated using ellipsometry thickness measurement 30 nm divided by 10 supercycles. The nanolaminate structure was estimated from the XPS 16:20 Ti:Al ratio, ~1.7 nm of AlO_2 and 1.3 nm of TiO_2 sublayer thickness per supercycle (shown in Fig. 1.17 (b)). A selectivity of 33 was achieved on Si, similar to the single precursor TiO_2 pulsed CVD, but theTiO_2/Al_2O_3 nanolaminate had a completely smooth surface with an RMS roughness of 0.52 nm (see Fig. 1.17). TEM was performed to confirm the nanolaminate structure with an initial Al-rich layer (see Fig. 1.18). From Fig. 1.18, the Al-rich layer was found to be around 0.8 nm and each superlayer (separated by black dash) is around 2-3 nm. These numbers are consistent with the estimated thickness derived from XPS data.

To validate that 200 pulses $Ti(O^iPr)_4$ followed by 1 pulse of TMA is the ideal nanolaminate CVD process, a fixed 200 pulses $Ti(O^iPr)_4$ per supercycle was carried out on HF-cleaned Si, SiO_2 and degreased SiCOH with only a 300 °C preanneal. After the initial 10 supercycles (incubation period), ~2.9 nm was deposited on HF-cleaned Si with no deposition on SiCOH. With an additional 6 supercycles, the Si signal from HF-cleaned Si was attenuated to 0% and Si from SiCOH still had 18% (Fig. 1.4 (a)). Film thickness on HF-cleaned Si was measured by ellipsometry to be 22 nm and only 0.5 nm on SiCOH was deposited. AFM was conducted to confirm a smooth film surface on both HF-cleaned Si and SiO_2 with RMS roughness of 0.38 nm and 0.4 nm, respectively (Fig. 1.4 (b)). Based on the Ti:Al ratio (16:17), the sublayer thickness of each oxide can be estimated. Nanolaminate structure was composed of 1.5 nm of TiO_2 and 1.6 nm of AlO_2 (Fig. 1.4 (c)). Although 22 nm thickness selective deposition on HF-cleaned Si was less than previous mixed

recipe experiment (Fig. 1.17), the calculated selectivity was 44 which showed a higher selectivity than single precursor TiO_2 pulsed CVD.

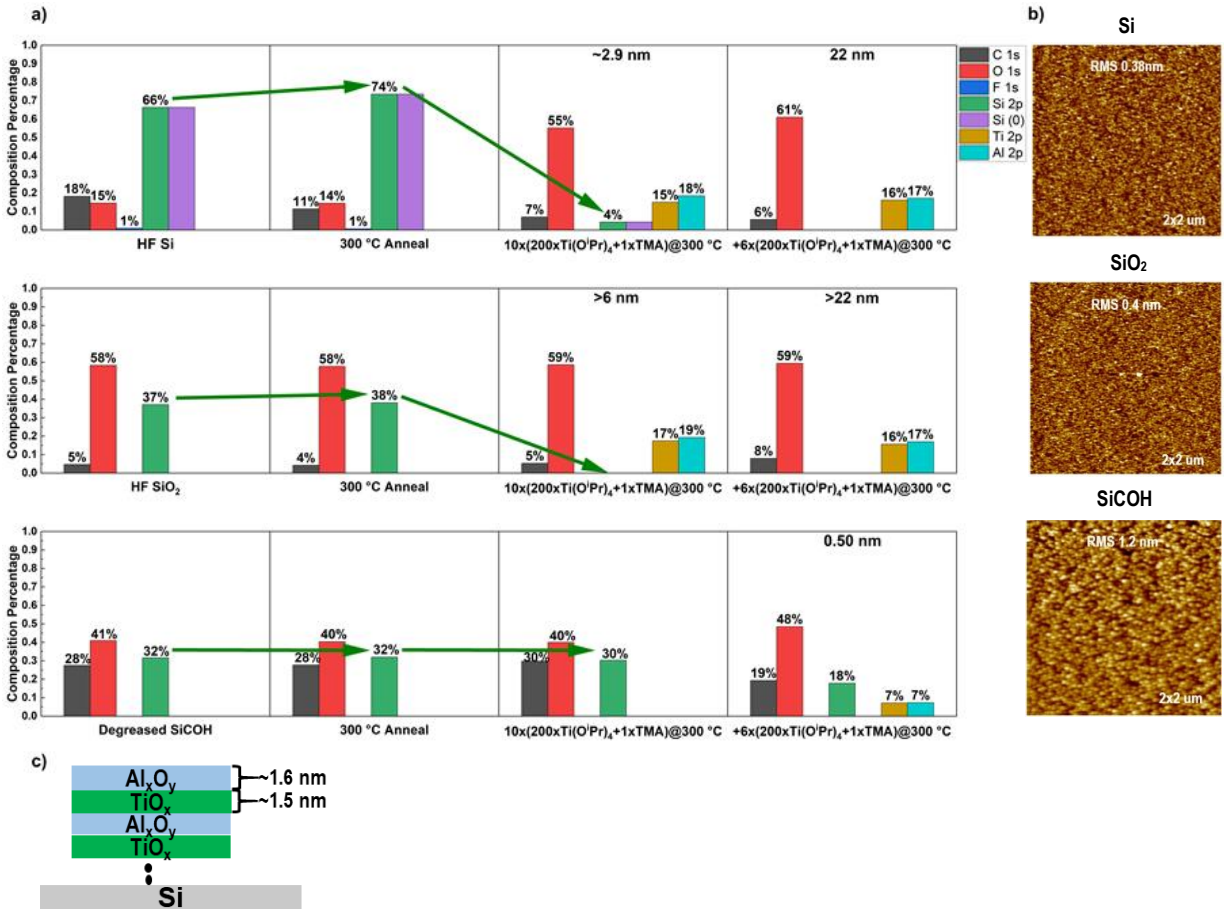

Figure 1.4. XPS Study of selectivity for Ti/AlO_x pulsed CVD. (a) $TiAlO_x$ CVD with single recipe (200 Ti pulses +1 TMA) XPS shows around 22 nm of TiO_2/Al_2O_3 nanolaminate was selectively deposited on Si in preference to SiCOH. XPS raw spectra is shown in Fig. 1.19. (b) AFM images show both TiO_2/Al_2O_3 nanolaminate films are smooth on Si and SiO_2 with 0.38 nm and 0.40 nm RMS roughness, respectively. (c) estimated nanolaminate structure composed of 1.6 nm of Al_2O_3 and 1.5 nm of TiO_2.

For HfO_2/Al_2O_3 nanolaminates, a sub-monolayer of HfO_2 is equivalent of 10 Hf(O^{t}Bu)$_4$ pulses, and HfO_2 is known to readily form nanocrystallites at 300 °C [18, 38]. The single recipe for HfO_2/Al_2O_3 nanolaminate CVD supercycle was set as 12 pulses Hf(O^{t}Bu)$_4$ followed by 1 TMA pulse. This allowed HfO_2 sublayers to be thick enough to form a proper nanolaminate structure while staying thin enough to prevent nanocrystallites formation. In Fig. 1.5 (a), after a total of 20

supercycles, 11 nm of HfO_2/Al_2O_3 was selectively deposited on Si with only 0.15 nm deposition on degreased SiCOH; this corresponds to a selectivity of 73. The selectivity was greatly improved over the single precursor HfO_2 pulsed CVD which has a selectivity of 14. AFM images of both Si and SiO_2 samples showed a smooth HfO_2/Al_2O_3 film (Fig. 1.5 (b)). Based on the Hf:Al (17:18) ratio from the XPS plot, nanolaminate structure with HfO_2 and AlO_2 alternating subnanometer layers is proposed (Fig. 1.5 (c)).

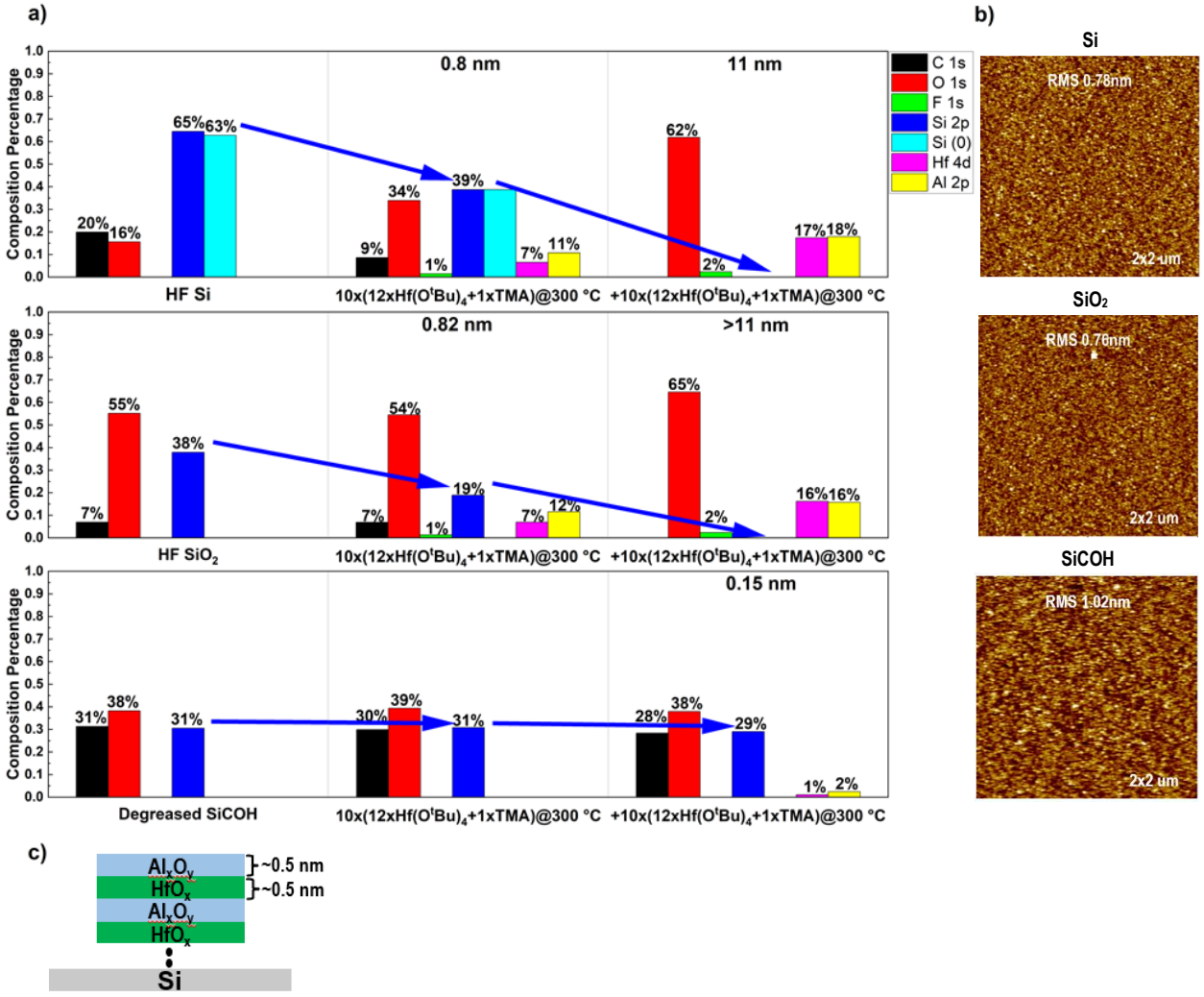

Figure 1.5. XPS Study of selectivity for Hf/AlO_x pulsed CVD. (a) after 300 °C preanneal, XPS of single recipe (12 Hf pulses +1 TMA) $HfAlO_x$ CVD shows around 11 nm of HfO_2/Al_2O_3 nanolaminate was selectively deposited on Si in preference to SiCOH. Raw data is shown in Fig. 1.20. (b) AFM shows 0.78 nm and 0.76 nm RMS roughness on Si and SiO_2 samples, respectively. (c) estimated nanolaminate structure composed of 0.5 nm of Al_2O_3 and 0.5 nm of HfO_2.

Mechanism and Nanoselectivity Tests

Based on the selectivity study, a proposed mechanism of selective water-free TiO_2/Al_2O_3 and HfO_2/Al_2O_3 nanolaminates pulsed CVD is shown in Fig. 1.6. In Fig. 1.6 (a) and (b), $Hf(O^tBu)_4$ (or $Ti(O^iPr)_4$) adsorbs on the H-terminated Si (H-Si) and OH-terminated SiO_2 (OH-SiO_2), surface and decomposes into $Hf(O^tBu)_xOH^-_{4-x}$ ($Ti(O^iPr)_xOH^-_{4-}$). [17, 18] It is hypothesized that the (OH^-) groups in the intermediate react with weaker bonding H-Si and OH-SiO_2 sites inducing chemisorption followed by a continuous growth. Even with TMA being introduced later, there are still enough H-Si or OH-SiO_2 reactive sites to nucleate and maintain the growth. Conversely, as shown in Fig. 1.6 (c), It is posed that CH_3-terminated SiCOH surface is thermodynamically less favorable for the adsorption of $Hf(O^tBu)_4$. Precursor molecules can be physiosorbed on SiCOH, but most of the precursor will thermally desorbed before dissociating. Although HfO_2 nucleation might start on (OH^-) defects sites on SiCOH, only limited growth will occur. It is proposed that HfO_2 nucleation will quickly be terminated on SiCOH by TMA since there are very few reactive sites (Si-OH), but TMA has a more modest effect on SiO_2 and Si since they have a much higher density of reactive sites (Si-OH and Si-H, the later may not be passivated by TMA).

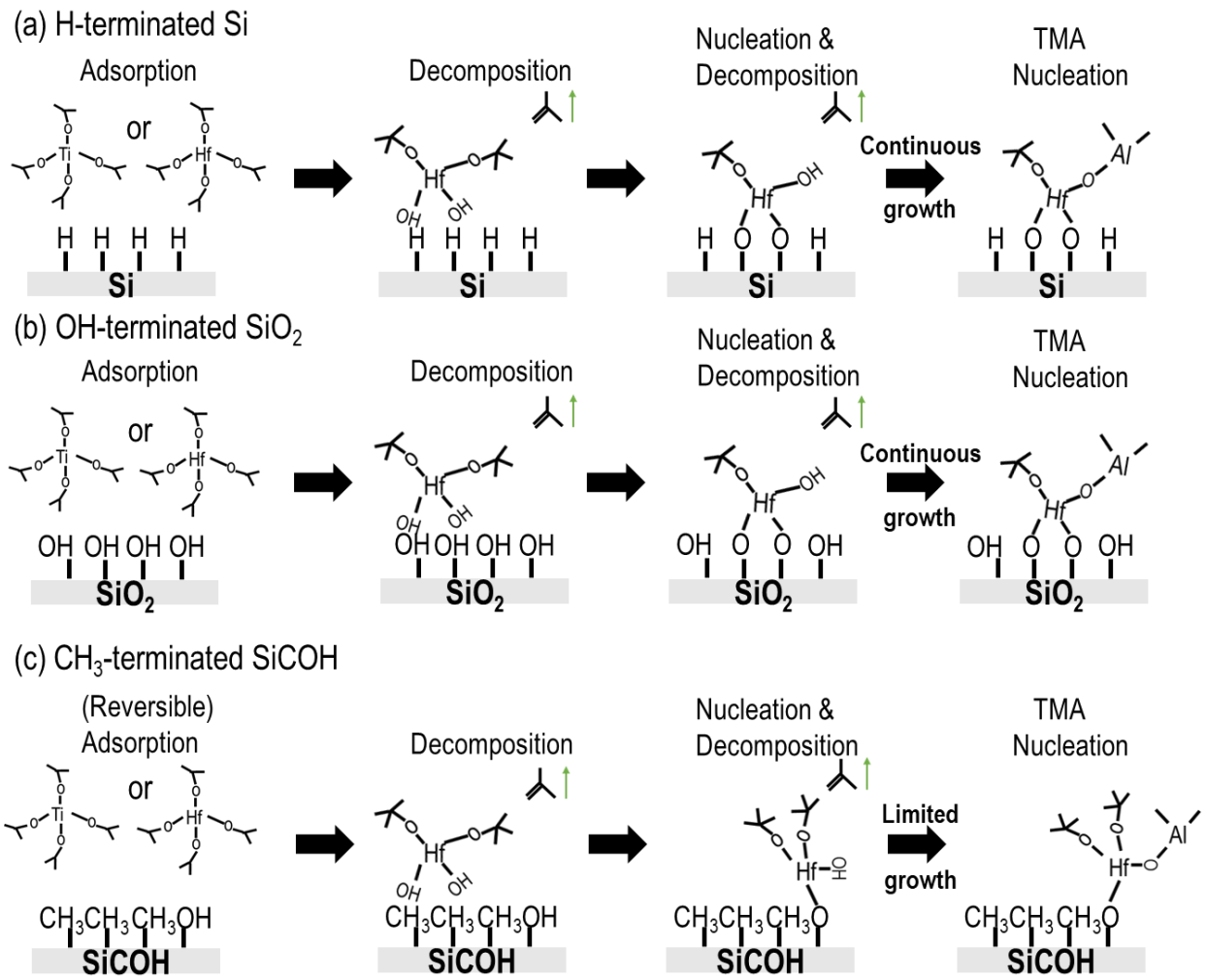

Figure 1.6. Proposed mechanism of enhancement of HfO_2 and TiO_2 on Si, SiO_2 versus SiCOH with TMA induced nanolaminate formation. (a)(b) On H-terminated Si and OH-terminated SiO_2, precursors can easily adsorb and undergo decomposition due to the high density of reactive sites. (c) CH_3-terminated SiCOH has less adsorption of $Hf(O^tBu)_4$ or $Ti(O^iPr)_4$ on the surface. Defect (OH^-)sites might start nucleation, but the nucleation can be readily suppressed on SiCOH by TMA.

Based on the proposed mechanism, this selective water-free TiO_2/Al_2O_3 and HfO_2/Al_2O_3 nanolaminate pulsed CVD can be applied to any surface with (OH^-) sites (or other reactive sites) in preference to SiCOH. Cu is known to form CuO_x on its surface. Previous result showed that blanket Cu samples have a similar or higher oxide CVD growth rate than SiO_2 (see Fig. 1.21). Selectivity between Cu and SiCOH should be greater than the selectivity study on Si vs SiCOH. Therefore, a Cu/SiCOH patterned sample was employed to test the nanoselectivity of the

nanolaminate CVD processes. Due to the damage of SiCOH by the fabrication processes and an extremely long duration (8 months) of air exposure of the patterned sample from the time of fabrication, a passivation was needed due to repair the SiCOH.

For each nanoselectivity test, passivated Cu/SiCOH sample was loaded together with a passivated SiCOH reference sample. TiO_2/Al_2O_3 nanolaminate and HfO_2/Al_2O_3 nanolaminate were independently tested for selectivity.

Cu/SiCOH was processed planarized with standard CMP processing which often involves use of organics to inhibit Cu oxidation; these organics need to be removed for CVD on the Cu surface. The sample was degreased with acetone, methanol, and water before passivation. Afterward, the patterned sample was rapidly loaded into the chamber. A 30 mins 350C UHV anneal was conducted to remove surface organic species. Possible benzotriazole (BTA) residue (a typical Cu oxidation inhibitor) should be mostly removed during the anneal according to the thermal stability studies of BTA [39, 40]. Furthermore, XPS show no CVD induction delay on the Cu surface consistent with a nearly clean Cu surface being prepared. However, as shown in the cross-sectional TEM EELS study later, there may still be a small amount of carbon on the patterned Cu surface.

HfO_2/Al_2O_3 XPS data plots are shown in Fig. 1.7 for nanoselectivity. The anneal induced the oxygen peak to decrease from 33% to 31% and carbon peak to decrease from 48% to 23% on the patterned sample. With a total of 15 supercycles (12 $Hf(O^tBu)_4$ pulses and 1 TMA pulse) , the Cu signal on the patterned sample was decreased to zero which means at least 3-5 nm of HfO_2/Al_2O_3 was deposited on Cu region. Hf and Al percentage on the pattern sample were 8% and 11%, respectively. The Si signal on the patterned sample also decreased; this is probably due to the X-ray beam interference by nanolaminate deposition. As deposition on Cu region increased,

less glancing angle X-ray intensity reached the SiCOH region. The SiCOH reference sample showed no trace of Al XPS signal which is consistent with little or no deposition on the patterned sample SiCOH region.

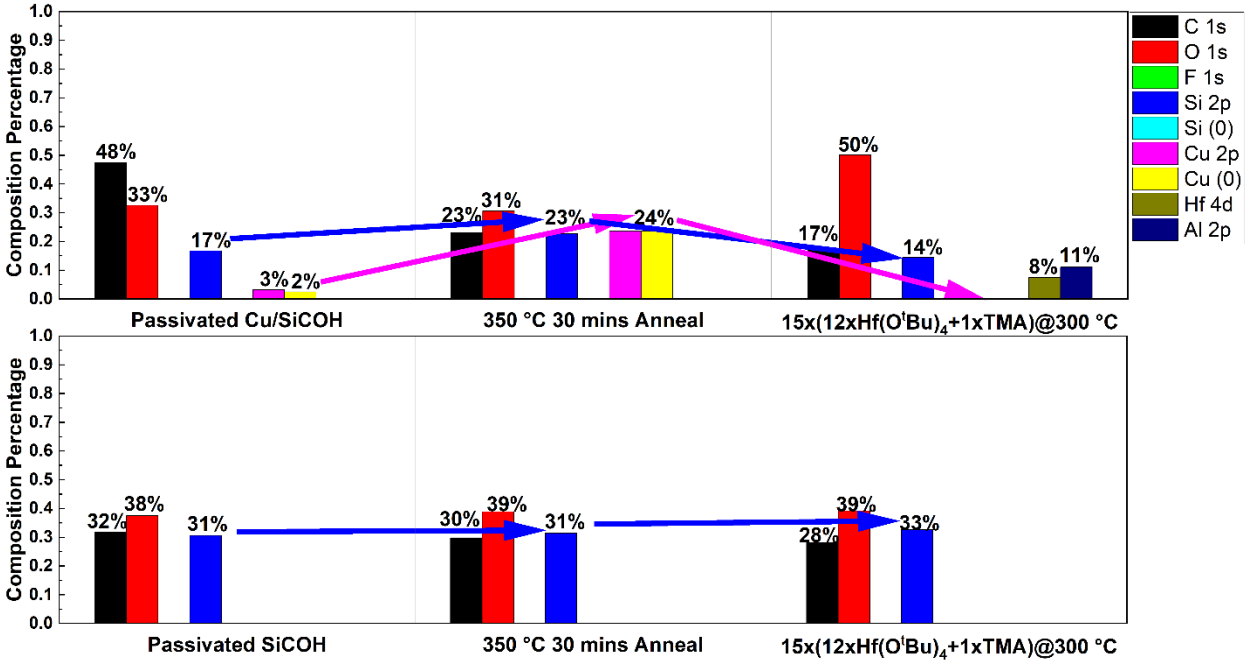

Figure 1.7. XPS study of nanoselectivity for HfO_2/Al_2O_3 nanolaminate on a patterned sample. XPS of single recipe (12 Hf pulses +1 TMA) $HfAlO_x$ CVD shows at least 5 nm of HfO_2/Al_2O_3 nanolaminate was selectively deposited on Cu region of the pattern sample while blank SiCOH sample shows no sign of deposition. Raw data is shown in Fig. 1.22.

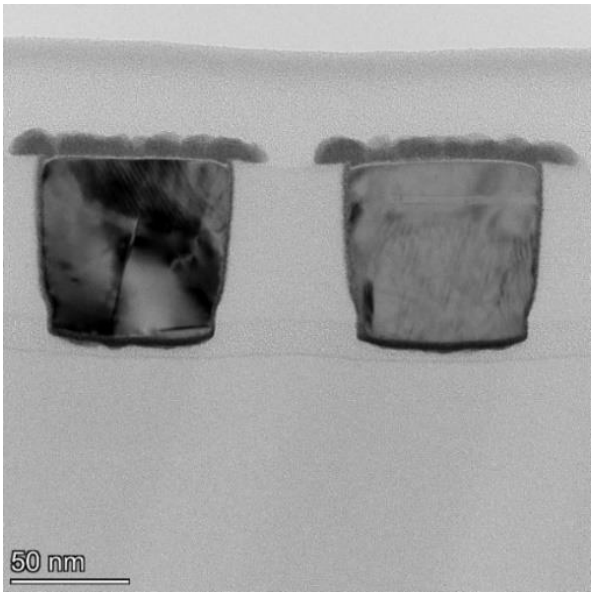

Figure 1.8. TEM of HfO_2/Al_2O_3 nanolaminate on a patterned sample. TEM image shows that HfO_2/Al_2O_3 nanolaminate selectively deposited on Cu region in preference to SiCOH.

After the HfO_2/Al_2O_3 pulsed CVD deposition, TEM was performed on the patterned sample. As shown in Fig. 1.8, around 8 nm of HfO_2/Al_2O_3 was selectively deposited on Cu region and no deposition was observed on SiCOH region. The growth of HfO_2/Al_2O_3 might be following the Volmer-Weber nucleation mode since island structures were observed. The higher reactivity and lower dissociation temperature (compared to $Ti(O^iPr)_4$) of the $Hf(O^tBu)_4$ precursor allows faster nucleation and dissociation. During continuous growth, one $Hf(O^tBu)_4$ can dissociate and provide three additional OH^- reactive sites for sequential dosing which leads to a mushroom-shape isotropic growth and induces formation of the overhang (a schematic diagram please see Fig. 1.23). The observed growth pattern is consistent with Volmer-Weber nucleation, higher dissociation rate and isotropic growth as well as growth overhang for $Hf(O^tBu)_4$.

Similar XPS results were observed for the TiO_2/Al_2O_3 pulsed CVD deposition on patterned samples as shown in Fig. 1.9. After 30 minutes of 350 ℃ anneal, the carbon percentage on the Cu/SiCOH patterned sample dropped from 38% to 24%. The oxygen percent which might come from surface hydrocarbon contamination decreased from 51% to the usual normal 29%. After a

total number of 8 supercycles (200 $Ti(O^iPr)_4$ pulses with 1 TMA pulse), the Cu signal on the patterned sample disappeared and 8% of Ti and 9% of Al were observed.

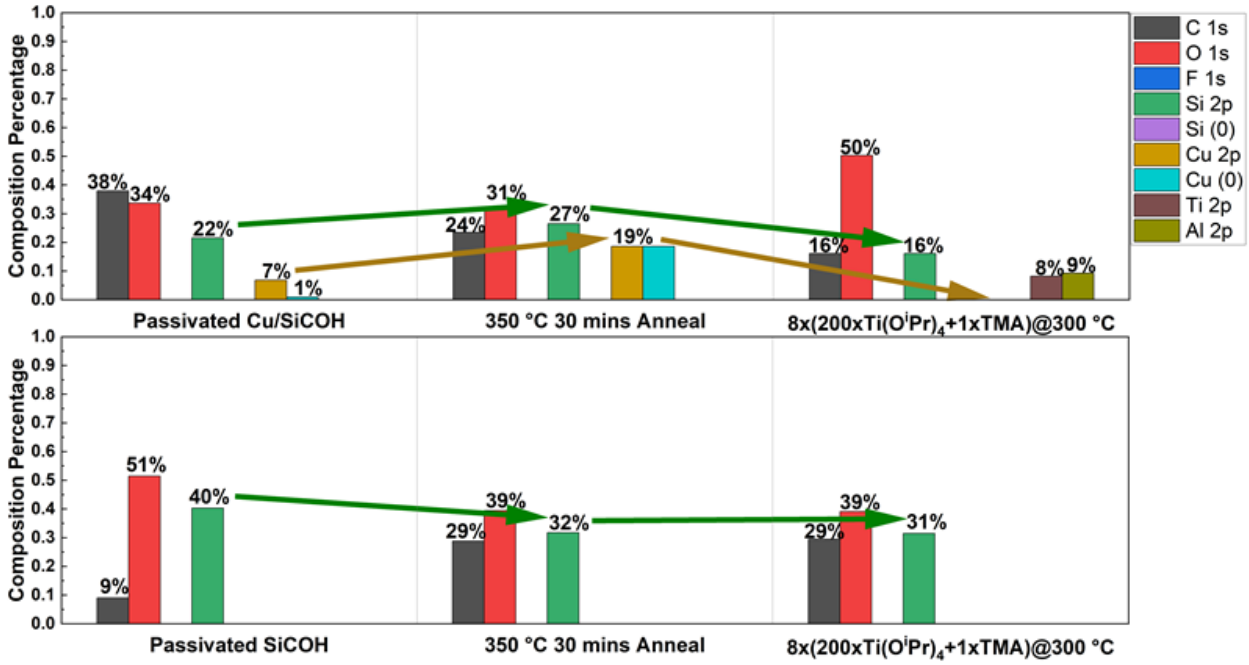

Figure 1.9. XPS study of nanoselectivity for TiO_2/Al_2O_3 nanolaminate on a patterned sample. XPS of single recipe (200 Ti pulses +1 TMA) $TiAlO_x$ CVD shows at least 5 nm of TiO_2/Al_2O_3 nanolaminate was selectively deposited on Cu region of the pattern. Raw data is shown in Fig. 1.24.

As shown in the TEM image in Fig. 1.10, ~10 nm of TiO_2/Al_2O_3 nanolaminate was successfully deposited only onto the Cu substrate while the SiCOH region remained clean and pristine. The white interfacial layer between Cu and deposition was studied by dark-field TEM and EELS (shown in Fig. 1.10). Dark-field TEM did not show any interfacial layer, but EELS elements mapping clearly identified a layer of carbon-rich content on the interface between Cu and the CVD oxide. By overlapping Cu with C and Cu with O, a layer of carbon-rich content was identified on the Cu interface before O signal increase and O mapping shows no signs of CuO_x at the interface. This carbon-rich layer might come from the BTA used in the CMP process or from

the oxide CVD process. Selectivity probably could be increased without this carbon-rich layer using a proper pre-clean method such as H_2 plasma.

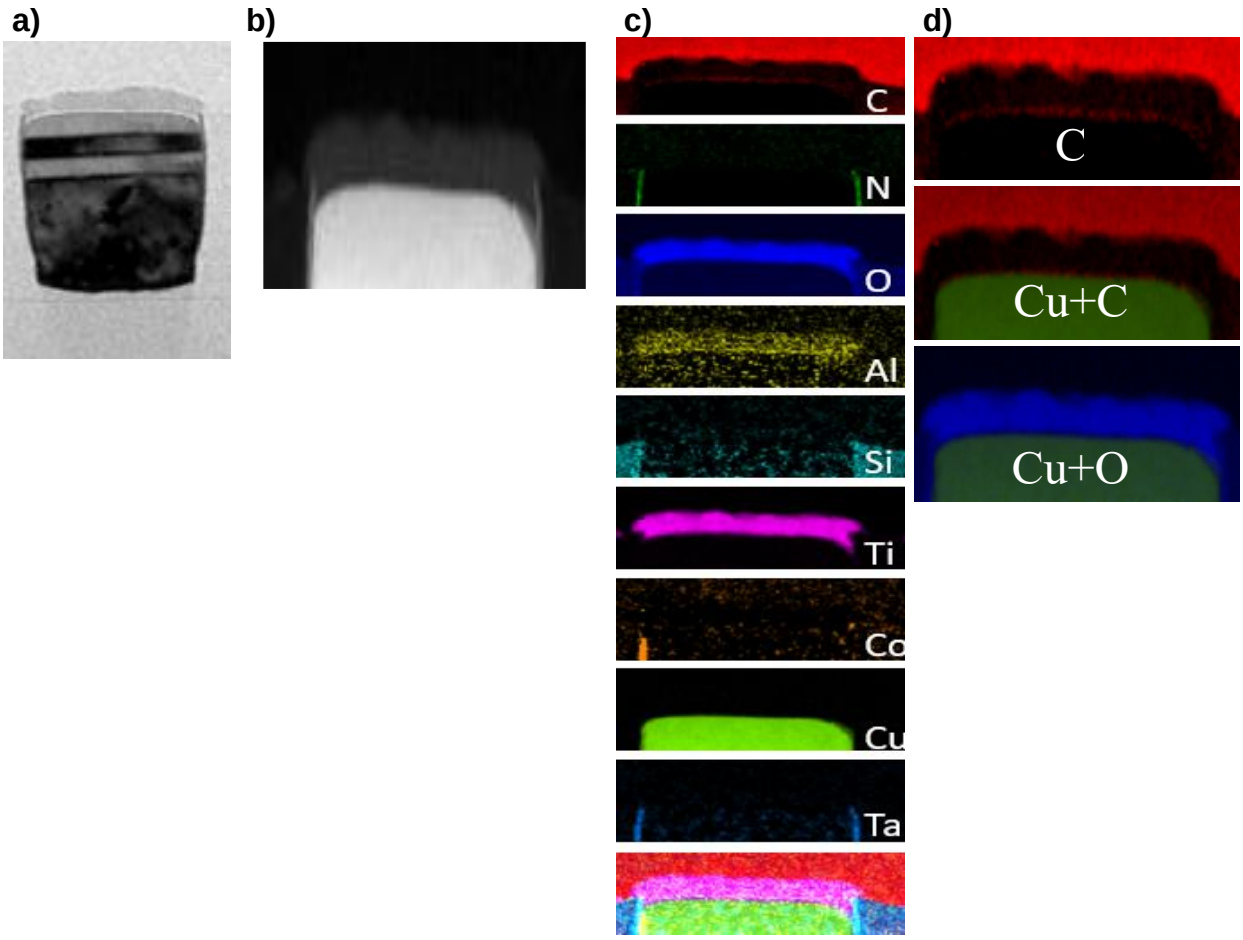

Figure 1.10. TEM and EELS study of TiO_2/Al_2O_3 on the patterned sample. From left to right: a) bright field TEM, b) dark field TEM, c) mapping of all elements, d) carbon element mapping showed a high intensity layer at the white interface area, copper with carbon overlap mapping proved a thin carbon-rich layer right on top of the copper interface, and a small gap was found between copper and oxygen consistent with the absence of CuO_x formation.

The TiO_2/Al_2O_3 nanolaminate appeared to grow only vertically without lateral growth. This may be caused by its lower dissociation rate, higher selectivity, and Cu recess structure resulting from the chemical mechanical polish (CMP). From the close-up TEM in Fig. 1.11, a recess structure was observed on both the top edges of Cu. This recess structure allowed the ALD

TaN/Co diffusion barrier to act as a physical vertical wall. Since $Ti(O^iPr)_4$ is less reactive and more selective than $Hf(O^tBu)_4$, it is harder for $Ti(O^iPr)_4$ to nucleate on TaN. With the help of the TaN wall, lower dissociation rate, and anisotropic film growth, no lateral overhang was observed for this thickness of TiO_2/Al_2O_3. This makes the TiO_2/Al_2O_3 nanolaminate a strong candidate for Cu diffusion barrier and etch stop layer [14-16]. Integrated with SAMs that selectively passivated Cu, this nanolaminate can be used as dielectric on dielectric to increase via to line critical dimension and improve time dependent dielectric breakdown [16]. TiO_2/Al_2O_3 nanolaminate may also be a unique spacer material in self-aligned double patterning method by maintaining the resolution of the feature while reducing the pitch size.

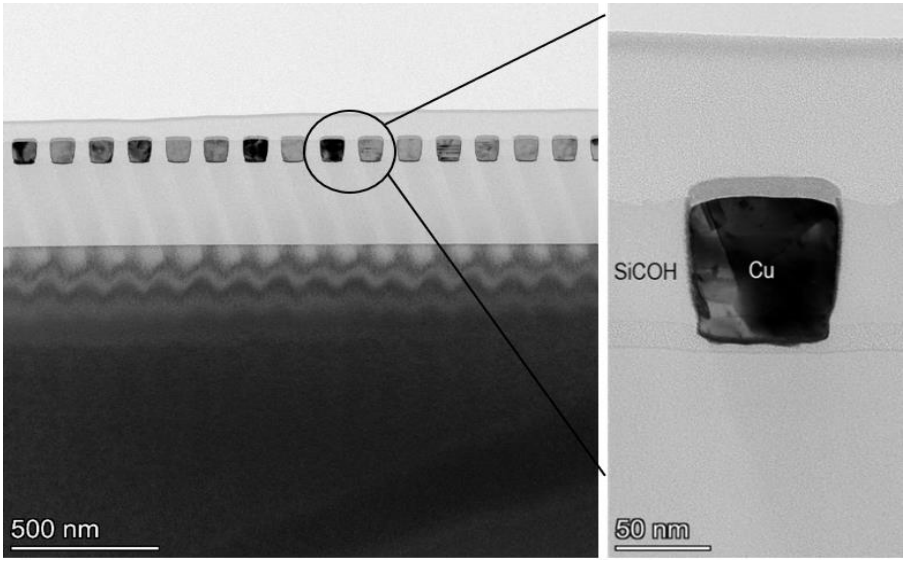

Figure 1.11. TEM of TiO_2/Al_2O_3 nanolaminate on a patterned sample. TEM image shows that TiO_2/Al_2O_3 nanolaminate selectively deposited on Cu region only with no lateral growth.

1.4 Conclusion

Inherently selective TiO_2/Al_2O_3 nanolaminates were grown on HF-cleaned Si, SiO_2 in preference to degreased SiCOH by water-free pulsed CVD using $Ti(O^iPr)_4$ and TMA as reactants. The same method was applied to achieve selective HfO_2/Al_2O_3 nanolaminate growth using $Hf(O^tBu)_4$ and TMA as precursors. Employing TMA as the co-reactant without water present

prolonged the nucleation period on all substrates of both TiO_2/Al_2O_3 and HfO_2/Al_2O_3 nanolaminates thereby increasing selectivity. For optimal selectivity, TMA needs to be dosed with a controlled pulse length that only increases the nucleation time slightly on HF-cleaned Si and SiO_2 surfaces but induces a long nucleation delay on SiCOH. For the growth stage of the nanolaminate, the number of pulses of the precursor must be set to allow only about 1 nm of growth in the TiO_2 and HfO_2 layer to prevent crystallization and consequently film roughening. For the optimized supercycles, 200 pulses $Ti(O^iPr)_4$ followed by 1 pulse of TMA and 12 pulses $Hf(O^tBu)_4$ with 1 TMA pulse were found to successfully deposit both TiO_2/Al_2O_3 and HfO_2/Al_2O_3 nanolaminates selectively on HF cleaned Si and SiO_2 in preference to SiCOH. Approximately 22 nm of TiO_2/Al_2O_3 was deposited on Si while only 0.5 nm deposition on SiCOH with a selectivity of 44. Around 11 nm of HfO_2/Al_2O_3 was deposited on Si where nucleation on SiCOH only had 0.15 nm. TEM images of Cu/SiCOH nanoselectivity samples showed both TiO_2/Al_2O_3 and HfO_2/Al_2O_3 were selectively deposited only on the Cu surface.

1.5 Supporting Information

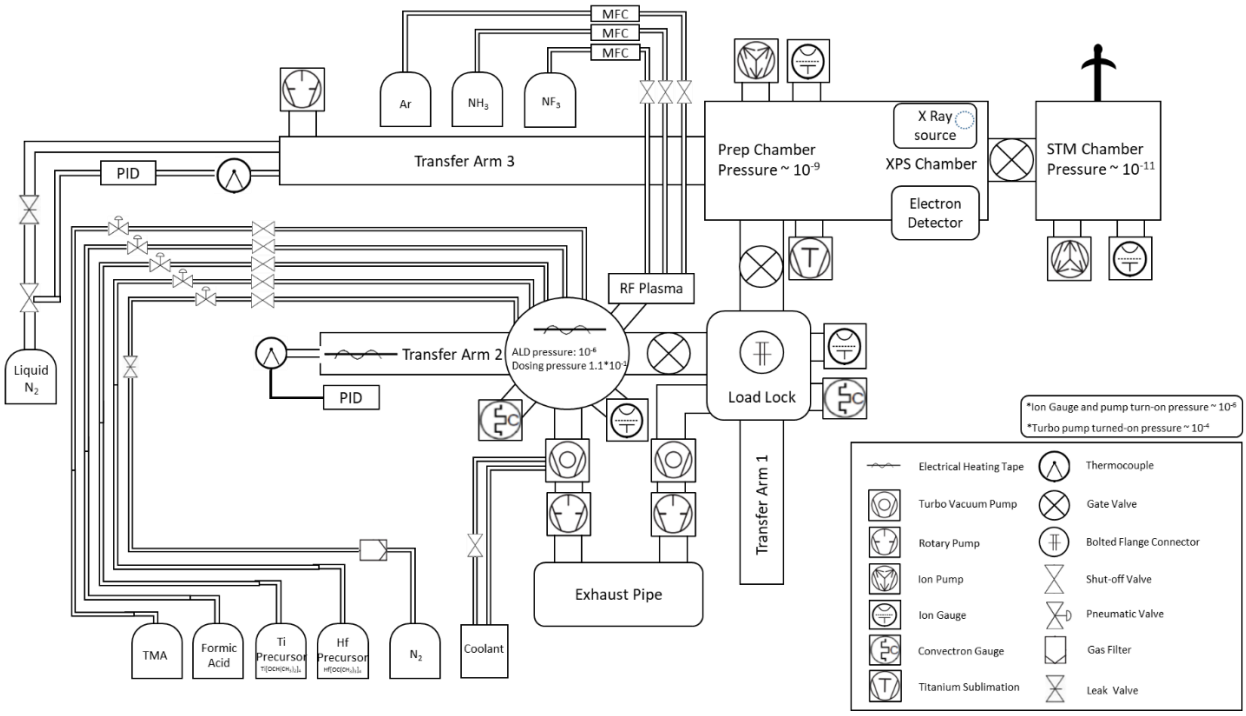

Figure 1.12. Schematic diagram illustrates the custom-built ALD/CVD with in-situ XPS system.

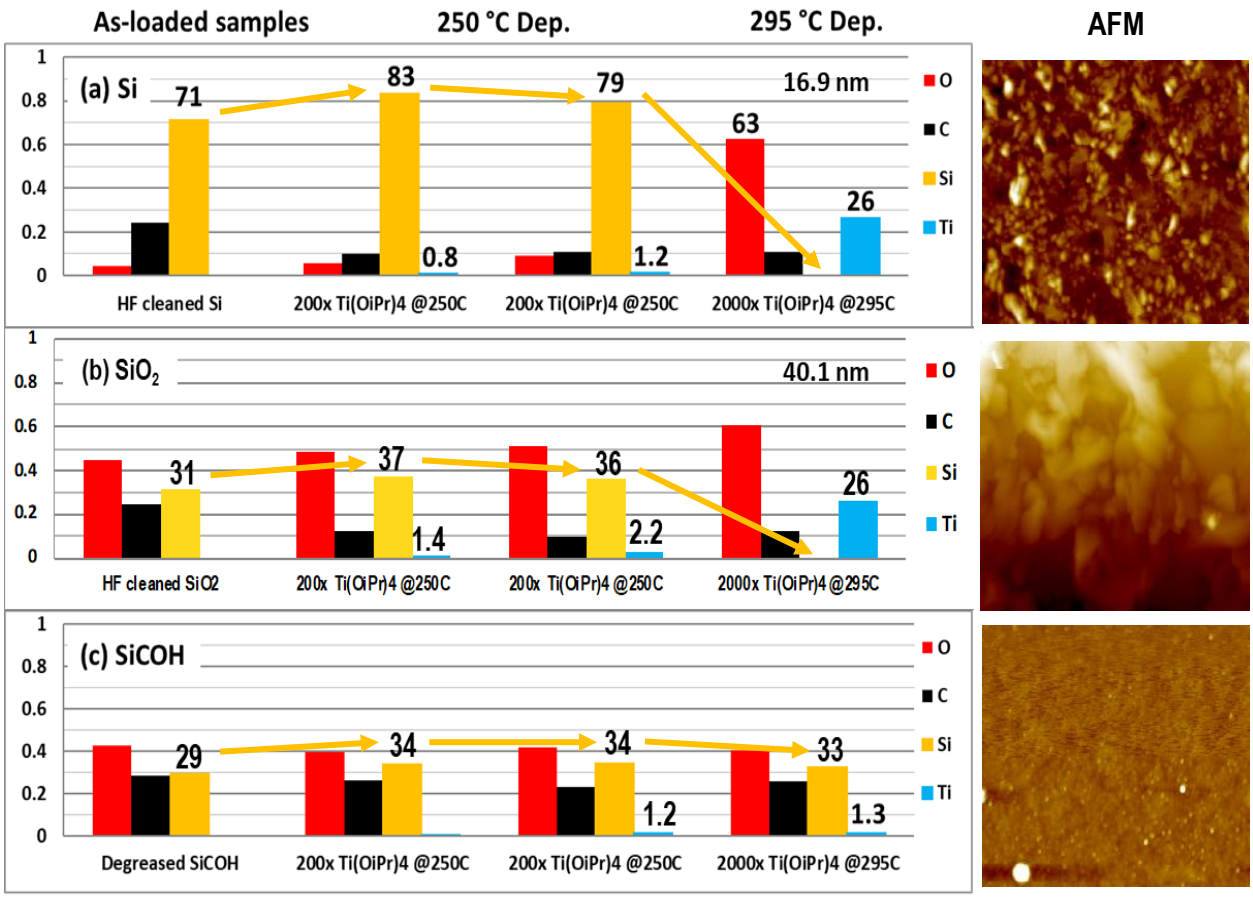

Figure 1.13. XPS study of single precursor TiO_2 pulsed CVD. [17] (a) HF cleaned Si, (b) HF cleaned SiO_2 and (c) degreased SiCOH after 2000 doses of $Ti(O^iPr)_4$ at 295 °C.

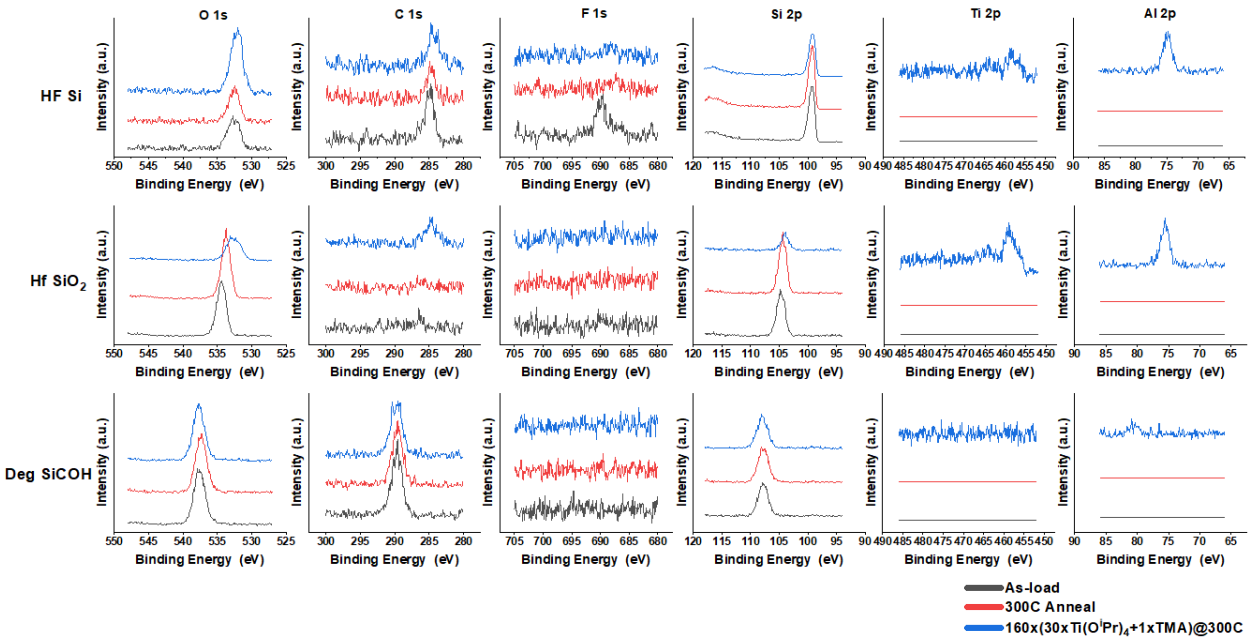

Figure 1.14. XPS raw spectra of Ti/AlOx CVD with 30 pulses of $Ti(O^iPr)_4$ followed by 1 pulse of TMA as a supercycle on HF Si, SiO_2 and degreased SiCOH simples.

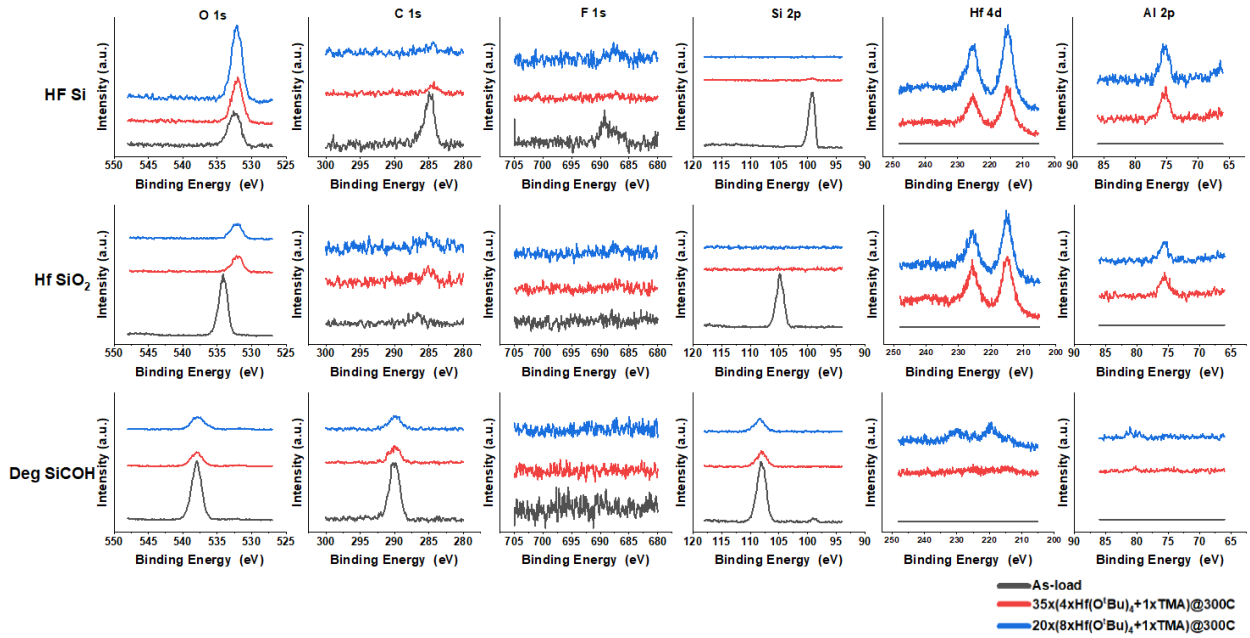

Figure 1.15. Raw spectra of XPS shows the growth suppression by TMA with 4 pulses of $Hf(O^tBu)_4$ in each supercycle while 8 pulses of $Hf(O^tBu)_4$ per supercycle.

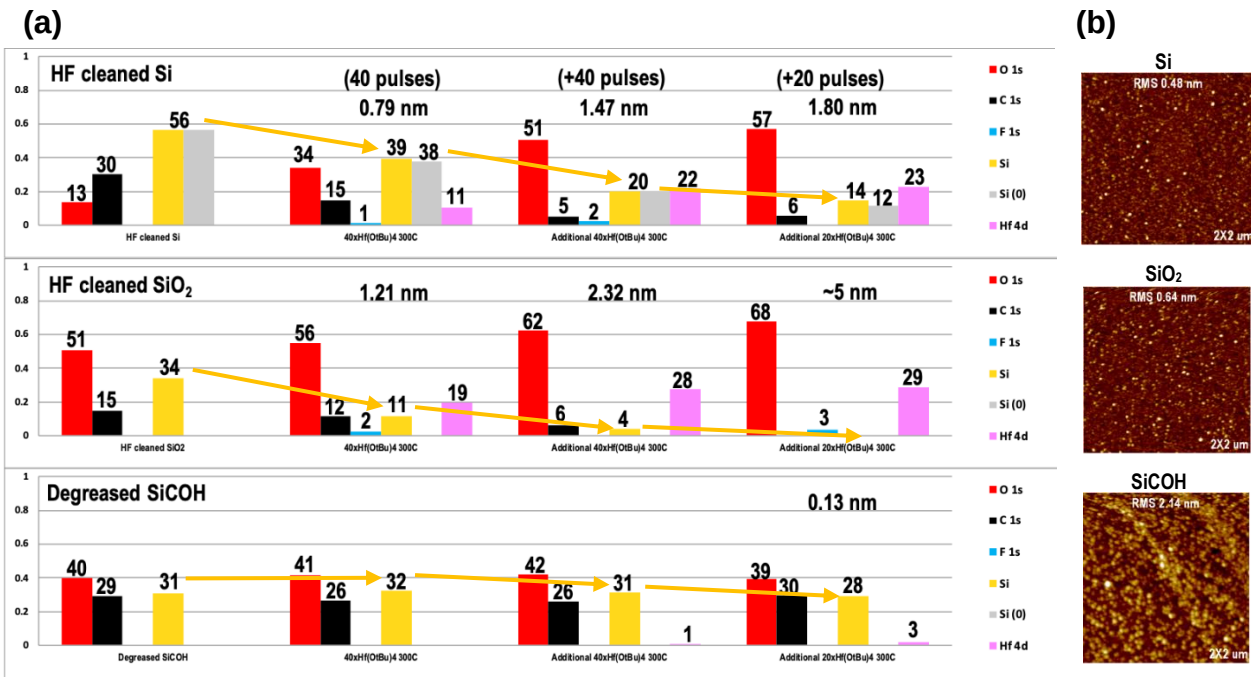

Figure 1.16. XPS chemical composition study of water-free single precursor pulsed HfO_2 CVD at 300 °C using $Hf(O^tBu)_4$. (a) XPS study on Si, SiO_2 and SiCOH after each round of deposition. (b) AFM images taken after deposition.

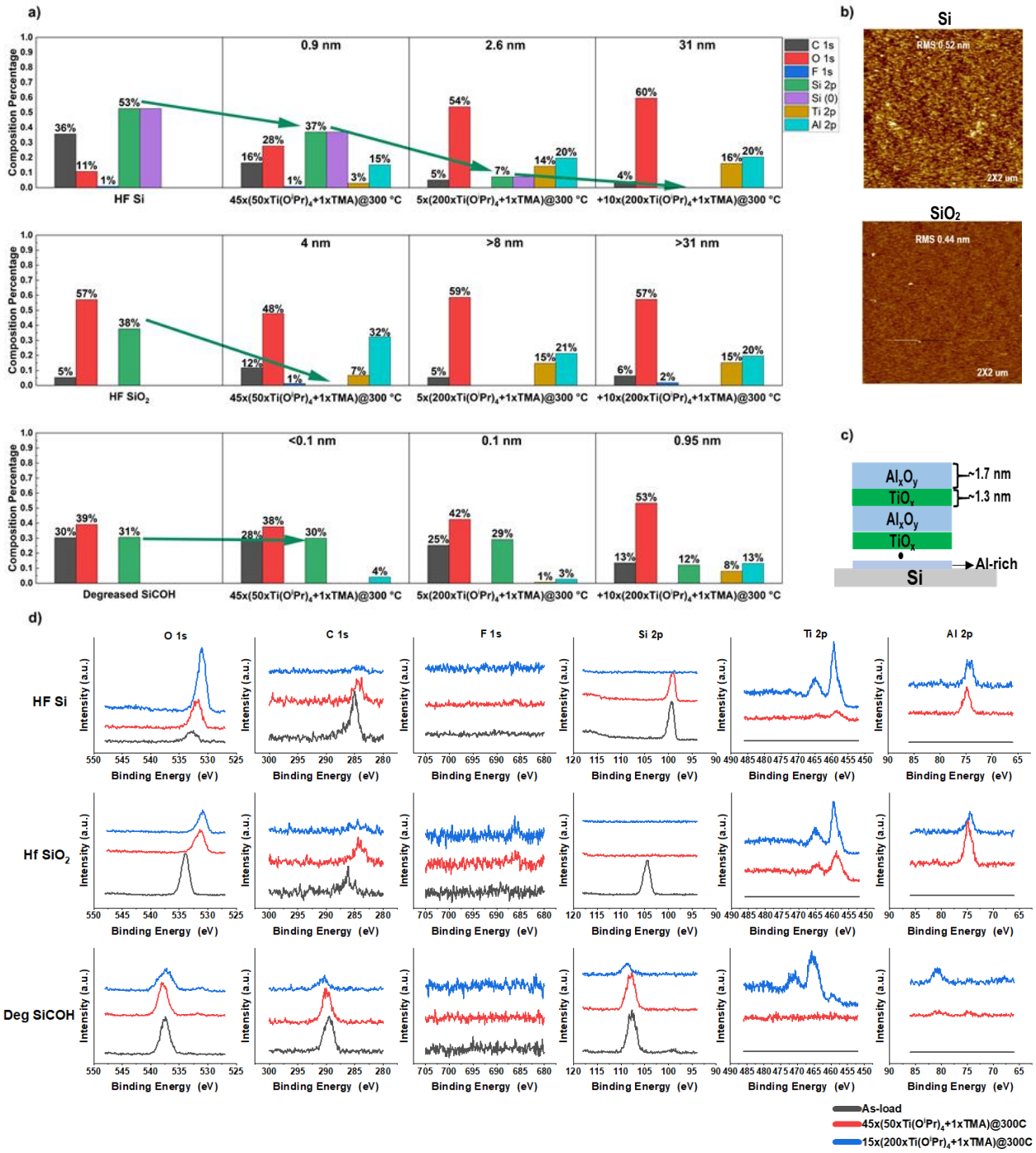

Figure 1.17. XPS and AFM studies of nucleation for Ti/AlOx pulsed CVD with different number of Ti pulses per supercycle. (a) XPS compositional study of Si, SiO2 and SiCOH after each round of deposition. (b) AFM images of Si and SiO_2 after deposition completed. (c) Schematic diagram depicts an estimated nanolaminate structure. d) raw spectra of above XPS histograms.

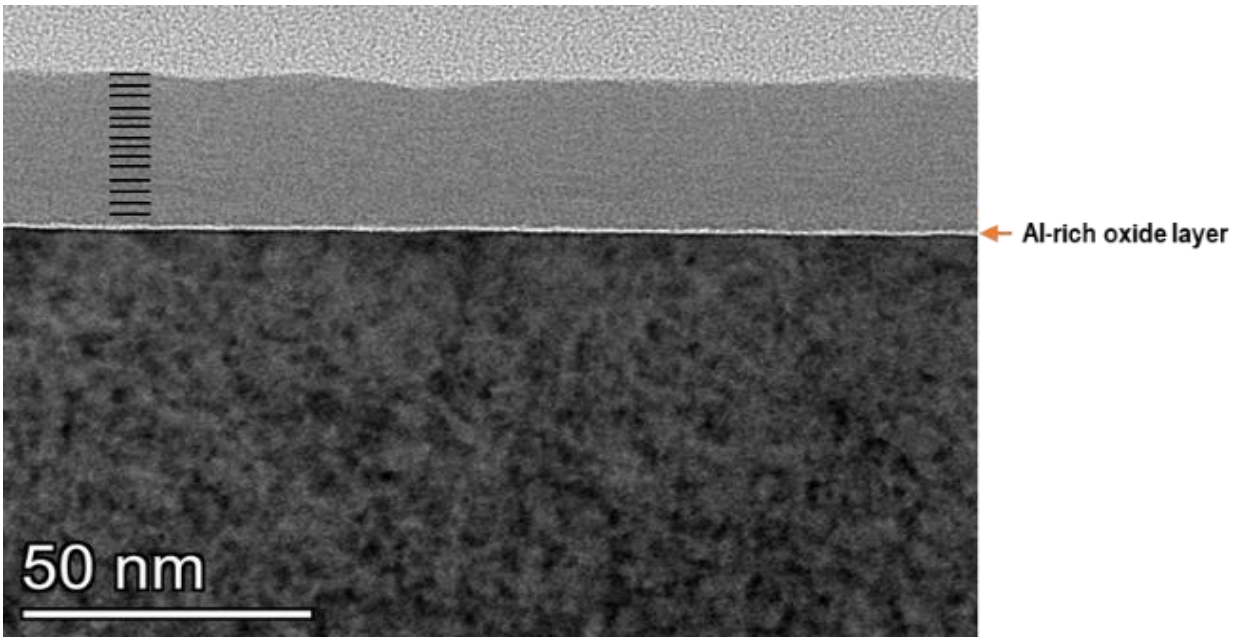

Figure 1.18. TEM of mixed recipe TiO_2/Al_2O_3 nanolaminate on a patterned sample.

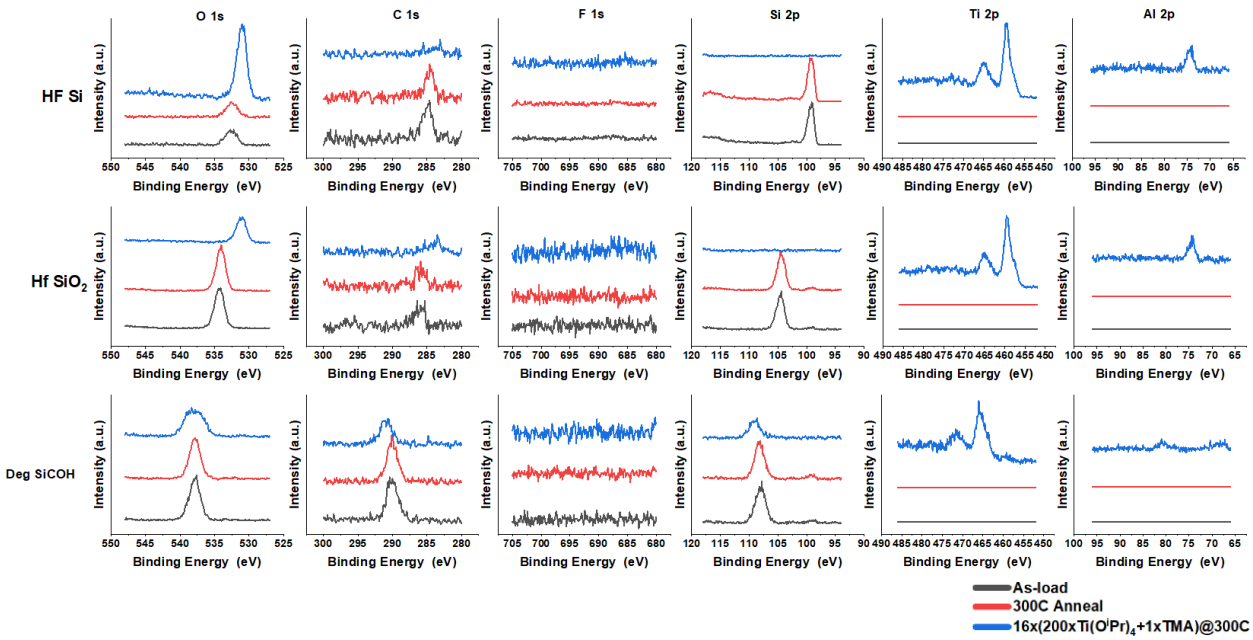

Figure 1.19. Raw spectra of TiAlOx CVD with single recipe (200 Ti pulses +1 TMA) XPS.

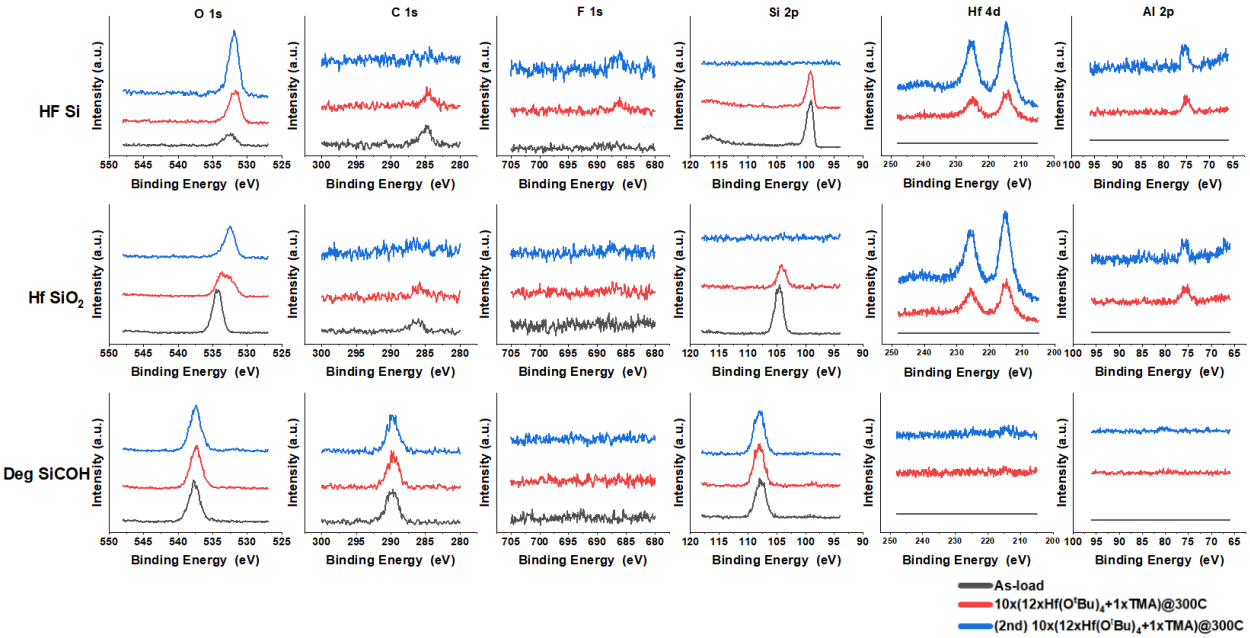

Figure 1.20. Raw XPS spectra of single recipe (12 Hf pulses +1 TMA) HfAlOx CVD.

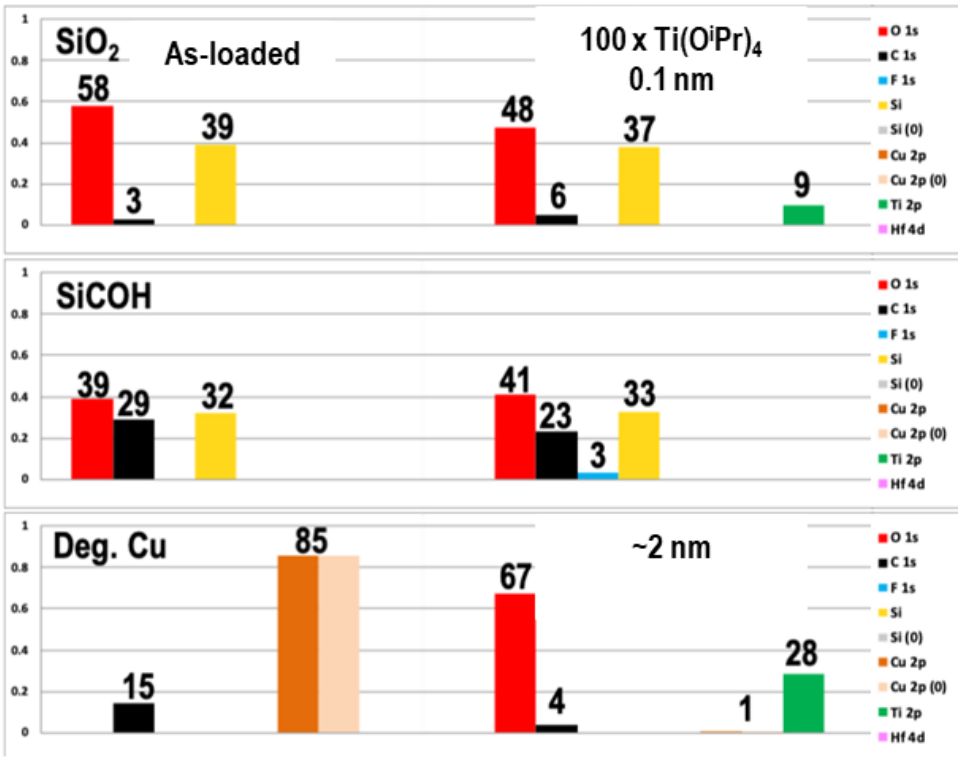

Figure 1.21. XPS study of pure TiO_2 300 °C CVD deposition on SiO_2, SiCOH and Cu.

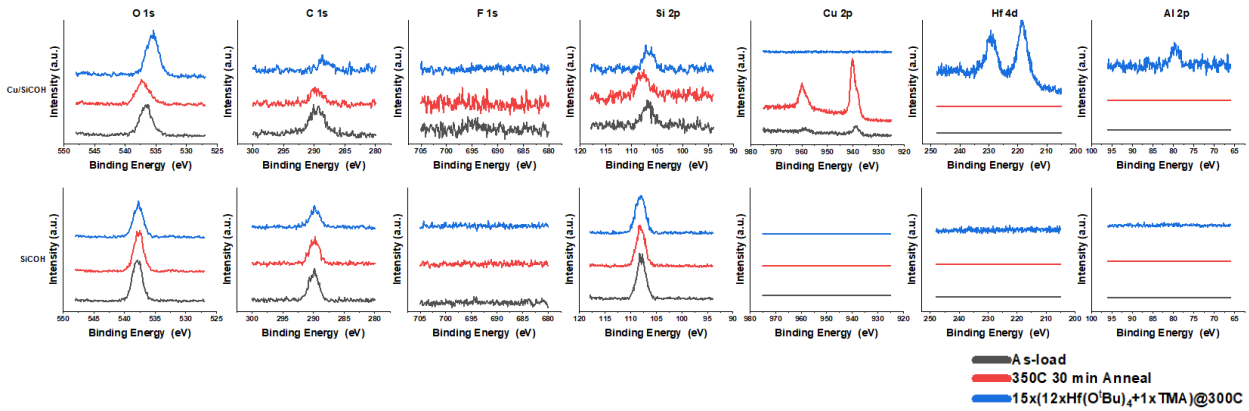

Figure 1.22. Raw XPS spectra of single recipe (12 Hf pulses +1 TMA) HfAlOx CVD on Cu/SiCOH patterned sample.

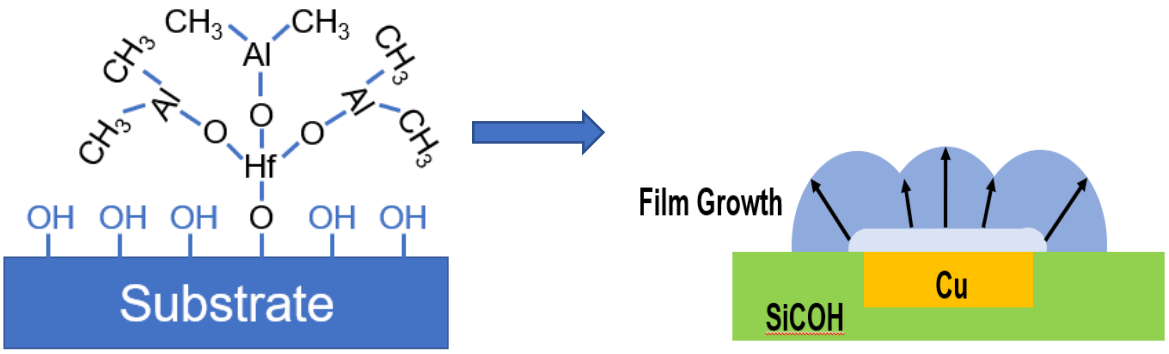

Figure 1.23. A schematic diagram shows how reactive $Hf(O^tBu)_4$ leads to a mushroom-shape isotropic growth and cause the overhang.

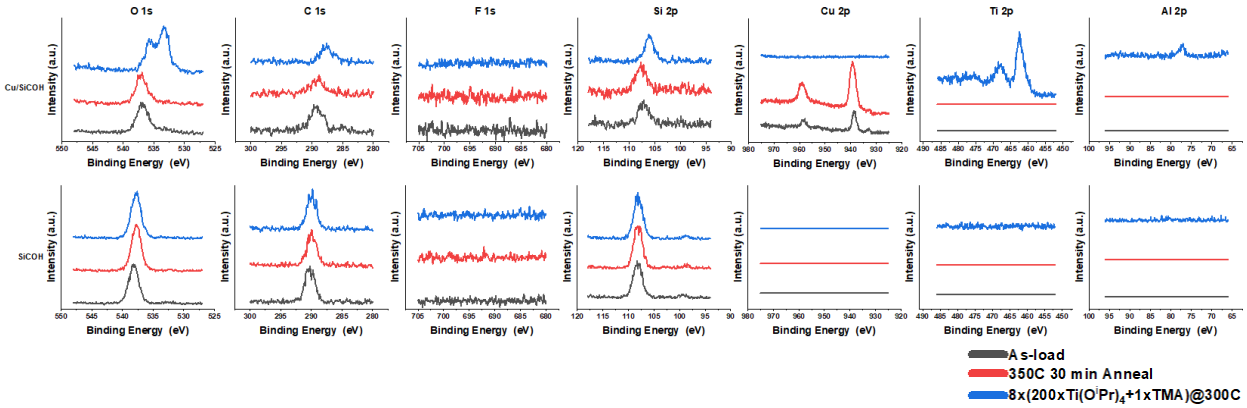

Figure 1.24. Raw XPS spectra of single recipe (200 Ti pulses +1 TMA) TiAlOx CVD on Cu/SiCOH patterned sample.

1.6 References

1. Ito, T.; Okazaki, S. Pushing the Limits of Lithography. *Nature* **2000**, *406* (August), 1027–1031.L. R. Harriott, "Extended Defects in Germanium," *Ext. Defects Ger.*, vol. 89, no. 3, 2009, https://doi.org/10.1007/978-3-540-85614-6.

2. Harriott, L. R. Next Generation Lithography. *Mater. Sci. Semicond. Process.* **1998**, *1* (2), 93–97. https://doi.org/10.1016/S1369-8001(98)00019-5.

3. Mulkens, J.; Hanna, M.; Slachter, B.; Tel, W.; Kubis, M.; Maslow, M.; Spence, C.; Timoshkov, V. Patterning Control Strategies for Minimum Edge Placement Error in Logic Devices. *Metrol. Insp. Process Control Microlithogr. XXXI* **2017**, *10145* (March 2017), 1014505. https://doi.org/10.1117/12.2260155.

4. Wu, B.; Kumar, A. Extreme Ultraviolet Lithography and Three Dimensional Integrated Circuit - A Review. *Appl. Phys. Rev.* **2014**, *1* (1), 1–15. https://doi.org/10.1063/1.4863412.

5. Li, L.; Liu, X.; Pal, S.; Wang, S.; Ober, C. K.; Giannelis, E. P. Extreme Ultraviolet Resist Materials for Sub-7 Nm Patterning. *Chem. Soc. Rev.* **2017**, *46* (16), 4855–4866. https://doi.org/10.1039/c7cs00080d.

6. Buitrago, E.; Meeuwissen, M.; Yildirim, O.; Custers, R.; Hoefnagels, R.; Rispens, G.; Vockenhuber, M.; Mochi, I.; Fallica, R.; Tasdemir, Z.; Ekinci, Y. State-of-the-Art EUV Materials and Processes for the 7nm Node and Beyond. *Extrem. Ultrav. Lithogr. VIII* **2017**, *10143* (March 2017), 101430T. https://doi.org/10.1117/12.2260153.

7. Juncker, A.; Clark, W.; Vincent, B.; Franke, J.-H.; Halder, S.; Lazzarino, F.; Murdoch, G. Self-Aligned Block and Fully Self-Aligned via for IN5 Metal 2 Self-Aligned Quadruple

Patterning. *SPIE Adv. Lithogr.* **2018**, No. March 2018, 29. https://doi.org/10.1117/12.2298761.

8. Bencher, C.; Chen, Y.; Dai, H.; Montgomery, W.; Huli, L. 22nm Half-Pitch Patterning by CVD Spacer Self Alignment Double Patterning (SADP). *Opt. Microlithogr. XXI* **2008**, *6924* (March 2008), 69244E. https://doi.org/10.1117/12.772953.

9. Dhungana, S.; Nguyen, T. D.; Nordell, B. J.; Caruso, A. N.; Paquette, M. M.; Chollon, G.; Lanford, W. A.; Scharfenberger, K.; Jacob, D.; King, S. W. Boron and High- k Dielectrics: Possible Fourth Etch Stop Colors for Multipattern Optical Lithography Processing . *J. Vac. Sci. Technol. A Vacuum, Surfaces, Film.* **2017**, *35* (2), 021510. https://doi.org/10.1116/1.4974920.

10. Majumder, P.; Katamreddy, R.; Takoudis, C. Atomic Layer Deposited Ultrathin HfO2 and Al2O 3 Films as Diffusion Barriers in Copper Interconnects. *Electrochem. Solid-State Lett.* **2007**, *10* (10), 3–8. https://doi.org/10.1149/1.2756633.

11. Shue, W. S.; Cao, M. Fully Self-Aligned Via Integration for Interconnect Scaling Beyond 3nm Node. **2021**, 486–489.

12. Doll, G. L.; Mensah, B. A.; Mohseni, H.; Scharf, T. W. Chemical Vapor Deposition and Atomic Layer Deposition of Coatings for Mechanical Applications. *J. Therm. Spray Technol.* **2010**, *19* (1–2), 510–516. https://doi.org/10.1007/s11666-009-9364-8.

13. Yang, M.; Aarnink, A. A. I.; Schmitz, J.; Kovalgin, A. Y. Inherently Area-Selective Hot-Wire Assisted Atomic Layer Deposition of Tungsten Films. *Thin Solid Films* **2018**, *649* (June 2017), 17–23. https://doi.org/10.1016/j.tsf.2018.01.016.

14. Choi, J. Y.; Ahles, C. F.; Wong, K. T.; Nemani, S.; Yieh, E.; Kummel, A. C. Highly Selective Atomic Layer Deposition of MoSiOx Using Inherently Substrate-Dependent Processes. *Appl. Surf. Sci.* **2020**, *512* (May), 144307. https://doi.org/10.1016/j.apsusc.2019.144307.

15. Lemaire, P. C.; King, M.; Parsons, G. N. Understanding Inherent Substrate Selectivity during Atomic Layer Deposition: Effect of Surface Preparation, Hydroxyl Density, and Metal Oxide Composition on Nucleation Mechanisms during Tungsten ALD. *J. Chem. Phys.* **2017**, *146* (5), 1–9. https://doi.org/10.1063/1.4967811.

16. Mackus, A. J. M.; Merkx, M. J. M.; Kessels, W. M. M. From the Bottom-Up: Toward Area-Selective Atomic Layer Deposition with High Selectivity †. *Chem. Mater.* **2019**, *31* (1), 2–12. https://doi.org/10.1021/acs.chemmater.8b03454.

17. Cho, Y.; Ahles, C. F.; Choi, J. Y.; Huang, J.; Jan, A.; Wong, K.; Nemani, S.; Yieh, E.; Kummel, A. C. Inherently Selective Water-Free Deposition of Titanium Dioxide on the Nanoscale: Implications for Nanoscale Patterning. *ACS Appl. Nano Mater.* **2022**, *5* (1), 476–485. https://doi.org/10.1021/acsanm.1c03311.

18. Choi, J. Y.; Ahles, C. F.; Cho, Y.; Anurag, A.; Wong, K. T.; Nemani, S. D.; Yieh, E.; Kummel, A. C. Selective Pulsed Chemical Vapor Deposition of Water-Free HfOx on Si in Preference to SiCOH and Passivated SiO2. *Appl. Surf. Sci.* **2020**, *512* (February), 145733. https://doi.org/10.1016/j.apsusc.2020.145733.J.

19. Testoni, G. E.; Chiappim, W.; Pessoa, R. S.; Fraga, M. A.; Miyakawa, W.; Sakane, K. K.; Galvão, N. K. A. M.; Vieira, L.; Maciel, H. S. Influence of the Al2O3 Partial-Monolayer Number on the Crystallization Mechanism of TiO2 in ALD TiO2/Al2O3 Nanolaminates and Its Impact on the Material Properties. *J. Phys. D. Appl. Phys.* **2016**, *49* (37). https://doi.org/10.1088/0022-3727/49/37/375301.

20. Ylivaara, O. M. E.; Kilpi, L.; Liu, X.; Sintonen, S.; Ali, S.; Laitinen, M.; Julin, J.; Haimi, E.; Sajavaara, T.; Lipsanen, H.; Hannula, S.-P.; Ronkainen, H.; Puurunen, R. L. Aluminum Oxide/Titanium Dioxide Nanolaminates Grown by Atomic Layer Deposition: Growth and Mechanical Properties. *J. Vac. Sci. Technol. A Vacuum, Surfaces, Film.* **2017**, *35* (1), 01B105. https://doi.org/10.1116/1.4966198.

21. Yang, T.; Xuan, Y.; Zemlyanov, D.; Shen, T.; Wu, Y. Q.; Woodall, J. M.; Ye, P. D.; Aguirre-Tostado, F. S.; Milojevic, M.; Mcdonnell, S.; Wallace, R. M. Interface Studies of GaAs Metal-Oxide-Semiconductor Structures Using Atomic-Layer-Deposited Hf O2 Al2 O3 Nanolaminate Gate Dielectric. *Appl. Phys. Lett.* **2007**, *91* (14), 3–5. https://doi.org/10.1063/1.2798499.

22. Tan, Y. N.; Chim, W. K.; Choi, W. K.; Joo, M. S.; Cho, B. J. Hafnium Aluminum Oxide as Charge Storage and Blocking-Oxide Layers in SONOS-Type Nonvolatile Memory for High-Speed Operation. *IEEE Trans. Electron Devices* **2006**, *53* (4), 654–662. https://doi.org/10.1109/TED.2006.870273.

23. Joo, M. S.; Cho, B. J.; Yeo, C. C.; Chan, D. S. H.; Whoang, S. J.; Mathew, S.; Bera, L. K.; Balasubramanian, N.; Kwong, D. L. Formation of Hafnium-Aluminum-Oxide Gate Dielectric Using Single Cocktail Liquid Source in MOCVD Process. *IEEE Trans. Electron Devices* **2003**, *50* (10), 2088–2094. https://doi.org/10.1109/TED.2003.816920.

24. Gong, Y. P.; Li, A. D.; Li, X. F.; Li, H.; Zhai, H. F.; Wu, D. Impact of the Al/Hf Ratio on the Electrical Properties and Band Alignments of Atomic-Layer-Deposited HfO2/Al2O3 on S-Passivated GaAs Substrates. *Semicond. Sci. Technol.* **2010**, *25* (5), 1–6. https://doi.org/10.1088/0268-1242/25/5/055012.

25. Kim, S. K.; Lee, S. W.; Hwang, C. S.; Min, Y.-S.; Won, J. Y.; Jeong, J. Low Temperature (<100°C) Deposition of Aluminum Oxide Thin Films by ALD with O[Sub 3] as Oxidant. *J. Electrochem. Soc.* **2006**, *153* (5), F69. https://doi.org/10.1149/1.2177047.

26. Dingemans, G.; Engelhart, P.; Seguin, R.; Mandoc, M. M.; Van De Sanden, M. C. M.; Kessels, W. M. M. Comparison between Aluminum Oxide Surface Passivation Films

Deposited with Thermal ALD, Plasma ALD and PECVD. *Conf. Rec. IEEE Photovolt. Spec. Conf.* **2010**, 3118–3121. https://doi.org/10.1109/PVSC.2010.5614508.

27. Delabie, A.; Sioncke, S.; Rip, J.; Van Elshocht, S.; Pourtois, G.; Mueller, M.; Beckhoff, B.; Pierloot, K. Reaction Mechanisms for Atomic Layer Deposition of Aluminum Oxide on Semiconductor Substrates. *J. Vac. Sci. Technol. A Vacuum, Surfaces, Film.* **2012**, *30* (1), 01A127. https://doi.org/10.1116/1.3664090.

28. Cho, Y.; Huang, J.; Ahles, C. F.; Wong, K.; Nemani, S.; Yieh, E.; Kummel, A. C. Selective Pulsed CVD of HfO_2/TiO_2 Nanolaminate for Nanoscale Patterning. presented at IEEE SISC, **2020**, San Diego, CA, USA.

29. Kwak, I.; Sardashti, K.; Clemons, M. S.; Ueda, S. T.; Fruhberger, B.; Oktyabrsky, S.; Kummel, A. C. (Invited) HfO 2 /Al2O3 Nanolaminate on Si 0.7 Ge 0.3 (100) Surface by Thermal Atomic Layer Deposition. *ECS Trans.* **2018**, *86* (7), 281–289. https://doi.org/10.1149/08607.0281ecst.

30. Balasubramanian, S.; Mundy, C. J.; Klein, M. L. Trimethylaluminum: A Computer Study of the Condensed Phases and the Gas Dimer. *J. Phys. Chem. B* **1998**, *102* (50), 10136–10141. https://doi.org/10.1021/jp982291s.

31. Longo, R. C.; McDonnell, S.; Dick, D.; Wallace, R. M.; Chabal, Y. J.; Owen, J. H. G.; Ballard, J. B.; Randall, J. N.; Cho, K. Selectivity of Metal Oxide Atomic Layer Deposition on Hydrogen Terminated and Oxidized Si(001)-(2×1) Surface. *J. Vac. Sci. Technol. B, Nanotechnol. Microelectron. Mater. Process. Meas. Phenom.* **2014**, *32* (3), 03D112. https://doi.org/10.1116/1.4864619.

32. Grill, A. PECVD Low and Ultralow Dielectric Constant Materials: From Invention and Research to Products. *J. Vac. Sci. Technol. B, Nanotechnol. Microelectron. Mater. Process. Meas. Phenom.* **2016**, *34* (2), 020801. https://doi.org/10.1116/1.4943049.

33. Baklanov, M. R.; Jousseaume, V.; Rakhimova, T. V.; Lopaev, D. V.; Mankelevich, Y. A.; Afanas'Ev, V. V.; Shohet, J. L.; King, S. W.; Ryan, E. T. Impact of VUV Photons on SiO 2 and Organosilicate Low-k Dielectrics: General Behavior, Practical Applications, and Atomic Models. *Appl. Phys. Rev.* **2019**, *6* (1). https://doi.org/10.1063/1.5054304.

34. Krishtab, M.; de Marneffe, J. F.; Armini, S.; Meersschaut, J.; Bender, H.; Wilson, C.; De Gendt, S. Metal Barrier Induced Damage in Self-Assembly Based Organosilica Low-k Dielectrics and Its Reduction by Organic Template Residues. *Appl. Surf. Sci.* **2019**, *485* (April), 170–178. https://doi.org/10.1016/j.apsusc.2019.04.083.

35. Rezvanov, A. A.; Miakonkikh, A. V.; Seregin, D. S.; Vishnevskiy, A. S.; Vorotilov, K. A.; Rudenko, K. V.; Baklanov, M. R. Effect of Terminal Methyl Group Concentration on Critical Properties and Plasma Resistance of Organosilicate Low-k Dielectrics. *J. Vac. Sci. Technol. A* **2020**, *38* (3), 033005. https://doi.org/10.1116/1.5143417.

36. Oszinda, T.; Schaller, M.; Schulz, S. E. Chemical Repair of Plasma Damaged Porous Ultra Low-κ SiOCH Film Using a Vapor Phase Process. *J. Electrochem. Soc.* **2010**, *157* (12), H1140. https://doi.org/10.1149/1.3503596.

37. Burrows, V. a; Chabal, Y. J.; Higashi, G. S.; Raghavachari, K.; Christman, S. B. Infrared Spectroscopy of Si (111) Surfaces after HF Treatment : Hydrogen Termination and Surface Morphology Infrared Spectroscopy of Si (111) Surfaces after HF Treatment : Hydrogen. **2013**, *998* (111), 10–13.

38. Hausmann, D. M.; Gordon, R. G. Surface Morphology and Crystallinity Control in the Atomic Layer Deposition (ALD) of Hafnium and Zirconium Oxide Thin Films. *J. Cryst. Growth* **2003**, *249* (1–2), 251–261. https://doi.org/10.1016/S0022-0248(02)02133-4.

39. Grillo, F.; Tee, D. W.; Francis, S. M.; Früchtl, H. A.; Richardson, N. V. Passivation of Copper: Benzotriazole Films on Cu(111). *J. Phys. Chem. C* **2014**, *118* (16), 8667–8675. https://doi.org/10.1021/jp411482e.

40. Lim, D. F.; Wei, J.; Leong, K. C.; Tan, C. S. Cu Passivation for Enhanced Low Temperature (≤300 °C) Bonding in 3D Integration. *Microelectron. Eng.* **2013**, *106*, 144–148. https://doi.org/10.1016/j.mee.2013.01.032.

Chapter 1, in full, is a reprint of the material as it appears in the following publication:

Huang, J.; Cho, Y.; Zhang, Z.; Jan, A.; Wong, K. T.; Nemani, S. D.; Yieh, E.; Kummel, A. C. (2022). Selective Pulsed Chemical Vapor Deposition of Water-Free TiO2/Al2O3 and HfO2/Al2O3 Nanolaminates on Si and SiO_2 in Preference to SiCOH. ACS Applied Materials and Interfaces, 14(13), 15716–15727. https://doi.org/10.1021/acsami.1c19810.

The dissertation author was the primary investigator and author of this paper.

Chapter 2 Dielectric on Dielectric Achieved on SiO_2 in Preference to W by Water-free Chemical Vapor Depositions with Aniline Passivation

2.1 Introduction

Current 3-D Integrated circuit (IC) requires multilayer circuits bonded together by interconnects. The advantage of the 3-D integration comes from the decrease in interconnect length, which leads to higher performance and lower power consumption [1-7]. Despite the advantages of 3-D IC, 3-D IC is also facing several challenges such as heat removal, power delivery and interconnect misalignment [8,9]. This interconnect misalignment is one of the major limitations of IC performance and scaling process due to limited via to metal line distance which leads to shorting or capacitive coupling between via and metal [10].

To solve the interconnect misalignment, Brain et al. first proposed the self-aligned via process to increase the via to metal distance for a 32nm process [11]. Subsequently, Murdoch et al. and Briggs et al. both described their fully self-aligned via integration processes with metal recess for 5nm and 7nm, respectively [12,13]. Chen at al. proposed the idea of self-aligned via integration using either metal recess etch or dielectric on dielectric (DOD) selective deposition [10]. In Chen's paper, metal recess achieved by etch has poor uniformity over the wafer due to an uneven etch rate. DOD selective deposition is the preferred approach which selectively deposits a dielectric buffer layer on top of the existing dielectric to provide the required metal recess [10]. Extra via to metal line distance (x') created by the DOD buffer layer prevented unwanted shorting, capacitive coupling effect and improved the time dependent dielectric breakdown (shown in Fig. 2.1).

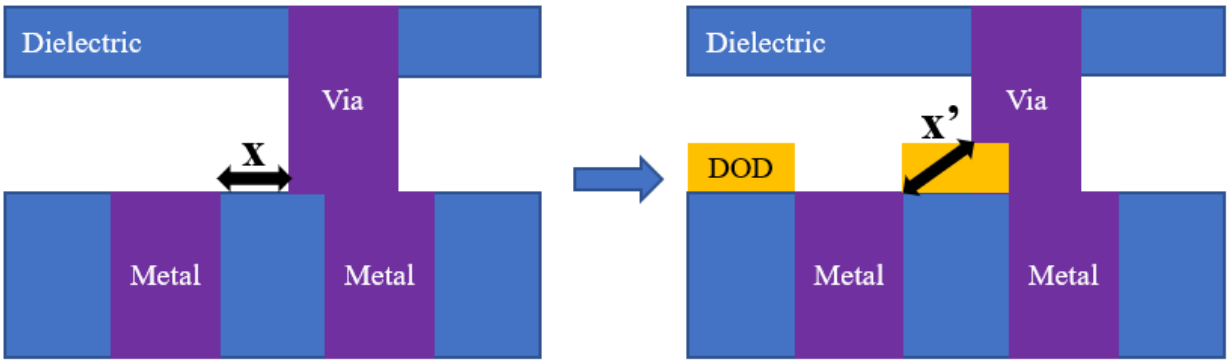

Figure 2.1. Schematic diagram of DOD increasing via to line distance by creating metal recess. Interconnect misalignment could be mitigated by employing DOD to achieve a larger via to line distance.

To achieve DOD, area selective chemical vapor deposition (AS-CVD) or atomic layer deposition (AS-ALD) is required to deposit dielectric on dielectric in preference to metal. AS-CVD can be achieved by three methods: inherent selectivity, selective passivation, and selective activation [14-16]. Inherent selectivity is achieved by the reactivity difference between two substrate surfaces. However, most CVD/ALD processes have deposition on both dielectric and metal surfaces due to their similar surface reactivity. Therefore, self-assembled monolayers (SAMs) or small organic molecule monolayers are typically employed as passivants of the metal surfaces.

Heshmi et al. and other researchers demonstrated selective passivation on metals and resultant selective DOD deposition by using octadecylphosphonic acid or thiolate as the passivant [17-19]. However, these passivant do not work well with strong oxidizers and are only compatible with low temperature (<150°C) ALD, which normally uses water as the co-reactant [20]. This low temperature water-based ALD might compromise the performance of back end of line (BEOL) circuits by inducing resistor capacitor time delay since a small amount of adsorbed water could lead to a significant increase in the k value of low k dielectric materials [21, 22].

Another promising metal passivant candidate is aniline. A. Shearer et al. showed selective Al_2O_3 deposition on SiO_2 in preference to Cu using nitrogenous aromatic small molecule inhibitors

such as pyrrole, aniline, and pyridine [23]. 3 nm selective Al_2O_3 deposition on SiO_2 was demonstrated using dimethyl aluminum isopropoxide (DMAI) and water at 150°C. M.J.M. Merkx et al. demonstrated selective TaN ALD on oxide (Al_2O_3/ SiO_2) in preference to metal (Ru/Co) with aniline passivation in each ALD cycle. With repetitive aniline passivation and a plasma ALD process, ~6 nm of selective TaN ALD was achieved on dielectric at 250°C. However, selective oxide deposition was not studied in Merkx's paper and aniline passivation was performed in every cycle of the ALD process. In addition, a plasma process will damage low k dielectrics such as SiCOH [24, 25].

Selective water-free single precursor HfO_2 pulsed CVD deposition on Si, SiO_2, and SiCOH was previously reported [26]. Selective water-free single precursor Al_2O_3 pulsed CVD has also been studied by Y. Cho et al using Aluminum-tri-*sec*-butoxide (ATSB) as the precursor [27]. At 300°C, HfO_2 deposition was achieved by pulsed dosing of hafnium tert-butoxide ($Hf(O^tBu)_4$) precursor. When pulsed gas-phase $Hf(O^tBu)_4$ molecules adsorb onto the substrate surface, it decomposes into HfO/HfOH and O^tBu/^tBu ligands. HfO/HfOH will react with the substrate hydroxyl reactive sites while remaining ligands will be removed by the nitrogen purge gas. Sequential pulses of $Hf(O^tBu)_4$ induce HfO_2 deposition. At 330°C, pulsed CVD with ATSB follows the same mechanism and deposits Al_2O_3. The use of multiple short pulses allows time for the precursors to decompose and reaction products to desorb. In the present study, DOD was achieved by the above water-free CVD processes with aniline passivation. Water-free processing is desirable when using low k dielectrics such as SiCOH to ensure they remain hydrophobic and to avoid oxidation for metal vias and interconnects. Plasma-free processing is also desirable for both conformality and to avoid damage to low-k dielectrics.

Even though aniline has been studied as a selective metal passivant in preference to dielectric in several papers, little is known about the water-free plasma-free DOD process and the aniline passivation performance above 250°C. Therefore, this work seeks to examine the thermal stability of Aniline above 250°C and establish non-destructive BEOL compatible water-free DOD processes.

2.2 Experimental Section

Reactor

All passivation and CVD processes were carried out in a custom-built vacuum chamber system (see chamber schematic diagram Fig. 2.14). It consisted of three major chambers: load-lock chamber (for sample loading and unloading), deposition chamber, and ultra-high vacuum (UHV) chamber. Two or three samples (i.e. W/SiO_2 patterned sample or W, Co, SiO_2) were simultaneously loaded into the load-lock chamber for a direct selectivity comparison. The deposition chamber has a base pressure of $2x10^{-6}$ Torr and was used for all the passivation and CVD experiments. This deposition chamber was pumped by a Pfeiffer TPH060 turbo pump with an Edwards RV3 rotary backing pump. Samples were mounted on a copper sample block with a manipulator and a cartridge heater. Samples were heated and located in the center of the deposition chamber during experiments. There was a N_2 purge line, a $Hf(O^tBu)_4$ dosing line, a $Ti(O^iPr)_4$ dosing line, an ATSB dosing line, and an aniline dosing line; all dosing lines were connected to the deposition chamber pointed directly at the sample stage at a distance of 3 inches.

Deposition Process

SiO_2, W, Co and W/SiO_2 patterned samples were used as the substrate materials. The patterned samples were obtained from Applied Materials (AMAT). For the W/SiO_2 patterned samples, the pitch size was ~55 nm and the average linewidth was ~30nm. TiN was used as a

barrier layer between W and SiO_2. All samples were degreased before loading by using acetone, methanol and HPLC water to rinse for 10 s each. A N_2 air gun was employed after each 10 s rinse to remove the residual solution on the surface. An extra 30 s 0.5% hydrofluoric acid (HF) clean followed by an HPLC water 30 s rinse was performed on SiO_2 only.

Hafnium *tert*-butoxide ($Hf(O^tBu)_4$, 99.99%), aluminum-tri-*sec*-butoxide (ATSB, 97%), titanium isopropoxide ($Ti(O^iPr)_4$, 99.99%), and aniline (ACS reagent 99.5%) were purchased from Sigma Aldrich. For each precursor dosing line, there were at least one pneumatic ALD valve and a shut off valve except for the $Hf(O^tBu)_4$ dosing line. The $Hf(O^tBu)_4$ dosing line had two pneumatic valves creating a fixed volume in between to achieve a consistent smaller pressure. The N_2 purge line had a leak valve to control the purging pressure. The deposition chamber wall and the dosing lines were heated by heating tapes and kept at 150°C. No carrier gas was used for any of the precursors.

For HfO_2 and TiO_2 single precursor CVD processes, experiments were carried out at 300°C which is the optimized dosing temperature according to previous research [26, 28]. For ATSB single precursor CVD, experiments were conducted at 330°C for better nucleation and faster growth [27]. Aniline passivation was performed before any CVD processes by trapping the samples inside the deposition chamber (without pumping) for 40 minutes at 250~350°C with a constant pressure of 780 mTorr.

For HfO_2 CVD at 300°C, the $Hf(O^tBu)_4$ precursor bottle was heated to 36°C. The two pneumatic valves in series were employed to reduce the $Hf(O^tBu)_4$ pulse precursor, both were set to have an opening times of 500 ms. After the first pneumatic valve opening, $Hf(O^tBu)_4$ gas would flow into the fixed volume tube and be trapped for 10 s. The precursor gas was released by the second pneumatic valve opening with a pressure spike of 0.3 mTorr. Between each fixed volume

pulsing, there would be a 60 s purge time. A continuous flow of N_2 purge gas was implemented. For Al_2O_3 CVD, the sample stage was heated up to 330°C. The ATSB precursor bottle was heated to 110°C. ATSB dosing line pneumatic valve had an opening time of 200 ms with 10s purge time between pulses. Each pulse achieved a pressure spike of 0.02 mTorr. During the CVD process, a continuous flow of N_2 purge gas was employed. For TiO_2 CVD, the sample stage was heated to 300°C. $Ti(O^iPr)_4$ precursor bottle was kept at room temperature. A pressure spike of 0.1 mTorr was achieved with 200 ms opening time and 5 s purge time between pulses. Continuous N_2 gas was employed.

Deposition Characterization

Samples were transferred *in-vacuo* to the UHV chamber after deposition. X-ray photoelectron spectroscopy (XPS) was used to perform a compositional study. The XPS system included a monochromatic Al Kα X-ray source (E = 1487 eV) and a hemispherical analyzer (XM 1000 MkII/SPHERA, Omicron Nanotechnology) with a pass energy of 50 eV employed. The XPS anode voltage was set to 10 kV, and the filament emission current was set to 25 mA. All XPS data collected was analyzed by the Casa XPS v2.3 program. *Ex-situ* characterization studies include atomic force microscopy (AFM), ellipsometry, transmitted electron microscopy (TEM) and electron energy loss spectroscopy (EELS).

2.3 Result and Discussion

Aniline passivation Aniline passivation at different temperature & on different metal surfaces (W and Co)

The water-free single precursor HfO_2 CVD was performed on HF-cleaned SiO_2, degreased W, and degreased Co at 300°C. W and Co are metals known to be easily oxidized and have surface

hydroxyl groups. These surface hydroxyl groups will induce the unwanted growth of HfO_2 on these two metals.

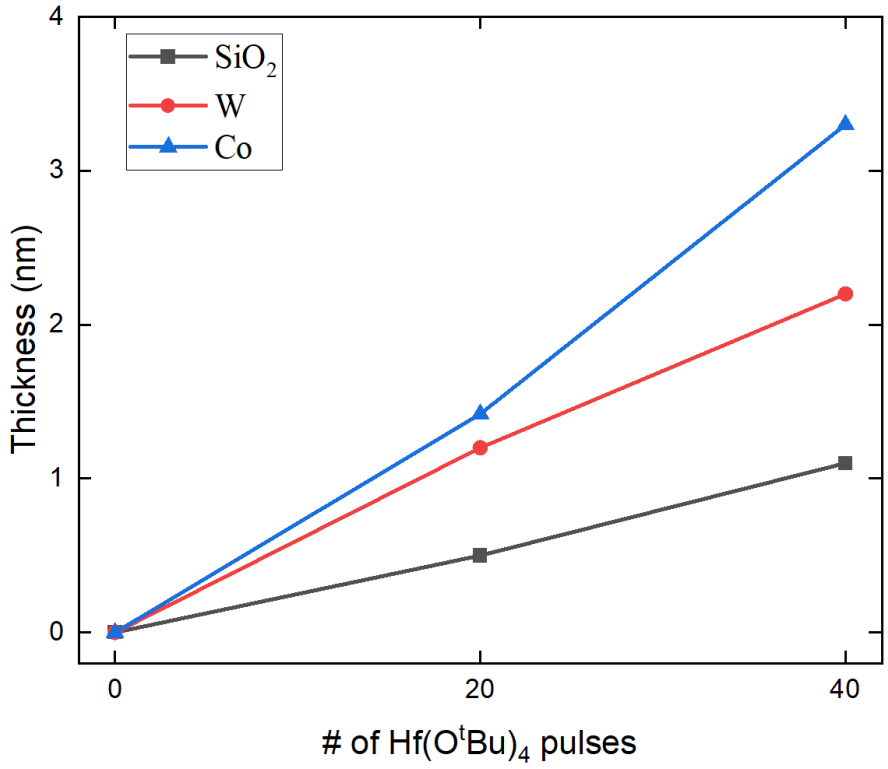

Figure 2.2. HfO_2 growth curve on SiO_2 vs. metals (W, Co). Water-free single precursor HfO_2 CVD has around 2-3 times faster growth on metals compared to SiO_2.

Fig. 2.2 shows the growth rate of the water-free single precursor HfO_2 CVD on unpassivated SiO_2, W, and Co surfaces. After 20 pulses of $Hf(O^tBu)_4$, deposition thicknesses (derived from the equation between the inelastic mean free path and the signal attenuation length of an electron from the substrate) are around 1.4 nm, 1.2 nm and 0.5 nm on Co, W, and SiO_2 respectively. After a total of 40 pulses, there are 3.3 nm and 2.2 nm on Co and W while only 1.1 nm deposition on SiO_2. Without passivation, HfO_2 deposition growth on Co is around 3 times faster than SiO_2. Growth on W is around 2 times faster compared to SiO_2. The different growth rates correspond to the oxide bond strength. Cobalt-oxygen bond has the lowest bond energy while silicon-oxygen bond possesses the highest bond strength [29]. In sum, precursor molecules more

readily chemisorb on the metal surfaces; consequently, SAM or small organic molecules are required to reverse the selectivity.

Merkx et al. performed aniline passivation at the same substrate temperature (250 ^{o}C) as their TiN ALD process. Based on Merkx's paper, aniline passivated at 250°C rendered a satisfactory inhibition of ALD growth on the unwanted area. As a result, aniline passivation at 250°C was conducted. Samples were trapped in the aniline gas with a pressure of 760 mTorr for 40 minutes and then followed by $Hf(O^tBu)_4$ dosing at 300°C.

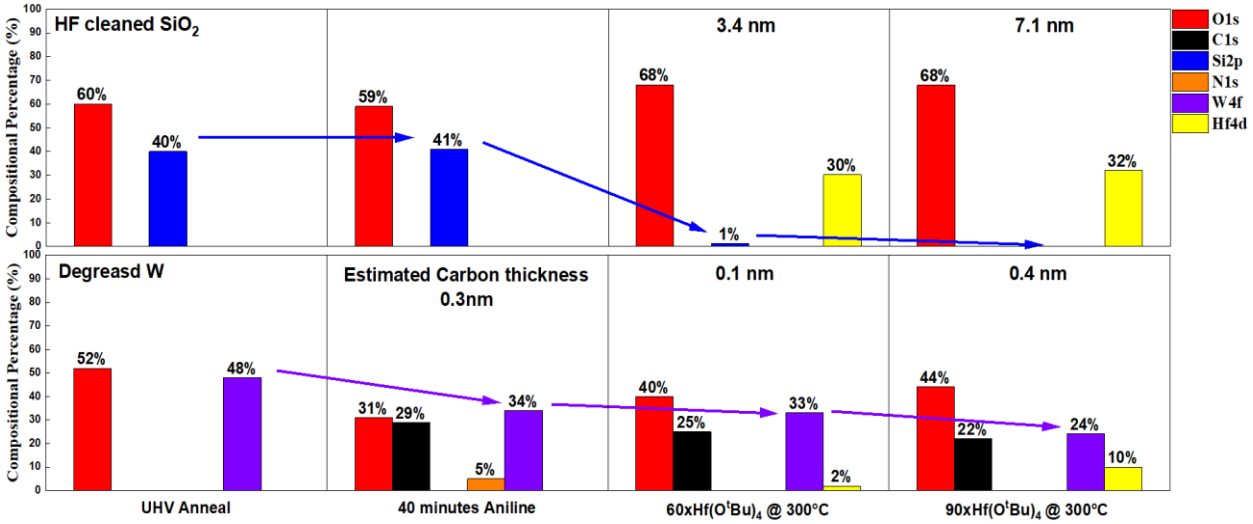

Figure 2.3. Selective 300°C HfO_2 CVD on SiO_2 in preferent to W with 250°C aniline passivation. Raw data can be found in support information Fig. 2.15.

Selective passivation was achieved on W versus SiO_2 (Fig. 2.3). After the aniline passivation, on the W sample, C_{1s} peak increased from 0% to 31%, W_{4f} decreased from 48% down to 34% while no compositional signal changed on SiO_2. After aniline passivation, a N_{1s} signal also appeared on W. After 60 pulses of $Hf(O^tBu)_4$, around 3.4 nm was selectively deposited on SiO_2 while 0.1 nm on W. With an additional 30 pulses of $Hf(O^tBu)_4$, around 7.1 nm (measured by ellipsometry) of HfO_2 was deposited on SiO_2 while only 0.4 nm was deposited on W. Compared to unpassivated W, HfO_2 growth after 60 pulses was inhibited for more than 4.5 nm deposition.

Since most of the selective pulsed metal oxide CVD reactions occur at 300°C, the aniline passivation at 300°C was also studied.

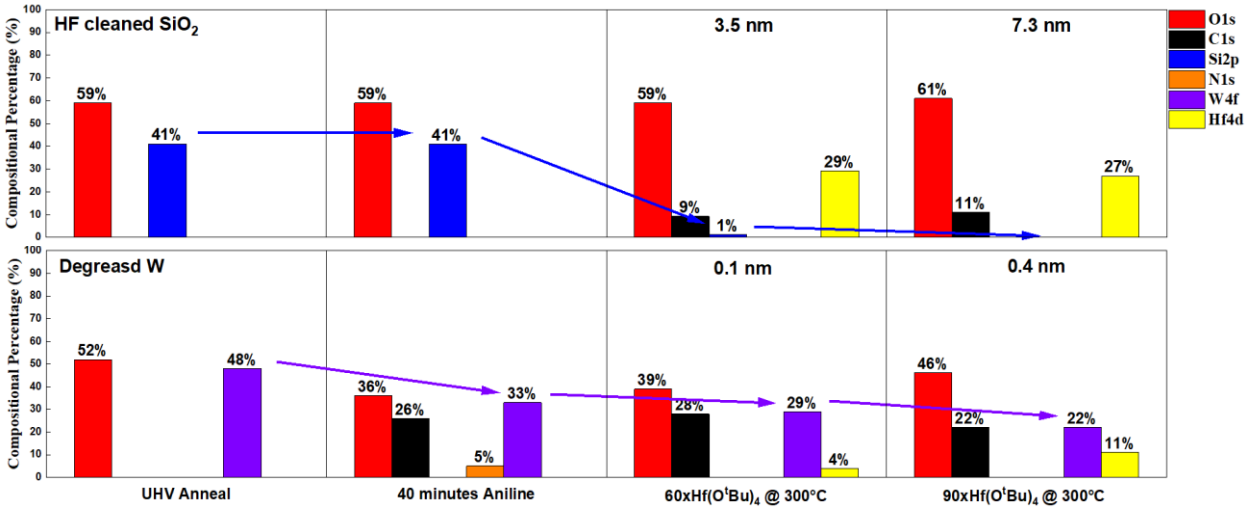

Figure 2.4. Selective 300°C HfO_2 CVD on SiO_2 in preference to W with 300°C aniline passivation. Raw data can be found in support information Fig. 2.16.

Fig. 2.4 shows the XPS chemical composition of HF cleaned SiO_2 and degreased W as loaded after a 300°C rapid UHV anneal, after 40 minutes 300°C aniline passivation, and after the pulsed CVD HfO_2 deposition. After aniline passivation, XPS shows that on the W sample, C_{1s} increased from 0% to 26% and W_{4f} decreased from 48% down to 33% which are similar compared to the 250°C aniline passivation. This indicated selective passivation was achieved even at 300°C. Both aniline passivation at 250°C and 300°C result in a saturated 0.3 nm of carbon monolayer on the W surface. After a total of 100 pulses of $Hf(O^tBu)_4$, similar selectivity was achieved with 7.3 nm HfO_2 deposited on SiO_2 while only 0.4 nm on W. This indicated no passivation difference between 250°C and 300°C substrate temperature.

For an effective precursor blocking, both chemical passivation and steric shielding effect need to be considered. For a larger passivant size, steric shielding becomes more prominent [30]. If surface roughness is high, passivant molecules cannot be compactly packed, which leads to a gap between passivant molecules and an early loss in selectivity. The same 300°C passivation and

HfO_2 CVD processes were performed on a rough sputtered W with an RMS roughness of 2.4 nm (W received from AMAT has an RMS roughness of 0.4 nm). Selectivity significantly decreased on the sputtered W due to an increase in RMS roughness (see support information Fig. 2.17).

The passivation process employed in the above experiments included aniline gas being trapped in the deposition chamber for 40 minutes at 300°C. A 60-minute trapping time aniline passivation at 300°C with HfO_2 deposition was shown in support information Fig. 2.18. Carbon content and selectivity were the same compared to the 40 minutes passivation. Therefore, 40 minutes trapping time ensured the saturation of passivation.

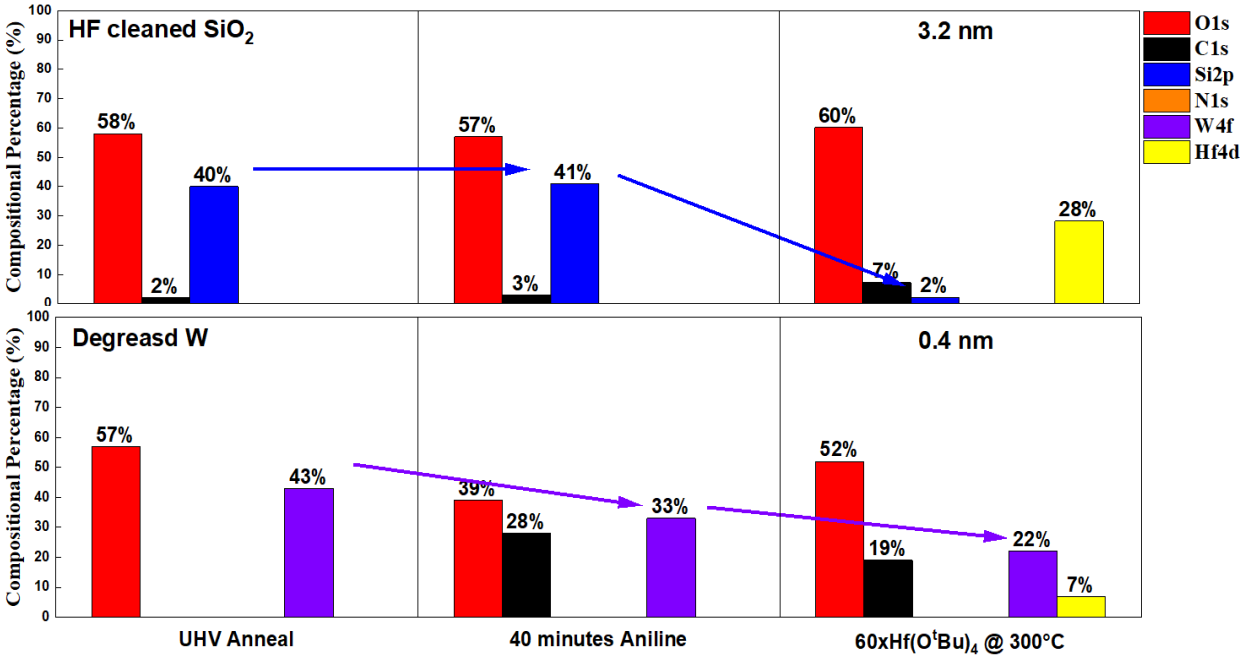

Figure 2.5. Selective 300°C HfO_2 CVD on SiO_2 in preferent to W with 350°C aniline passivation. Raw data can be found in support information Fig. 2.19.

40 minutes 350°C aniline passivation with HfO_2 CVD at 300°C was also studied on HF-cleaned SiO_2 and degreased W as shown in Fig. 2.5. The C_{1s} XPS percentage of the W sample shows a similar percentage increase after aniline dosing compared to the passivation at 250°C and 300°C. Despite the same amount of carbon content initially deposited on the W surface, the C_{1s} percentage decreased noticeably by 9% (28% to 19%) for only a total of 50 $Hf(O^tBu)_4$ pulses. For

the 250°C and 300°C aniline passivation, C1s only went down to 22% after 100/90 $Hf(O^tBu)_4$ pulses. The loss in passivation ability of the 350°C aniline process could be due to two possible reasons. The diffusion increase resulting from the elevated temperature leads to non-compact aniline monolayer packing resulting in less steric shielding effect and lower selectivity. No N_{1s} peak was observed for the W sample after aniline passivation. At 350°C, aniline might undergo additional decomposition leading to weak bonding or physisorption between decomposed carbon species and the W surface (without a strong N-metal bond). These weakly bonded carbon species will be easily displaced by the precursor from the pulsed CVD processes. Since aniline has the best passivation performance at 250°C and 300°C, the 300°C aniline passivation process was employed for additional experiments to maintain the same or similar substrate temperature throughout the experiment.

The optimal passivation and CVD processes were applied on a degreased Co to study the effect of different substrates on the passivation performance.

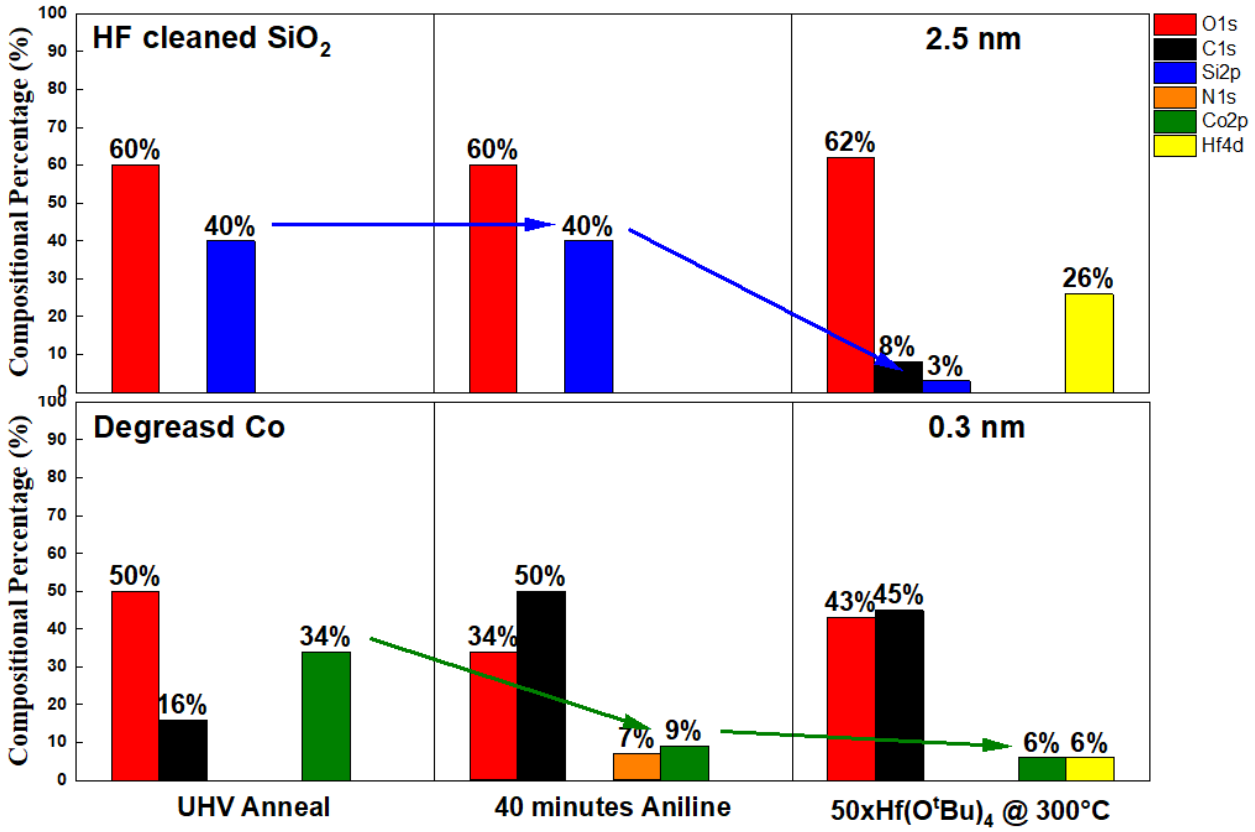

Figure 2.6. Selective 300°C HfO_2 CVD on SiO_2 in preference to Co with 300°C aniline passivation. XPS raw data can be found in support information Fig. 2.20.

After aniline passivation, XPS showed significant increase in the C1s peak only on Co and not on SiO_2 in Fig. 2.6. C_{1s} of Co increased from 16% to 50%, Co_{2p} decreased from 34% to 9%. Despite a higher carbon content increase, after a total of 50 pulses of single precursor $Hf(O^tBu)_4$ CVD, only 2.5 nm was selectively deposited on SiO_2 while 0.3 nm on Co.

The aniline passivated W showed a higher selectivity than aniline passivated Co. This is consistent with the weaker surface oxygen bond (higher surface reactivity) of Co compared to W [29]. According to the DFT calculation from Merkx et al., aniline undergoes two main types of adsorption on metal surfaces [31]. In the first mechanism, aniline absorbs onto metal surfaces through its amine group by forming a N-metal bond. In the second mechanism, aniline bonds to metal surfaces through its phenyl ring with C-metal bonds. Based on the bond dissociation

enthalpies, W holds a stronger bond with N and C compared to Co [32-34]. This leads to a stronger passivation on W which corresponds to the higher selectivity observed in the previous studies.

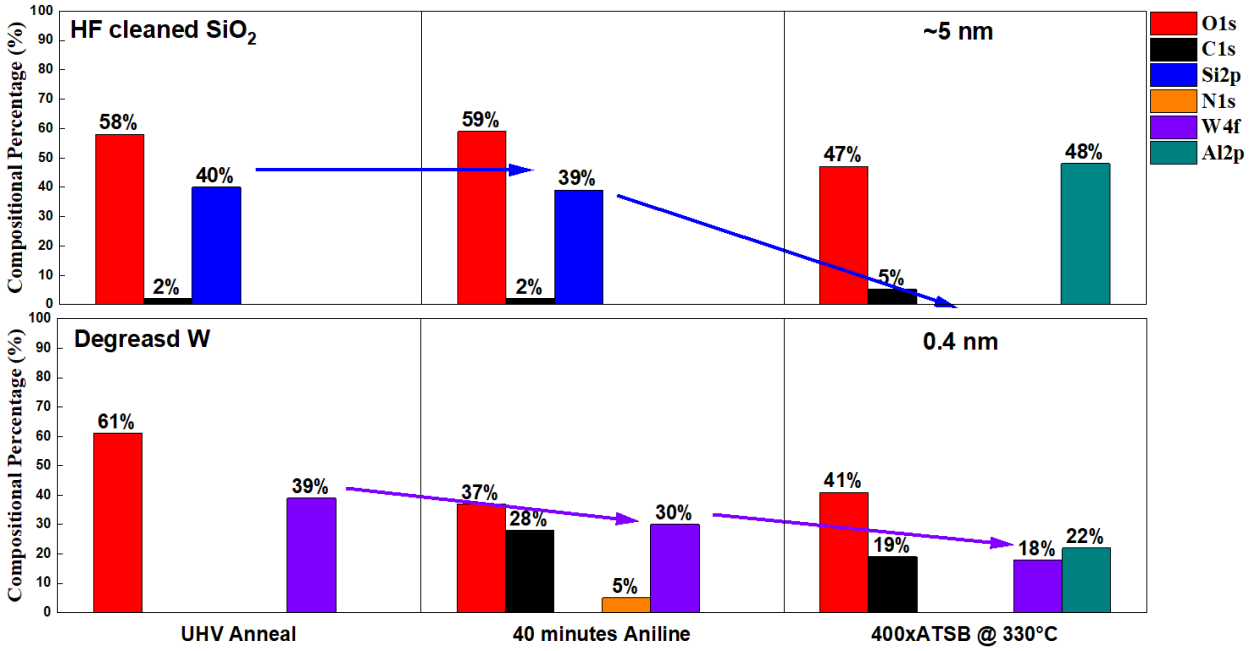

Figure 2.7. Selective Al_2O_3 330°C CVD on SiO_2 in preferent to W with 300°C aniline passivation. Raw data can be found in support information Fig. 2.21.

A 330°C single precursor Al_2O_3 CVD process using ATSB was also tested with aniline passivation (XPS shown in Fig. 2.7). Due to ATSB's higher decomposition temperature, a substrate temperature of 330°C was required in the ATSB CVD process to achieve an adequate growth rate. After a total of 400 ATSB pulses, around 5 nm Al_2O_3 was selectively deposited on HF SiO_2 in preference to W (0.4 nm). A 300°C ATSB process after the aniline passivation was shown in Fig. 2.22. Around 3.6 nm of Al_2O_3 was deposited on SiO_2 while 0.4 nm on W after a total of 640 pulses of ATSB. Based on the XPS data, the lower substrate temperature of ATSB process resulted in a lower selectivity due to the limited Al_2O_3 growth at 300°C. A higher number of ATSB pulses was required to deposit the same thickness and resulted in a higher chance of displacing the surface aniline group. The displacement rate depends on the reactivity of the precursor. One typical example is trimethylaluminum (TMA), TMA is too reactive to be blocked

by aniline [23]. By comparing the selectivity result between the 330°C and 300°C ATSB processes, the aniline passivation process is thermally stable at 330°C and compatible with the 330°C ATSB CVD process.

In addition, the compatibility test of the 300°C aniline passivation with the single precursor TiO_2 CVD process at 300°C was conducted (as shown in Fig. 2.23). Around 5.1 nm of TiO_2 was grown on HF cleaned SiO_2, while only 0.3 nm of TiO_2 was deposited on W.

Mechanism & Nanoselectivity tests

A proposed mechanism of the water-free single precursor CVD processes with aniline passivation is shown in Fig. 2.8. Aniline selectively forms a thermodynamically favorable N-metal bond on the W surface. It is hypothesized that with the help of the hydrophobic phenyl ring and its steric shielding, CVD precursors only physiosorb on W and desorb at 300°C. Conversely, CVD precursors chemisorbed onto the SiO_2 surface by reacting with the surface hydroxyl reactive sites. Precursors decompose at 300°C/330°C to generate more hydroxyl groups for the sequential pulsing. Thus, continuous CVD growth only occurs on SiO_2 while W remains passivated without deposition.

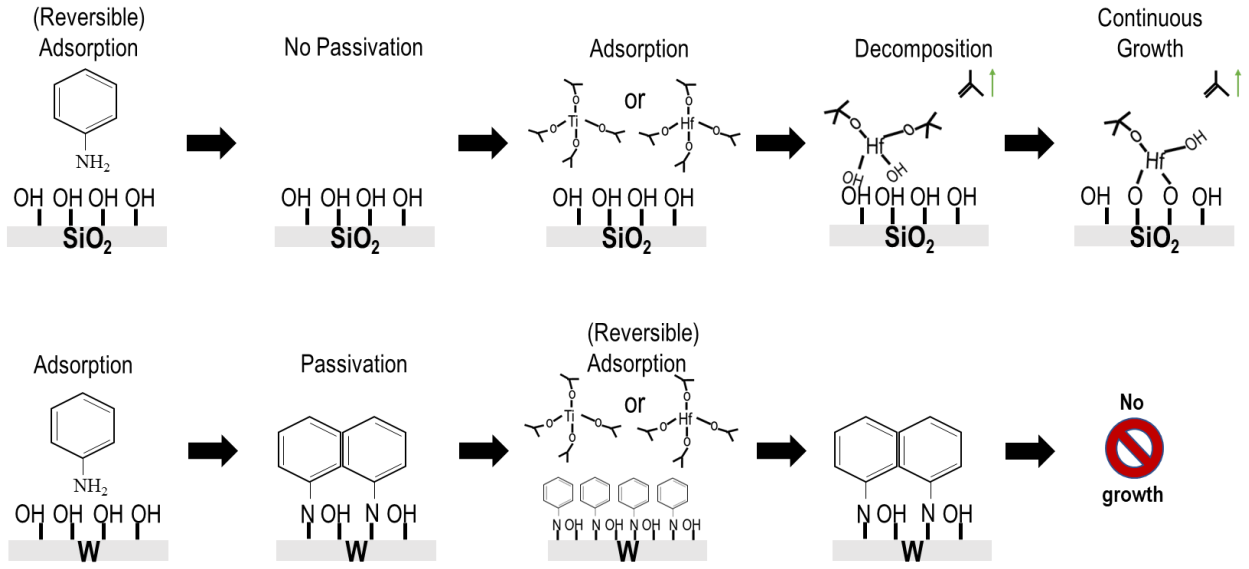

Figure 2.8. Proposed mechanism of water-free selective single precursor CVD on SiO_2 in preferent to W with 300°C aniline passivation.

As shown above, selective pulsed CVD HfO_2 and Al_2O_3 on blanket SiO_2 in preference to W is documented, but selectivity on the nanoscale can be more challenging since reaction product can diffuse from passivated to unpassivated surfaces. W/SiO_2 patterned samples with a 55 nm pitch size and a linewidth of 30 nm were used to test the nanoselectivity of HfO_2 and Al_2O_3 CVD processes with aniline passivation independently. A W control sample was loaded together with the W/SiO_2 to ensure no HfO_2 deposition on the W region of the patterned sample.

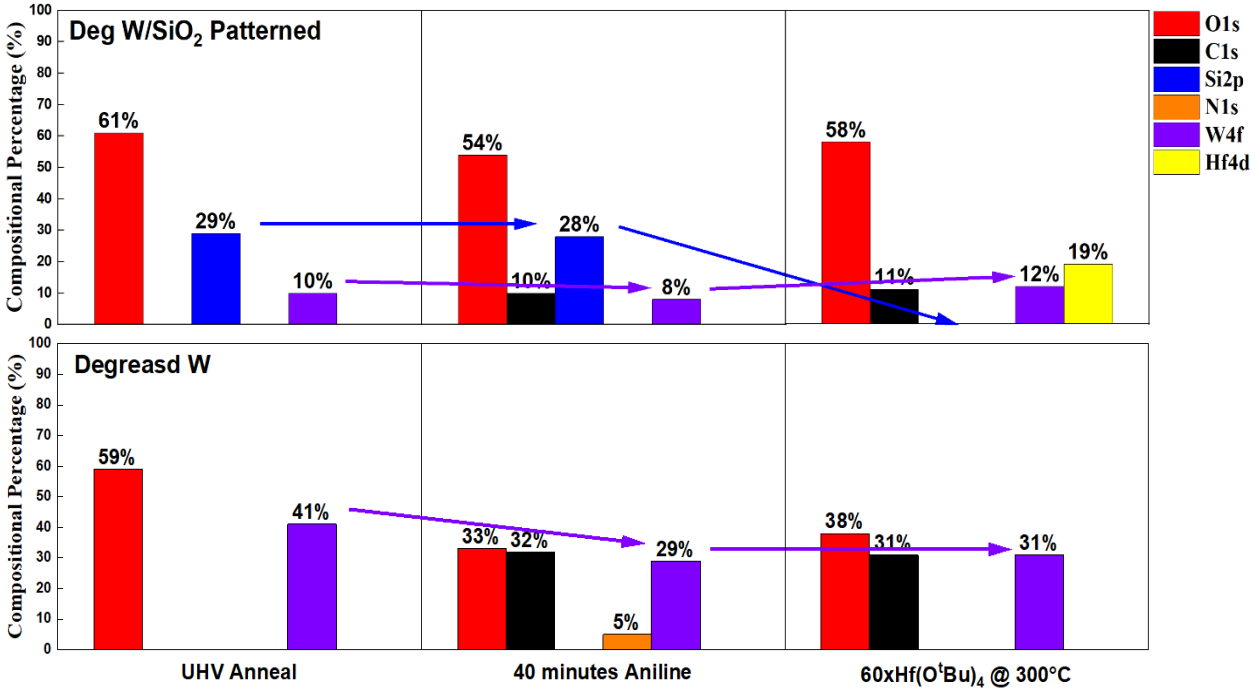

Figure 2.9. Selective 300°C HfO_2 CVD on SiO_2 region of W/SiO_2 patterned sample with 300°C aniline passivation. Raw data can be found in support information Fig. 2.24.

From the XPS in Fig. 2.9, around one monolayer aniline was selectively deposited on W sample surface after the 40-minute aniline passivation. For the patterned sample, Si_{2p} signal remained unchanged. The C_{1s} peak compositional percentage increased only from 0% to 10% which is reasonable since the XPS spectra was taken from an array of W and SiO_2 regions. W_{4f} decreased from 10% to 8% which could be due to the monolayer aniline coverage. No N_{1s} signal was observed from the patterned sample due to the N_{1s} signal being below the XPS detection limit. To prevent overgrowth and secure a clean W region surface, a total of 60 pulses of $Hf(O^tBu)_4$ (less than the number tested on the blanket sample) were employed. W_{4f} signal increased from 8% to 12%, this could be due to a different XPS scan region on the patterned sample. Due to micron-size scanning limitation, it became difficult to focus on the exact same W/SiO2 arrays (nanometer-scale) that has been studied previously. No W signal attenuation was observed on both samples

and no Hf_{4d} signal was detected on the W sample. This indicates a clean and pristine W surface on both the patterned sample and degreased W.

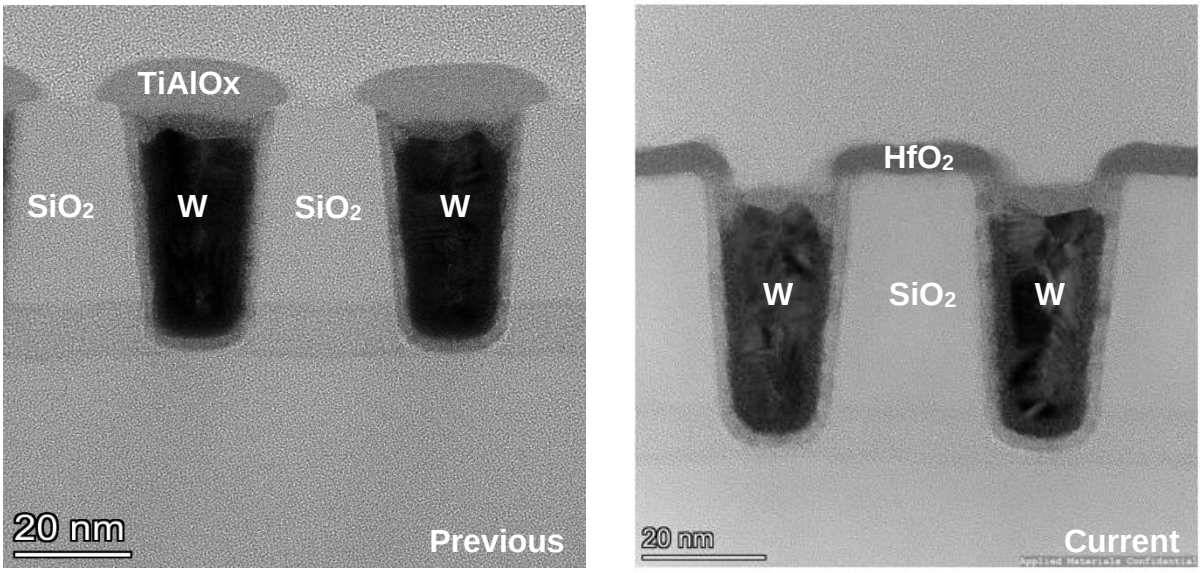

Figure 2.10. Left: TEM image of a selective 300°C TiAlOx CVD deposition (previously reported) on W region in preference to SiO_2 [35]. Right: selective 300°C HfO_2 CVD process on SiO_2 region of W/SiO_2 patterned sample with the help of 300°C aniline passivation.

After the HfO_2 CVD deposition with aniline passivation, TEM was performed on the patterned sample. Compared to our previously reported selective TiAlOx deposition on W in preference to SiO_2, around 5.5 nm of HfO_2 was selectively deposited on SiO_2 region and no deposition was observed on the W region. As shown in Fig. 2.10, HfO_2 deposition on SiO_2 was uniform and smooth.

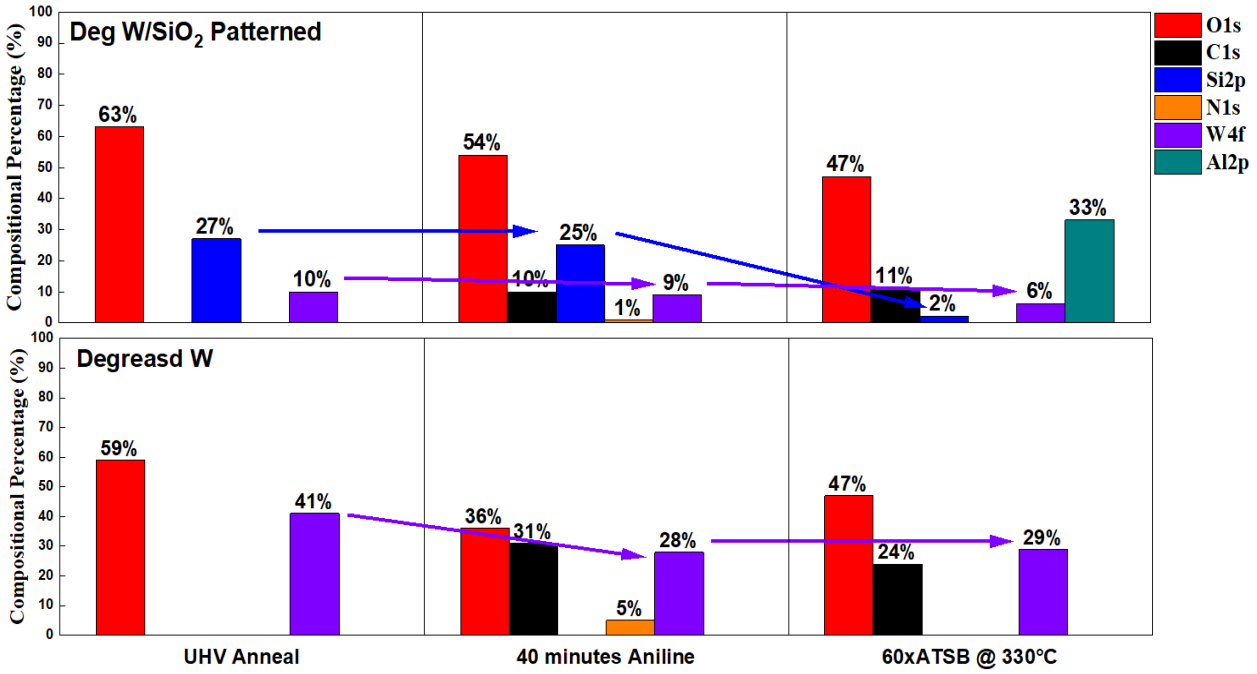

Figure 2.11. Selective 330°C Al_2O_3 CVD on SiO_2 region of W/SiO_2 patterned sample with 300°C aniline passivation. Raw data can be found in support information Fig. 2.25.

As shown in Fig. 2.11, similar XPS results were observed for the ATSB process. Both W/SiO_2 patterned and W samples started with no carbon content on the surface. After the 40-minute aniline passivation, around 10% carbon content on the patterned surface was recorded and around 0.3 nm aniline on the blanket W was detected. Only 200 pulses of ATSB were dosed onto the samples to minimize overgrowth on the W region of the patterned sample. After ATSB dosing, Si_{2p} signal from the patterned sample decreased from 27% to 2%, and the Al_{2p} signal increased from 0% to 33% while only a 3% decrease was observed for W_{4f}.

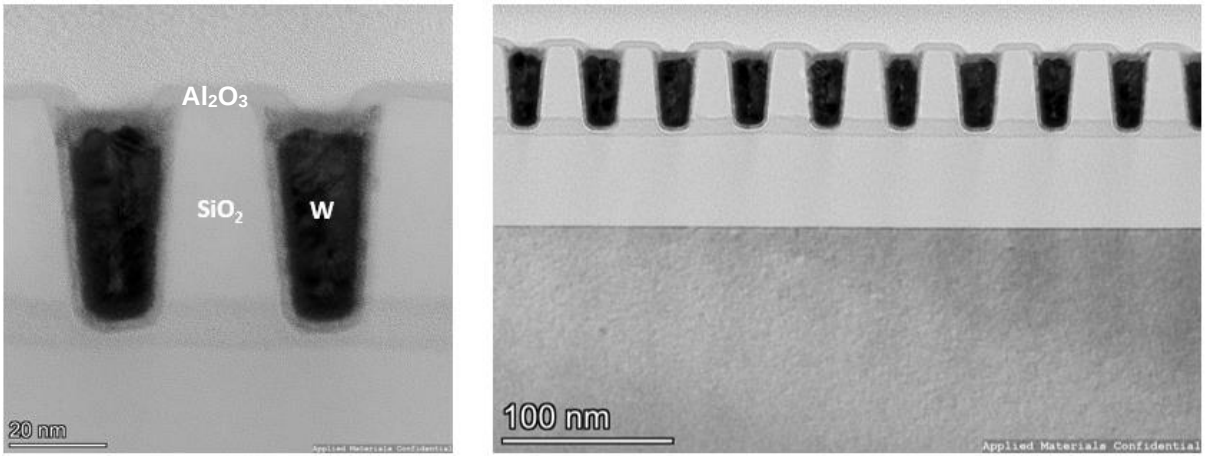

Figure 2.12. TEM images of the selective 330°C Al_2O_3 deposition on SiO_2 region of W/SiO_2 patterned sample with the help of 300°C aniline passivation.

As shown in Fig. 2.12, TEM was performed on the W/SiO_2 patterned sample after the deposition. Around 4 nm of Al_2O_3 was achieved on SiO_2 surface while W surface remained pristine. A little overgrowth of the Al_2O_3 was observed and covered a portion of the W surface. This overgrowth corresponds to the 3% attenuation in the W_{4f} signal.

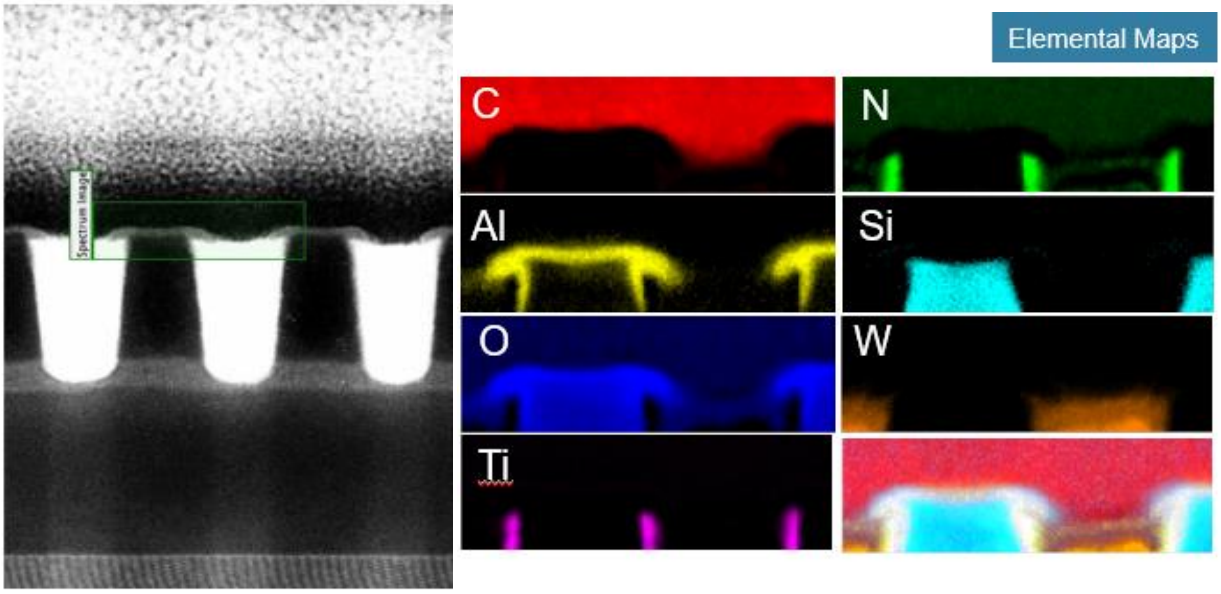

Figure 2.13. EELS element study proved Al_2O_3 was selectively deposited on SiO_2.

EELS was also performed to characterize and identify the surface elements. From Fig. 2.13, Al signal only appeared on SiO_2 regions which indicated selective deposition. Al elemental

mapping also showed the overgrowth of Al_2O_3. This might be due to the W recess caused by the early CMP process. According to the TEM, around 4 nm of WOx was observed on the W surface. This surface WOx provides the necessary reactive hydroxyl sites for the CVD processes. The selectivity of the process might increase if this WOx layer is removed in-situ. From the TEM, the Al_2O_3 surface is smooth and uniform though out the whole sample. Both HfO_2 and Al_2O_3 processes can be used for DOD depending on the preferred k value.

2.4 Conclusion

Water-free single precursor CVD tends to grow faster on metal surfaces compared to dielectric surfaces. Aniline can selectively passivate metal surfaces by forming thermodynamically favorable amine metal bonds. The CVD inhibition ability possessed by aniline depends on both chemical passivation and steric shielding effects. Aniline readily passivates W surfaces due to strong bonding and low surface roughness. Aniline passivation can be carried out at 250°C or 300°C, but becomes thermally unstable at 350°C with weaker CVD inhibition ability. With aniline passivation, selective HfO_2, Al_2O_3, and TiO_2 were achieved on HF-cleaned SiO_2 in preference to degreased W by the water-free single precursor CVD using $Hf(O^tBu)_4$, ATSB, and $Ti(O^iPr)_4$ as the reactants respectively. Passivation with the ATSB CVD process proved that aniline can be compatible with processes up to 330°C. HfO_2 and Al_2O_3 nanoselectivity tests were demonstrated on the W/SiO_2 patterned samples. Both processes showed a selective smooth thin film achieved on SiO_2 regions only. With the help of aniline passivation at 300°C, these water-free single precursor CVD processes can be the potential solution for BEOL DOD applications.

2.5 Supporting Information

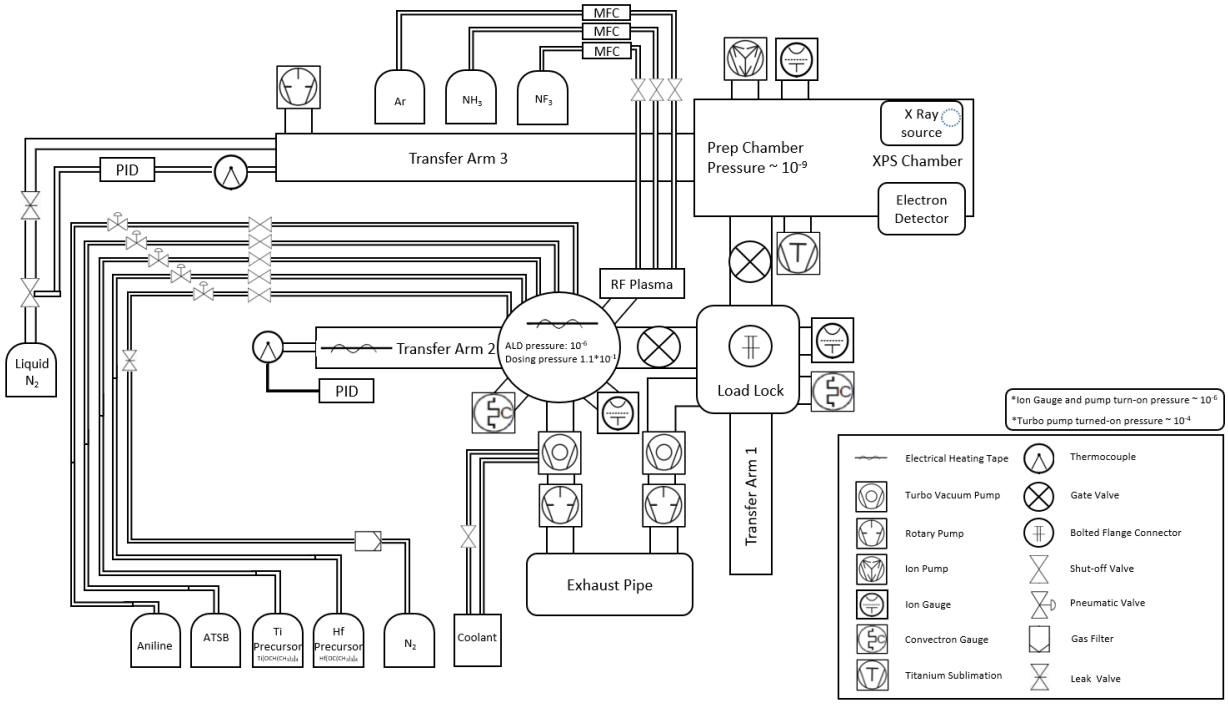

Figure 2.14. Schematic diagram illustrates the custom-built ALD/CVD with in-situ XPS system.

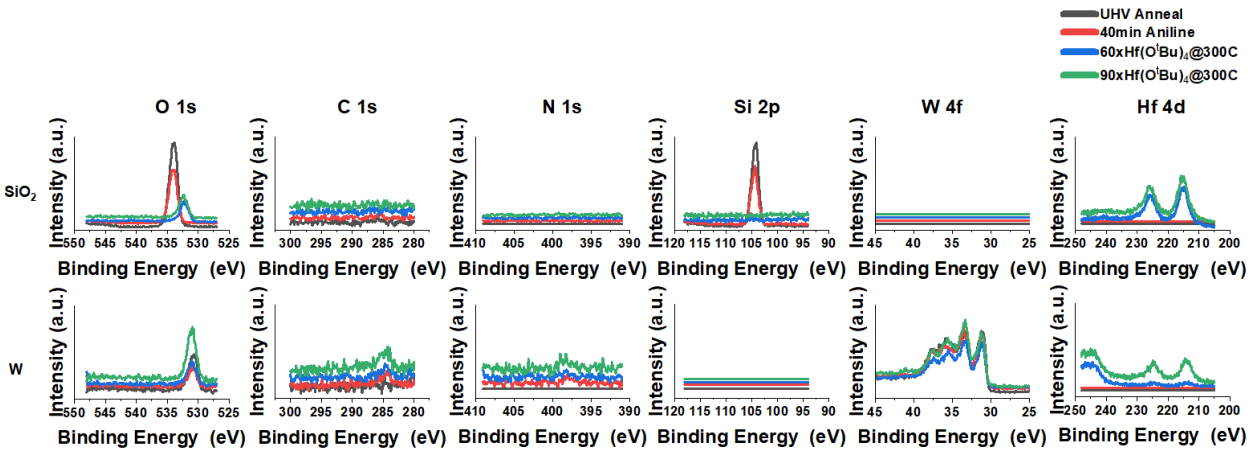

Figure 2.15. Raw XPS spectra of selective 300°C HfO_2 CVD on SiO_2 in preferent to W with 250°C aniline passivation.

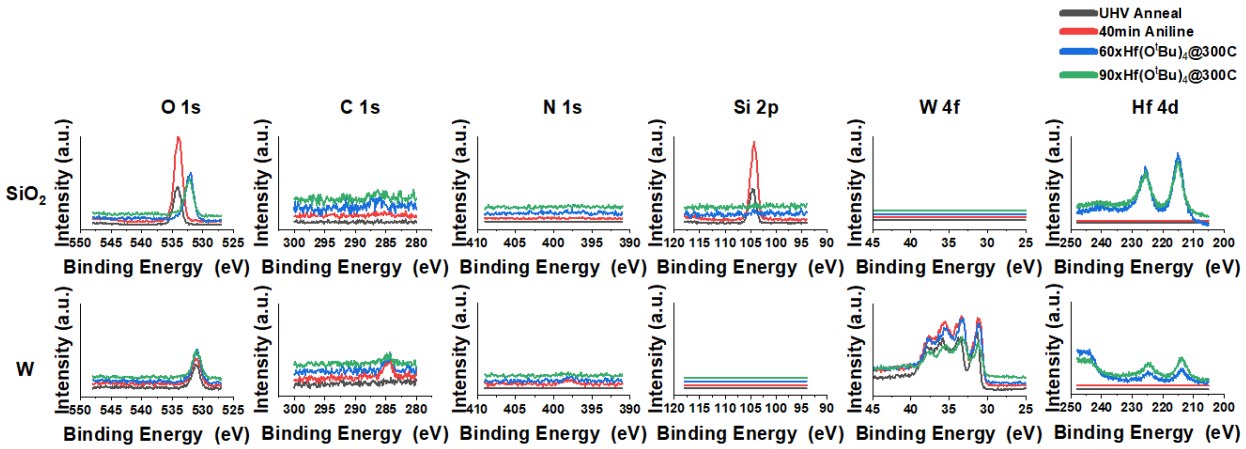

Figure 2.16. Raw XPS spectra of selective 300°C HfO_2 CVD on SiO_2 in preferent to W with 300°C aniline passivation.

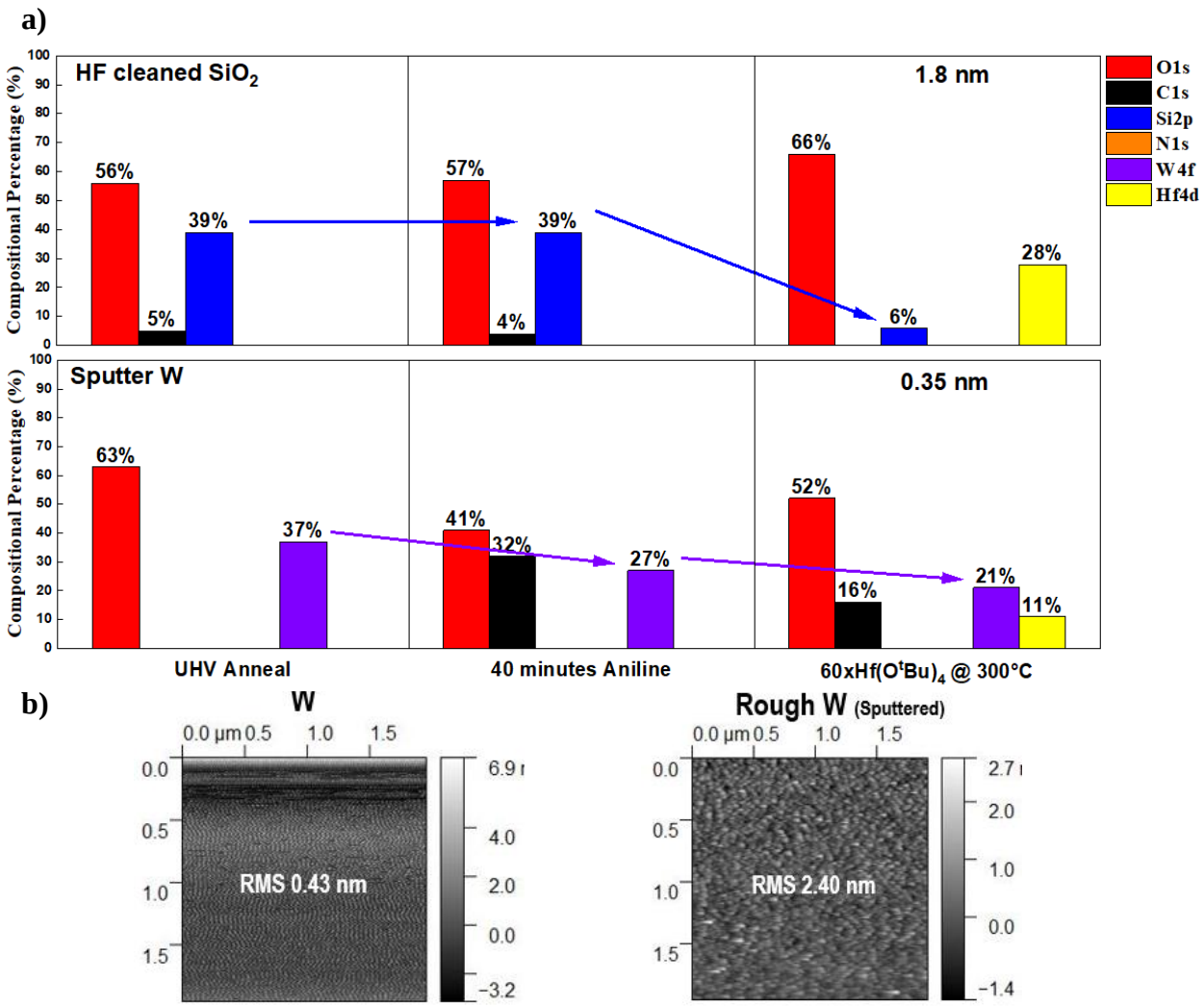

Figure 2.17. Selective 300°C HfO_2 CVD on SiO_2 in preferent to sputtered W with 300°C aniline passivation. a) XPS study on SiO_2 and sputtered W after each round of deposition. b) AFM images of W received from AMAT and sputtered W before deposition.

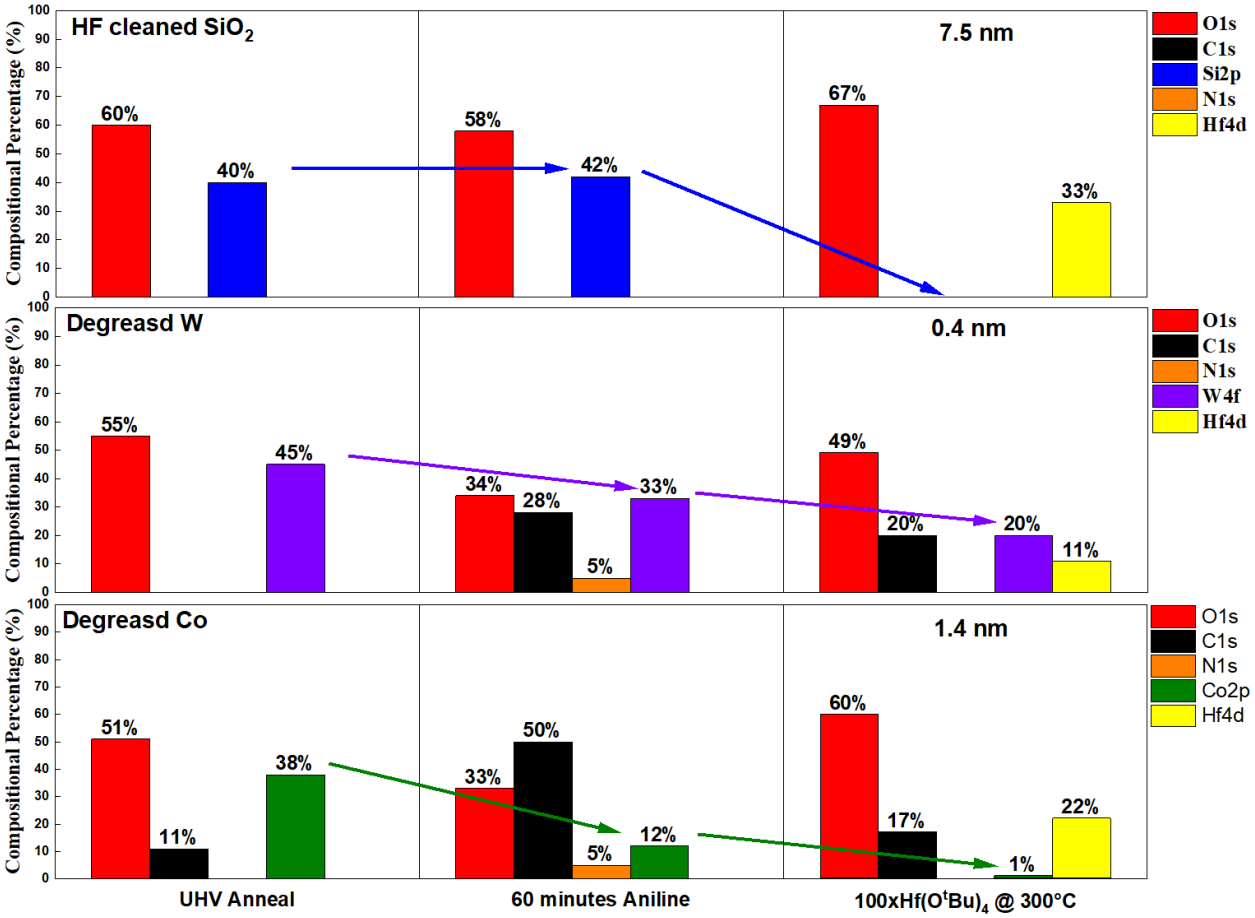

Figure 2.18. Selectivity study of single precursor HfO_2 CVD with 60-minute aniline passivation.

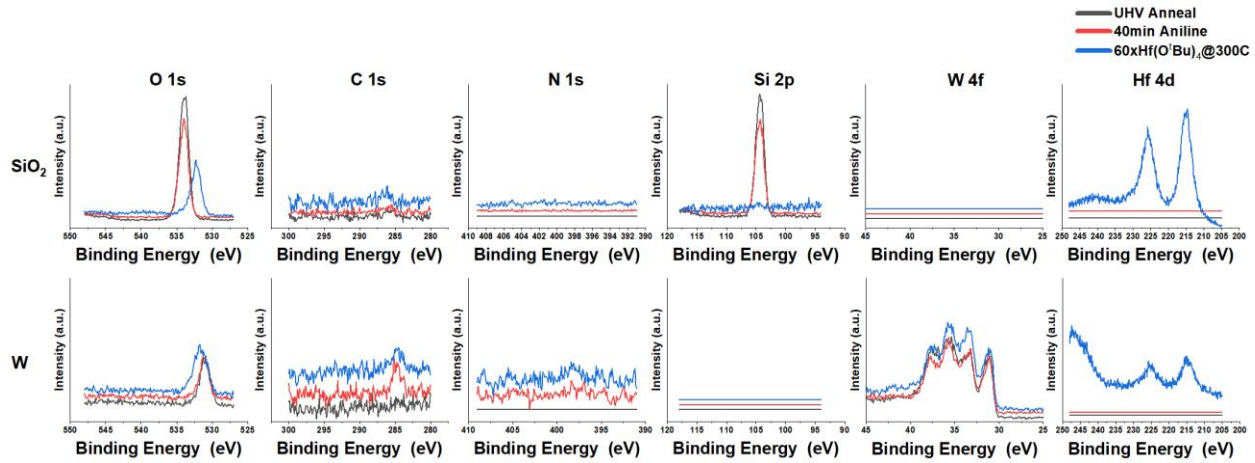

Figure 2.19. Raw XPS spectra of selective 300°C HfO_2 CVD on SiO_2 in preferent to W with 350°C aniline passivation.

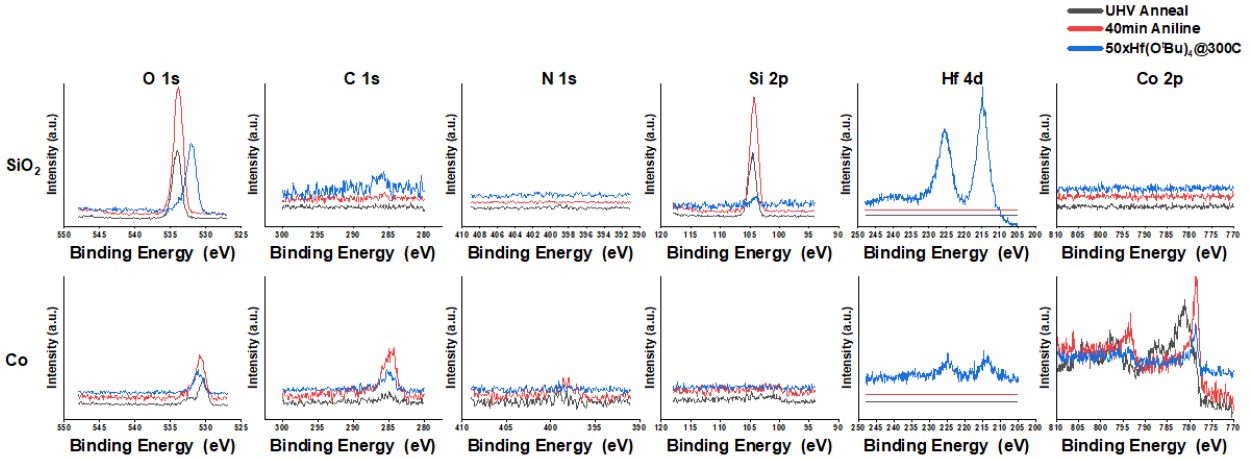

Figure 2.20. Raw XPS spectra of selective 300°C HfO_2 CVD on SiO_2 in preferent to Co with 300°C aniline passivation.

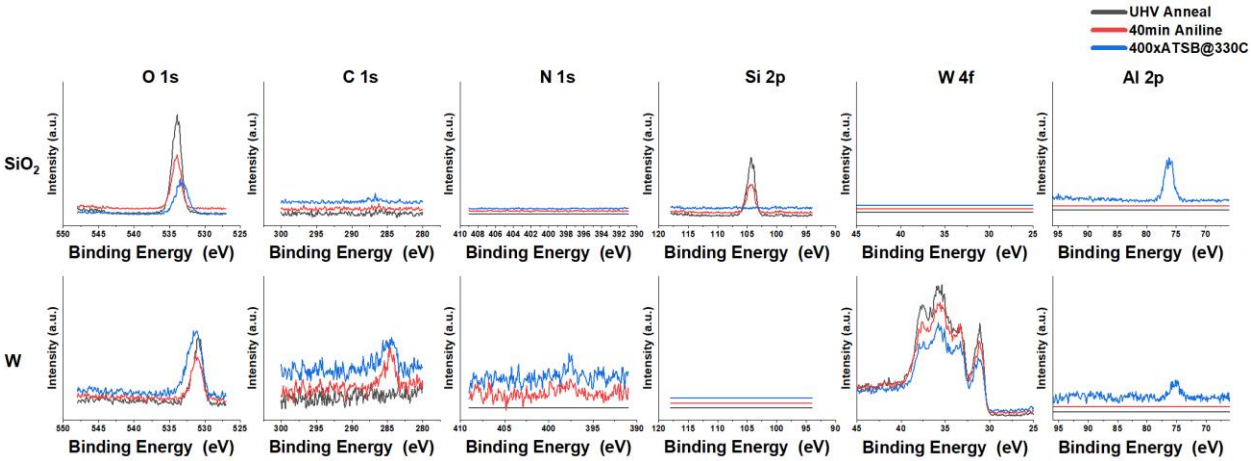

Figure 2.21. Raw XPS spectra of selective Al_2O_3 330°C CVD on SiO_2 in preferent to W with 300°C aniline passivation.

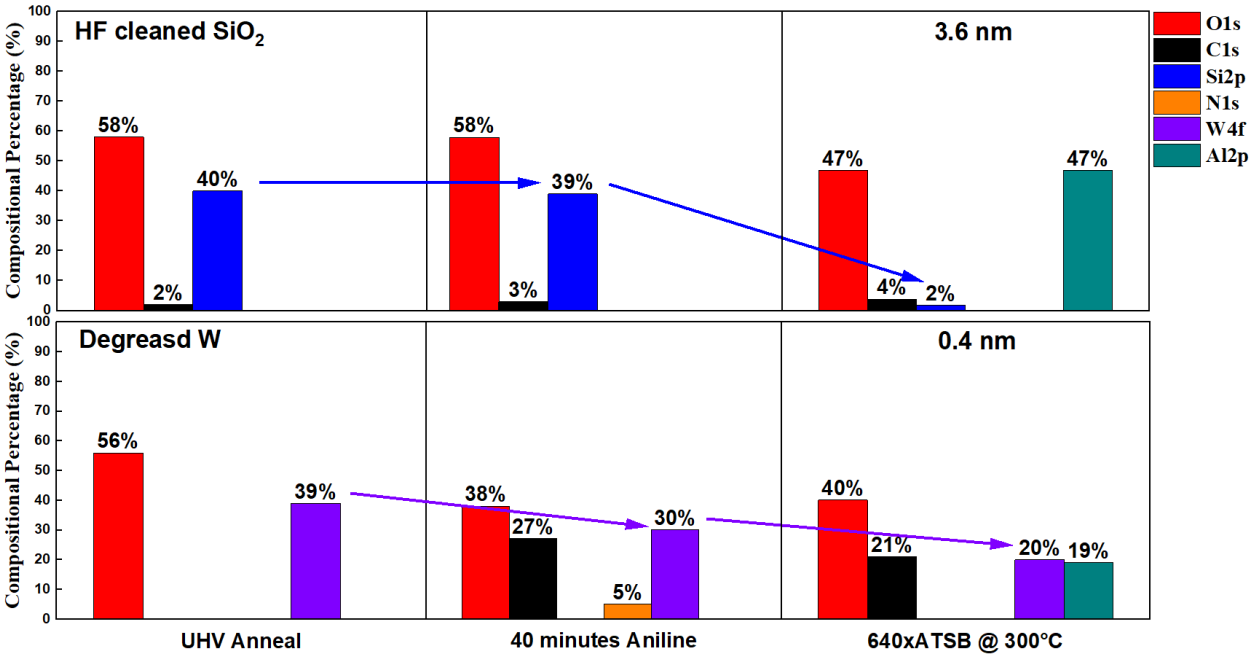

Figure 2.22. Selective Al_2O_3 300°C CVD on SiO_2 in preferent to W with 300°C aniline passivation.

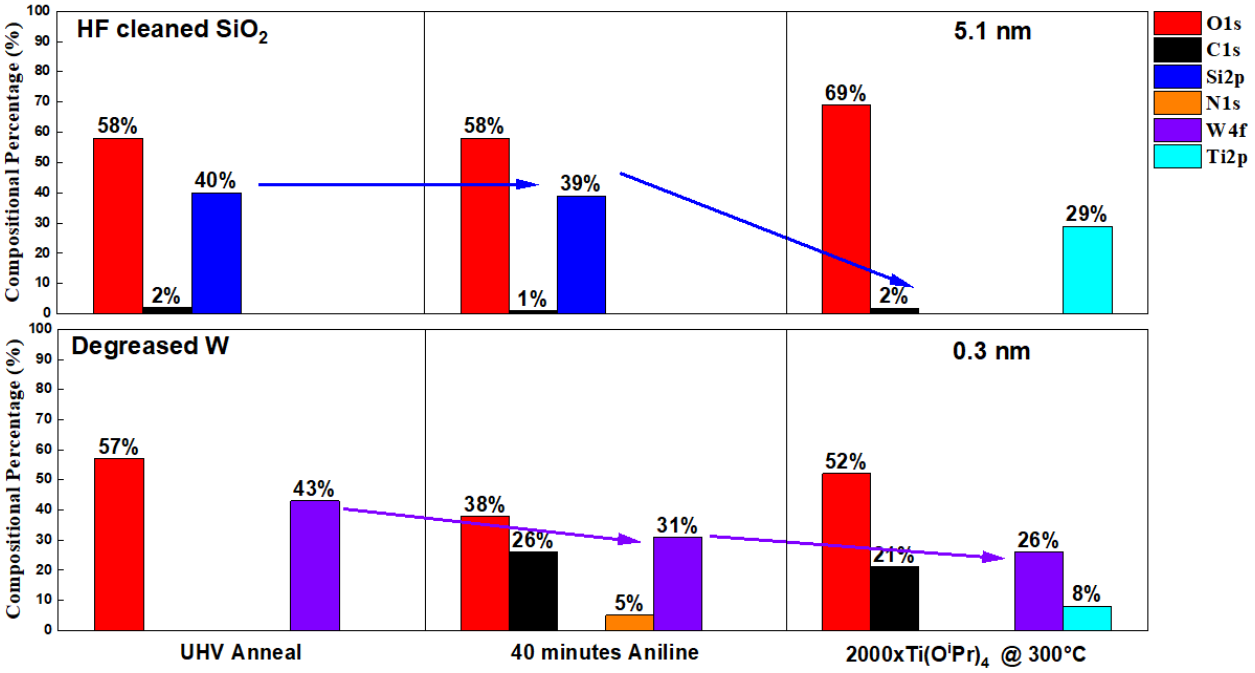

Figure 2.23. Selective 300°C TiO_2 CVD on SiO_2 in preferent to degreased W with 300°C aniline passivation.

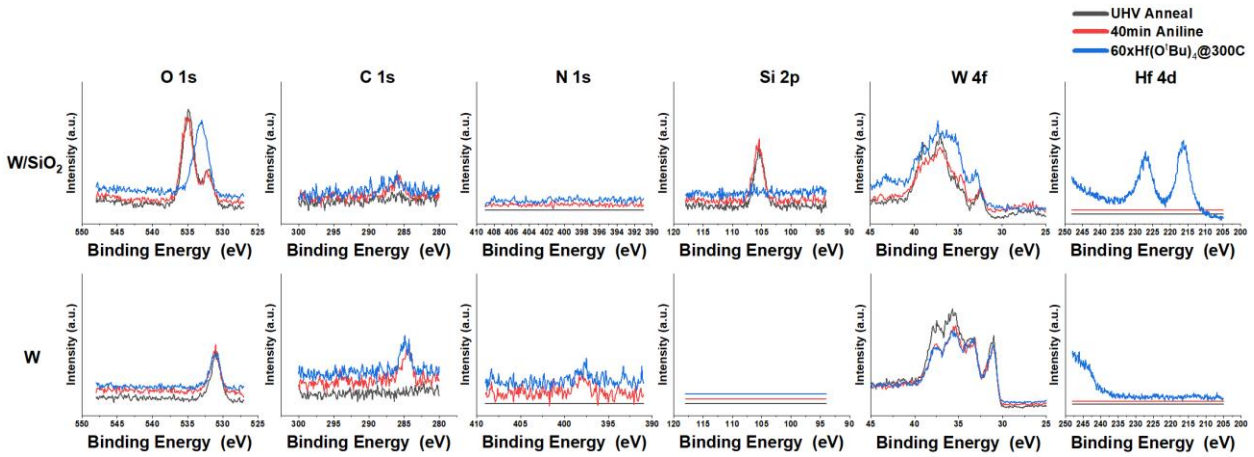

Figure 2.24. Raw XPS spectra of selective 300°C HfO_2 CVD on W region of W/SiO_2 patterned sample with 300°C aniline passivation.

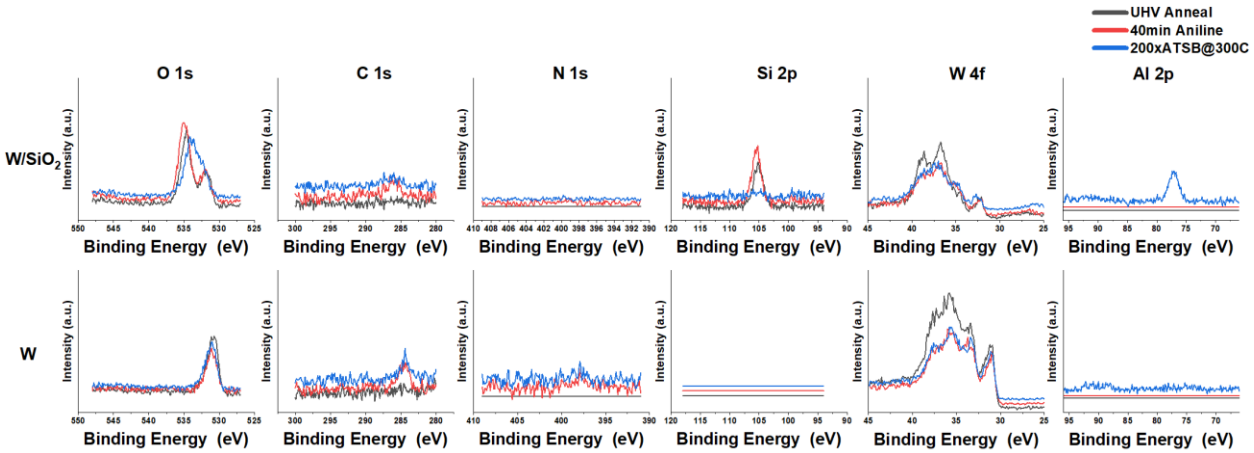

Figure 2.25. Raw XPS spectra of selective 330°C Al_2O_3 CVD on W region of W/SiO_2 patterned sample with 300°C aniline passivation.

2.6 References

1. Joyner, J.; Venkatesan, R.; Zarkesh-Ha, P.; Davis, J.; Meindl, J. Impact of Three-Dimensional Architectures on Interconnects in Gigascale Integration. IEEE Transactions on Very Large Scale Integration (VLSI) Systems, vol. 9, no. 6, pp. 922-928, Dec. 2001, doi: 10.1109/92.974905.

2. Joyner, J.; Zarkesh-Ha, P.; Meindl, J. A Stochastic Global Net-Length Distribution for A Three-Dimensional System-On-A-Chip (3D-SoC). *14th Annual IEEE International ASIC/SOC Conference (IEEE Cat. No.01TH8558)*, 2001, pp. 147-151, doi: 10.1109/ASIC.2001.954688.

3. Nahman, A.; Fan, A.; Chung, J.; Reif, R. Wire-Length Distribution of Three-Dimensional Integrated Circuits. *1999 IEEE International Interconnect Technology Conference (Cat. No.99EX247)*, 1999, pp. 233-235, doi: 10.1109/IITC.1999.787131.

4. Rahman, A.; Reif, R. System-Level Performance Evaluation of Three-Dimensional Integrated Circuits. *IEEE Transactions on Very Large Scale Integration (VLSI) Systems*, vol. 8, no. 6, pp. 671-678, Dec. 2000, doi: 10.1109/92.902261.

5. Pavlidis, V.; Friedman, E. Interconnect-Based Design Methodologies for Three-Dimensional Integrated Circuits. *IEEE*, vol. 97, no. 1, pp. 123-140, Jan. 2009, doi: 10.1109/JPROC.2008.2007473.

6. Joyner, J.; Meindl, J. Opportunities for Reduced Power Dissipation Using Three-Dimensional Integration. *IEEE 2002 International Interconnect Technology Conference (Cat. No.02EX519)*, 2002, pp. 148-150, doi: 10.1109/IITC.2002.1014915.

7. Zhang, R.; Roy, K.; Koh, C.; Janes, D. Stochastic Interconnect Modeling, Power Trends, and Performance Characterization of 3-D Circuits. *IEEE Transactions on Electron Devices*, vol. 48, no. 4, pp. 638-652, April 2001, doi: 10.1109/16.915671.

8. Kumar, V.; Naeemi, A. An Overview of 3D Integrated Circuits, *2017 IEEE MTT-S International Conference on Numerical Electromagnetic and Multiphysics Modeling and Optimization for RF. Microwave, and Terahertz Applications (NEMO)*, 2017, pp. 311-313, doi: 10.1109/NEMO.2017.7964270.

9. Jani, I.; Lattard, D.; Vivet, P.; Arnaud, L.; Beigné, E. Misalignment Analysis and Electrical Performance of High Density 3D-IC Interconnects. *2019 International 3D Systems Integration Conference (3DIC)*, 2019, pp. 1-4, doi: 10.1109/3DIC48104.2019.9058864.

10. Chen, H.; Wu, Y.; Huang, H.; Tsai, C.; Lee, S.; Lee, C.; Wei, T.; Yao, H.; Wang, Y.; Liao, C.; Chang, H.; Lu, C.; Shue, W.; Cao, M. Fully Self-Aligned Via Integration for Interconnect Scaling Beyond 3nm Node. *2021 IEEE International Electron Devices Meeting (IEDM)*, 2021, pp. 22.1.1-22.1.4, doi: 10.1109/IEDM19574.2021.9720600.

11. Brain, R.; Agrawal, S.; Becher, D.; Bigwood, R.; Buehler, M.; Chikarmane, V.; Childs, M.; Choi, J.; Daviess, S.; Ganpule, C.; He, J.; Hentges, P.; Jin, I.; Klopcic, S.; Malyavantham, G.; McFadden, B.; Neulinger, J.; Neirynck, J.; Neirynck, Y.; Pelto, C.; Plekhanov, P.; Shusterman, Y.; Van, T.; Weiss, M.; Williams, S.; Xia, F.; Yashar, P.; Yeoh, A. Low-K Interconnect Stack with A Novel Self-Aligned Via Patterning Process for 32nm High Volume Manufacturing. *2009 IEEE International Interconnect Technology Conference*, 2009, pp. 249-251, doi: 10.1109/IITC.2009.5090400.

12. Murdoch, G.; Bommels, J.; Wilson, C.; Gavan, K.; Le, Q.; Tokei, Z.; Clark, W. Feasibility Study of Fully Self Aligned Vias for 5nm Node BEOL. *2017 IEEE International Interconnect Technology Conference (IITC)*, 2017, pp. 1-4, doi: 10.1109/IITC-AMC.2017.7968958.

13. Briggs, B.; Peethala, C.; Rath, D.; Lee, J.; Nguyen, S.; LiCausi, N.; McLaughlin, P.; You, H.; Sil, D.; Lanzillo, N.; Huang, H.; Patlolla, R.; Haigh,T.; Xu, Y.; Park, C.; Kerber, P.; Shobha, H.; Kim, Y.; Demarest, J.; Li, J.; Lian, G.; Ali, M.; Le, C.; Ryan, E.; Clevenger,

L.; Canaperi, D.; Standaert, T.; Bonilla, G.; Huang, E. Fully Aligned Via Integration for Extendibility of Interconnects to Beyond The 7 nm Node. *2017 IEEE International Electron Devices Meeting (IEDM)*, 2017, pp. 14.2.1-14.2.4, doi: 10.1109/IEDM.2017.8268388.

14. Yang, M.; Aarnink, A.; Schmitz, J.; Kovalgin, A. Y. (2018). Inherently Area-Selective Hot-Wire Assisted Atomic Layer Deposition of Tungsten Films. Thin Solid Films, 649, 17–23. https://doi.org/10.1016/j.tsf.2018.01.016.

15. Choi, J. Y.; Ahles, C. F.; Wong, K. T.; Nemani, S.; Yieh, E.; Kummel, A. C. (2020). Highly Selective Atomic Layer Deposition of MoSiOx Using Inherently Substrate-Dependent Processes. Applied Surface Science, 512. https://doi.org/10.1016/j.apsusc.2019.144307.

16. Lemaire, P. C.; King, M.; Parsons, G. N. (2017). Understanding Inherent Substrate Selectivity During Atomic Layer Deposition: Effect of Surface Preparation, Hydroxyl Density, and Metal Oxide Composition on Nucleation Mechanisms During Tungsten ALD. Journal of Chemical Physics, 146(5). https://doi.org/10.1063/1.4967811.

17. Hashemi, S. M.; Prasittichai, C.; Bent, S. (2014). A New Resist for Area Selective Atomic and Molecular Layer Deposition on Metal–Dielectric Patterns. The Journal of Physical Chemistry C, 118(20), 10957–10962. https://doi.org/10.1021/jp502669f.

18. Pasquali, M.; Gendt, S. D.; Armini, S. (2019). Area-Selective Deposition by A Combination of Organic Film Passivation and Atomic Layer Deposition. ECS Transactions, 92(3), 25–32. https://doi.org/10.1149/09203.0025ecst.

19. Liu, T. L.; Nardi, K. L.; Draeger, N.; Hausmann, D. M.; Bent, S. (2020). Effect of Multilayer Versus Monolayer Dodecanethiol on Selectivity and Pattern Integrity in Area-Selective Atomic Layer Deposition. ACS Applied Materials and Interfaces, 12(37), 42226–42235. https://doi.org/10.1021/acsami.0c08873.

20. Liu, G.; Kanjolia, R.; Potyen, M.; Woodruff, J.; Zope, B.; Chandra, H.; Lei, X. (2022). Selective Deposition of Dielectric on Dielectric Using Low Temperature ALD SiO2 from A Halogen-Free Precursor. ASD2022, 11.

21. Shamiryan, D.; Abell, T.; Iacopi, F.; Maex, K. (2004). Low-K Dielectric Materials.

22. Lee, W.; Fukazawa, A.; Choa, Y. H. (2016). Gap-Fill Characteristics and Film Properties of DMDMOS Fabricated by An F-CVD System. Korean Journal of Materials Research, 26(9), 455–459. https://doi.org/10.3740/MRSK.2016.26.9.455.

23. Shearera, A.; Bent, S. (2022). Area-Selective Atomic Layer Deposition Using Nitrogenous Aromatic Small Molecule Inhibitors. ASD2022.

24. Merkx, M. J. M.; Vlaanderen, S.; Faraz, T.; Verheijen, M. A.; Kessels, W. M. M.; MacKus, A. J. M. (2020). Area-Selective Atomic Layer Deposition of TiN Using Aromatic Inhibitor

Molecules for Metal/Dielectric Selectivity. Chemistry of Materials, 32(18), 7788–7795. https://doi.org/10.1021/acs.chemmater.0c02370.

25. Oszinda, T.; Schaller, M.; Schulz, S. E. (2010). Chemical Repair of Plasma Damaged Porous Ultra Low-K SiOCH Film Using A Vapor Phase Process. Journal of The Electrochemical Society, 157(12), H1140. https://doi.org/10.1149/1.3503596.

26. Choi, J. Y.; Ahles, C. F.; Cho, Y.; Anurag, A.; Wong, K. T.; Nemani, S. D.; Yieh, E.; Kummel, A. (2020). Selective Pulsed Chemical Vapor Deposition of Water-Free HfOx on Si in Preference to SiCOH and Passivated SiO2. Applied Surface Science, 512. https://doi.org/10.1016/j.apsusc.2020.145733.

27. Cho, Y.; Huang, J.; Zhang, Z.; Wang, K.; Lee, P.; Kim, C.; Wong, K., Nemani, S.; Yieh, E.; Kummel, A. C. (2023). Inherent Selective Pulsed Chemical Vapor Deposition of Aluminum Oxide in nm Scale. Applied Surface Science, 622, 156824. https://doi.org/10.1016/j.apsusc.2023.156824.

28. Cho, Y.; Ahles, C. F.; Choi, J. Y.; Huang, J.; Jan, A.; Wong, K.; Nemani, S.; Yieh, E.; Kummel, A. C. (2022). Inherently Selective Water-Free Deposition of Titanium Dioxide on the Nanoscale: Implications for Nanoscale Patterning. ACS Applied Nano Materials, 5(1), 476–485. https://doi.org/10.1021/acsanm.1c03311.

29. Cottrell, T. L. The Strengths of Chemical Bonds, 2d ed., Butterworth, London, 1958; Darwent, B. deB. National Standard Reference Data Series, NationalBureau of Standards, no. 31, Washington, 1970; Benson, S. W. J. Chem. Educ. 42:502 (1965); and Kerr, J. A. Chem. Rev. 66:465 (1966).

30. Yu, P.; Merkx, M.J.M.; Tezsevin, I.; Hausmann, D.M.; Sandoval, T.; Kessels, W.M.M.; Mackusa, A.J.M. (2022). Area-Selective ALD Using Small Molecule Inhibitors of Different Sizes: Steric Shielding Versus Chemical Passivation. ASD2022, 28.

31. Merkx, M.J.M.; Tezsevin, I.; Heinemans, R.H.G.M.; Lengers, R.J.; Kessels, W.M.M.; Sandoval, T.E.; Mackusa, A.J.M. (2022). Mechanisms of Precursor Blocking by Aniline Inhibitor Molecules During Area-Selective ALD of TaN. ASD2022, 15.

32. Andruniow, T.; Zgierski, M. Z.; Kozlowski, P. M. (2001). Theoretical Determination of the Co-C Bond Energy Dissociation in Cobalamins. Journal of the American Chemical Society (Vol. 123, Issue 11, pp. 2679–2680). https://doi.org/10.1021/ja0041728.

33. Moulder, C. A.; Cundari, T. R. (2017). A DFT Survey of the Effects of d-Electron Count and Metal Identity on the Activation and Functionalization of C−H Bonds for Mid to Late Transition Metals. Israel Journal of Chemistry, 57(10). https://doi.org/10.1002/ijch.201700066.

34. Moulder, C. A.; Kafle, K.; Cundari, T. R. (2019). Tungsten-Ligand Bond Strengths for 2p Elements Including σ- And π-Bond Strength Components, A Density Functional Theory

and ab Initio Study. Journal of Physical Chemistry A, 123(37), 7940–7949. https://doi.org/10.1021/acs.jpca.9b03272.

35. Huang, J.; Cho, Y.; Zhang, Z.; Jan, A.; Wong, K. T.; Nemani, S. D.; Yieh, E.; Kummel, A. C. (2022). Selective Pulsed Chemical Vapor Deposition of Water-Free TiO2/Al2O3 and HfO2/Al2O3 Nanolaminates on Si and SiO2 in Preference to SiCOH. ACS Applied Materials and Interfaces, 14(13), 15716–15727. https://doi.org/10.1021/acsami.1c19810.

Chapter 2, in full, is a reprint of the material as it appears in the following publication:

Huang, J., Cho, Y., Wang, V., Zhang, Z., Mu, J., Yadav, A., Wong, K., Nemani, S., Yieh, E., & Andrew, K. (2023). Dielectric-on-Dielectric Achieved on SiO_2 in Preference to W by Water-free Chemical Vapor Depositions with Aniline Passivation. *ACS Applied Materials & Interfaces*, *15*(21), 26128–26137. https://doi.org/10.1021/acsami.3c02278.

The dissertation author was the primary researcher and author of this paper.

Chapter 3 Low-k SiO_x/AlO_x Nanolaminate Dielectric on Dielectric Achieved by Hybrid Pulsed Chemical Vapor Deposition

3.1 Introduction

The semiconductor industry continues scaling of the three-dimensional integrated circuits (IC). IC scaling is achieved by shrinking the sizes of devices and interconnects. Shorter interconnect length improves performance and reduces power consumption. However, continued scaling of ICs in nanometer dimension results in interconnect misalignment. Interconnect misalignment leads to shorting and capacitive coupling between vias[1]. Chen et al. demonstrated that misalignment can be solved by dielectric on dielectric (DOD) deposition which selectively deposits a buffer layer of dielectric on the existing dielectric in preference to metal (schematic diagram shown in Fig. 3.1) [1]. The selective dielectric layer increases the distance (x' compared to x) between the misaligned via and the metal line distance which improves shorting, capacitive coupling, and time-dependent dielectric breakdown (TDDB).

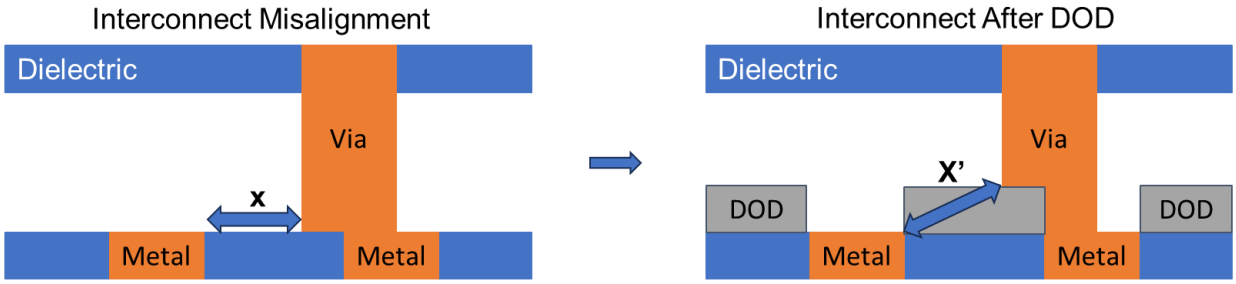

Figure 3.1. Schematic diagram of dielectric on dielectric (DOD) shows how it increases the distance between vias and metal lines by creating a metal recess. By utilizing DOD, interconnect misalignment effect can be effectively reduced, resulting in a larger via to metal line distance.

Selective DOD can be achieved by either atomic layer deposition (ALD) or chemical vapor deposition (CVD) with the help of small molecule inhibitors (SMI) as the metal passivant. Previously, Hashmi et al. and others used alkyl phosphonic acid (octadecyl phosphonic acid) or

thiolate as the metal passivant to achieve ZnO and Al_2O_3 DOD [2-4]; however, no selectivity studies were conducted on nanoscale patterned samples with the octadecyl phosphonic acid passivation [2]. Thiolate passivation only showed good selectivity on the blanket samples while poor selectivity and poor uniformity were observed on nanoscale patterned samples [4]. Both phosphonic acid and thiolate passivation require low temperature atomic layer deposition which typically requires water as co-reactant. The performance of back-end-of-line (BEOL) circuits could be compromised by these water-based ALD, as a small quantity of water may introduce a substantial rise in the dielectric constant of porous low-k materials.

Short chain small molecules inhibitors have been successfully used at high temperatures. A. Shearer et al. demonstrated a 3 nm selectivity of Al_2O_3 deposition on SiO_2 in preference to Cu using small molecule inhibitors such as pyrrole, aniline, and pyridine [5]. M.J.M. Merkx et al. showed a 6 nm selectivity TaN deposition on oxide (Al_2O_3/ SiO_2) in preference to metal (Ru/Co) with aniline passivation at 250 °C with a plasma enhance ALD process [6]. However, this plasma TaN process is not suitable for BEOL DOD since photons, radicals, and ions from the plasma may damage the commonly used low-k material SiCOH [7].

There are previous reports of 5 nm selective deposition of AlO_2, TiO_2, and HfO_2 on SiO_2 in preference to W with 300 °C aniline passivation[8]. These AlO_2, TiO_2, and HfO_2 DOD depositions were achieved by water-free pulsed CVD using tris(2-butoxy)aluminum (ATSB), hafnium tert-butoxide, and titanium isopropoxide, respectively [9-11]. In the present study, a "water-free process" denotes the absence of water as a co-reactant; however, a minute quantity of water might be formed by dehydration reactions of the alkoxy precursor ligands. Of these pulsed CVD selectively deposited DOD dielectric materials, Al_2O_3 (k=7~8) had the lowest k-value. Since lower dielectric

constants can have reduced capacitive coupling, the exploration of a water-free low-k DOD process is imperative.

With a dielectric constant of 3.9, SiO_2 has an acceptable low-k value widely used in the semiconductor industry. There are three main types of processes used for SiO_2 deposition. Two of them require either extremely high CVD substrate temperature (>700 °C) or use water/plasma as the co-reactant which are not compatible with the desired BEOL DOD application [12-15]. The catalytic-based ALD is the only SiO_2 process that does not involve the use of high temperature, water, or plasma. Numerous studies have been conducted on the catalytic-based SiO_2/Al_2O_3 nanolaminate with a k value close to 4.1, utilizing either TBS (tris(tert-butoxy) silanol) or TPS (tris(tert-pentoxy)silanol) together in combination with trimethylaluminum (catalyst TMA) [16-18]. With an initial TMA pulse, TBS/TPS tends to decompose and form sequential SiO_2 nanolaminate layers. However, TMA tends to bond with oxygen and hydroxyl sites on the surface. Consequently, it proves challenging to passivate against TMA substrate reactions with a small molecule inhibitor because TMA can readily displace SMI and form bonds with surface oxide (shown in support info Fig. 3.11) [5]. To date, there has been no reported selectivity study for the catalytic-based SiO_2/Al_2O_3 ALD process.

In a previous study, pulsed CVD AlO_x DOD was successfully deposited on SiO_2 and not on W surface [8]. By utilizing aniline passivation, ATSB alone proved capable of depositing up to 4 nm of selective DOD on SiO_2 surface at 330 °C [8]. This present report documents the benefits of merging the area-selective ATSB process with the low-k catalytic-based SiO_2/Al_2O_3 nanolaminate process. Through this combination, selective low-k dielectric on dielectric can be achieved by using the novel hybrid two-temperature pulsed CVD leveraging the advantages of both techniques.

3.2 Result and Discussion

Aniline passivation and TBS reactivity on different surfaces

In previous studies on water-free selective oxide deposition, water-free pulsed CVD has been shown to exhibit faster growth on metal surfaces compared to SiO_2 [8]. This phenomenon is particularly evident on W metal surfaces, which tend to undergo oxidation. Due to this facile oxidation, W has a propensity to favor the formation of hydroxyl groups and oxide layers [8]. To inhibit oxide growth on metals and allow growth on dielectric, aniline passivation is required. The passivation ability of aniline was tested on HF-cleaned SiO_2, degreased Si_3N_4, and degreased W substrates with the pulsed AlO_x (ATSB) CVD.

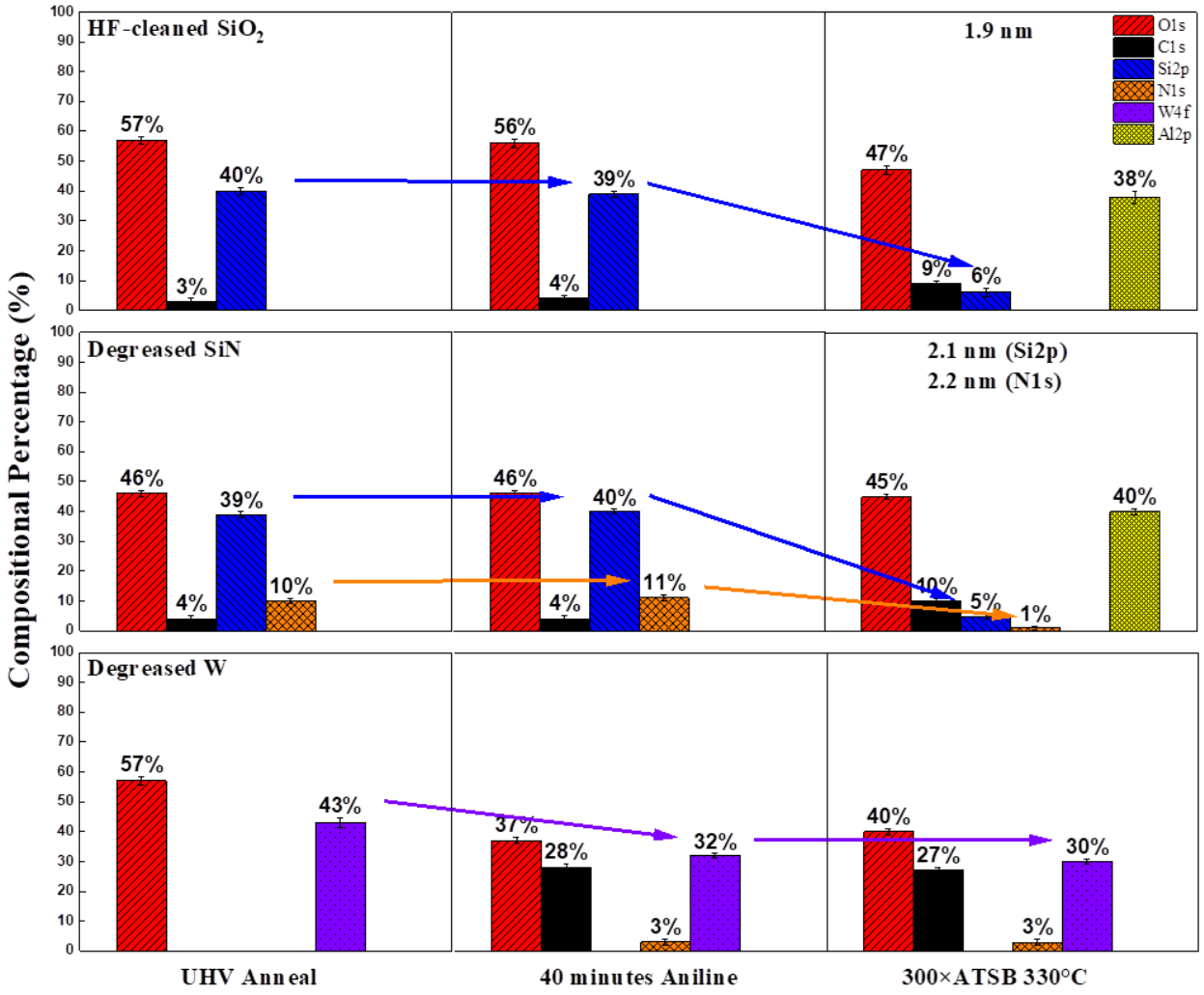

Figure 3.2. AlO_x growth on aniline passivated SiO_2, Si_3N_4, and W. 500 ms pulse time with 10 s purge time of pulsed ATSB CVD at 330 °C. Raw data can be found in support information Fig. 3.12.

In Fig. 3.2, the XPS chemical composition of HF-cleaned SiO_2, degreased Si_3N_4 and degreased W is shown at different stages of the process. This includes a 300 °C rapid UHV anneal, following a 40-minute aniline passivation at 300 °C, and after pulsed CVD of AlO_x using ATSB as the single precursor. After aniline passivation, C_{1s} signal from W increased from 0% to 28%, while the W_{4f} signal decreased from 42% to 32%. Both Si_{2p} and C_{1s} signals from Si_3N_4 and SiO_2 remain unchanged. This indicates a selective aniline passivation performed on the W in preference to SiO_2 and Si_3N_4.

As shown in Fig. 3.2, after a total of 300 pulses of ATSB, around 1.9 nm and 2.2 nm of sub-oxide AlO_x was selectively deposited on SiO_2 and Si_3N_4, respectively; conversely, no deposition was observed on aniline passivated W. ATSB shows a similar, if not faster, growth rate on Si_3N_4 than SiO_2. Deposition thickness was derived from the equation between the inelastic mean free path and the Si_{2p} signal attenuation length of an electron from the substrate.

When examining the Si_3N_4 substrate, the thickness derived from the N_{1s} signal was found to be similar to the thickness derived from the Si_{2p}. The similarity in values derived from the N_{1s} and Si_{2p} signals suggests that both signals can be reliably used to estimate the thickness of the AlO_x layer on Si_3N_4. In the SiO_x/AlO_x nanolaminates (below), it is anticipated that the Si_{2p} signal from the nanolaminate will overlap with the signal from the SiO_2 substrate. Therefore, the focus of the subsequent session will primarily be on the selectivity of SiO_x/AlO_x nanolaminates on Si_3N_4 vs.

W since the N_{1s} signal can be used to quantify the deposition of SiO_x/AlO_x on this insulator.

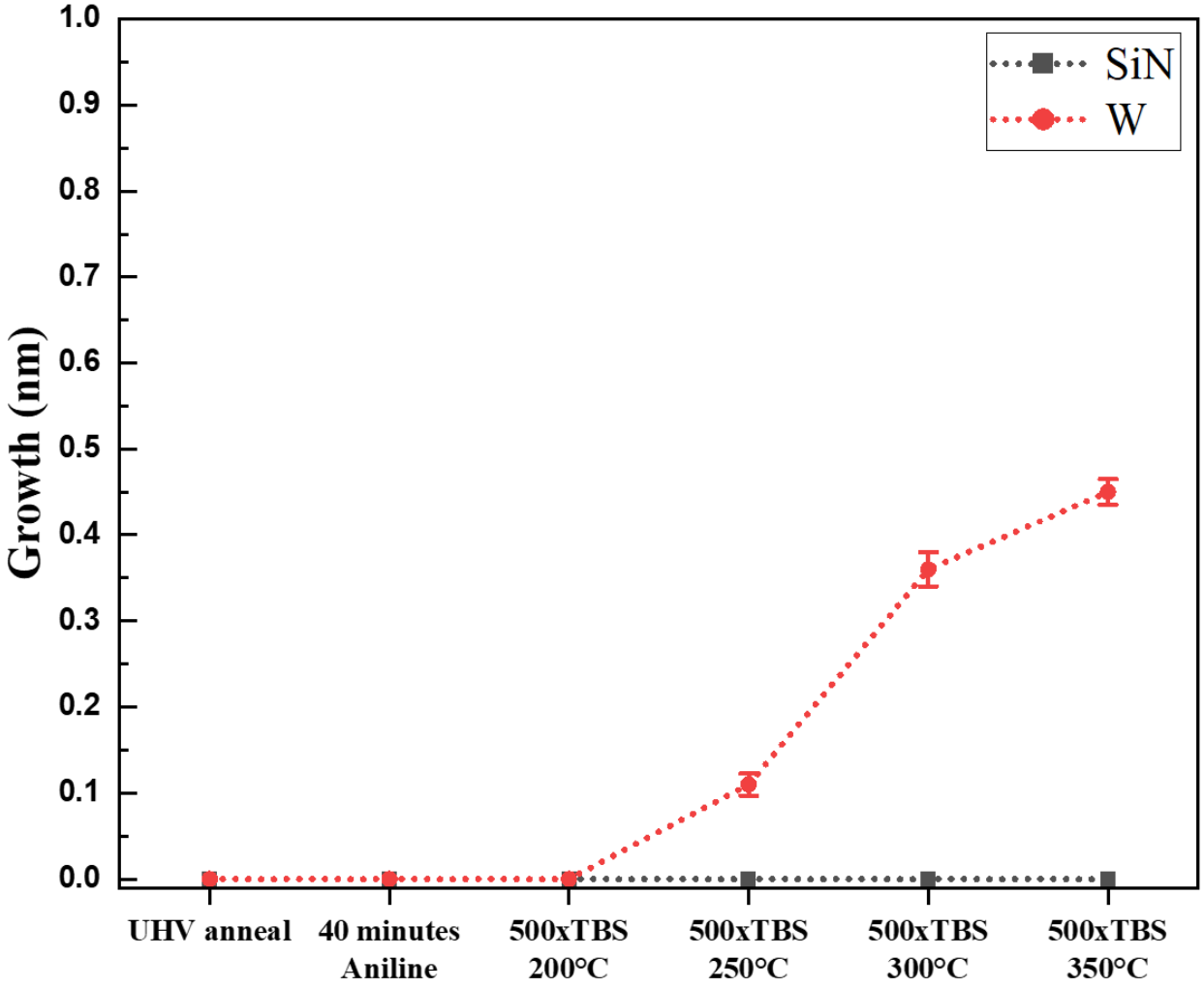

Figure 3.3. TBS reactivity test on Si_3N_4 vs. aniline passivated W at various substrate temperature. 500 ms pulse time with 10 s purge time of pulsed TBS CVD. XPS plot and raw data can be found in support information Fig. 3.13.

To achieve selective deposition of SiO_x/AlO_x nanolaminates, TBS reactivity on Si_3N_4 and W was studied after the aniline passivation. According to Fig. 3.3, TBS at 250 ^oC exhibits a preference for depositing SiO_2 on the W surface rather than the Si_3N_4. The observed results indicate two important findings. First, aniline is not effective in passivating TBS reactions, as TBS still exhibits reactivity towards aniline passivated W with active silanol end group. Second, the presence of W/WO_x suggests that it may act as a Lewis acid site, facilitating the catalysis of the

SiO_2 reaction, which promotes SiO_2 deposition on W surface without the presence of TMA or ATSB at higher temperature (≥250 °C) [19].

The investigation of TBS reactivity was extended to different substrate temperatures (250 ^oC - 350 ^oC), revealing that a higher SiO_2 deposition rate was observed at elevated temperatures during the CVD process. This can be attributed to the decomposition of TBS and subsequent SiO_2 formation on the W surface at higher temperature. No reaction or SiO_2 deposition was observed on the aniline passivated W surface in the absence of Al at 200 °C. A single 60-second TBS exposure was studied on a Si_3N_4 and an aniline passivated W surface, XPS result proved that TBS became unreactive in the absence of Al at 200 °C on the aniline passivated W (XPS shown in Fig. 3.14).

In sum, the substrate temperature during TBS dosing should be set equal to or below 200 °C to ensure the SiO_2 deposition is prevented on the W surface, allowing for the desired area selective SiO_x/AlO_x nanolaminates. At 200 °C TBS does not react with W; therefore TBS selective reaction can be enabled through the catalytic reaction of TBS with the selectively deposited AlO_x on SiO_2/ Si_3N_4.

SiO_x/AlO_x nanolaminates selectivity optimization

Since the selectivity of AlO_x deposition using ATSB was optimized at 330 °C and TBS showed no deposition by itself at 200 °C, deposition with 50 pulses of ATSB at 330 °C followed by a 30-minuite purge and 50 pulses of TBS at 200 °C was performed on degreased Si_3N_4 and W (shown in Fig. 3.4).

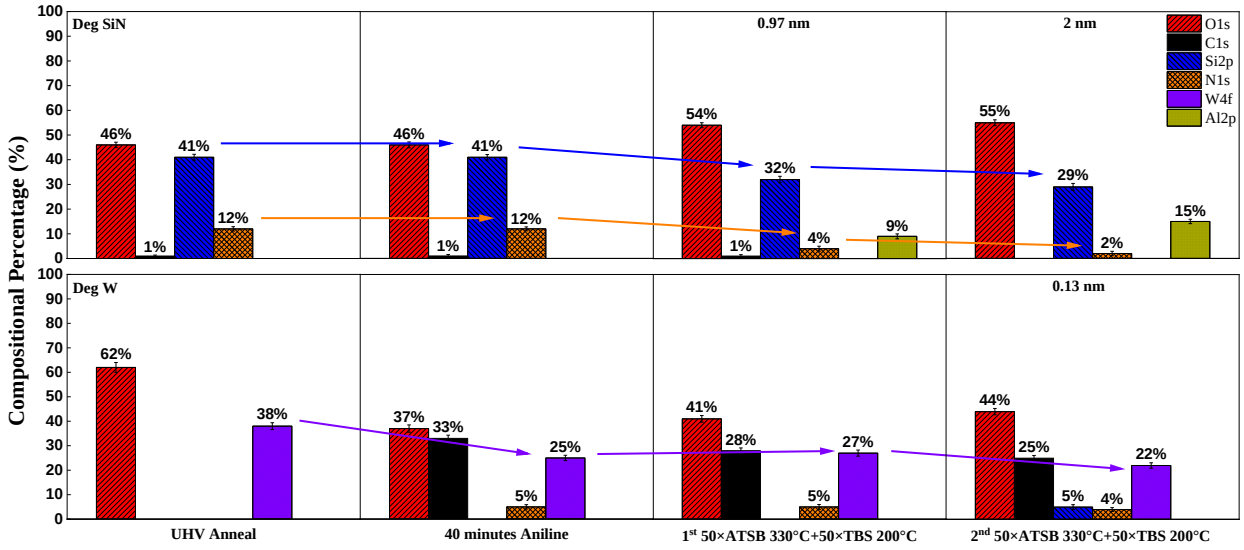

Figure 3.4. Pulsed ATSB at 330 °C followed by pulsed TBS at 200 °C on Si_3N_4 vs. aniline passivated W. The process utilized 50 pulses of ATSB at 330 °C and 50 pulses TBS dosing at 200 °C. Both ATSB and TBS has a pulse time of 500 ms and 10 s purge time. Scatter plot and raw data can be found in support information Fig. 3.15.

As shown in Fig 3, after the aniline passivation, C_{1s} peak from W increased from 0% to 33%, O_{1s} decreased from 62% down to 37% and no compositional signal changed on Si_3N_4. After the initial supercycle with the binary substrate temperature, around 0.97 nm was selectively deposited on Si_3N_4 while no deposition on W. The observed decrease in C_{1s} signal from 33% 28% and the increase in O_{1s} signal from 37% to 41% on W suggested that the initial catalytic reaction of the SiO_x/AlO_x nanolaminate compromised the aniline passivation layer by introducing hydroxyl groups. The hydroxyl groups were probably originated from trace TBS silanol groups and released as a byproduct during the catalytic reaction. With an additional supercycle, around 2 nm of SiO_x/AlO_x was deposited on Si_3N_4 while only 0.13 nm on W.

The deposition of 50 pulses of TBS requires approximately 9 minutes to complete. This extended dosing time increases the likelihood of compromising the aniline layer by introducing physiosorbed or chemisorbed hydroxyl species. According to previous research, the SiO_2 laminate growth depends on two competing factors: propagation/insertion and cross-linking [18, 20]. Rapid

TBS insertion promotes higher growth rates, while the occurrence of cross-linking inhibits the growth. During the initial few pulses of TBS, the SiO_2 layer can undergo cross-linking, effectively halting further growth. Subsequent pulses primarily compromise the integrity of the aniline layer rather than contribute to the growth process. Additionally, pulsing TBS does not enhance selectivity by purging physiosorbed TBS on the W surface due to its inert behavior in the absence of ATSB at 200 °C. Thus, 50 pulses of ATSB at 330 °C followed by 60-second continuous TBS exposure at 200 °C was performed on degreased Si_3N_4 and W (shown in Fig. 3.5). As before, a 30-minute purge was conducted between two precursors.

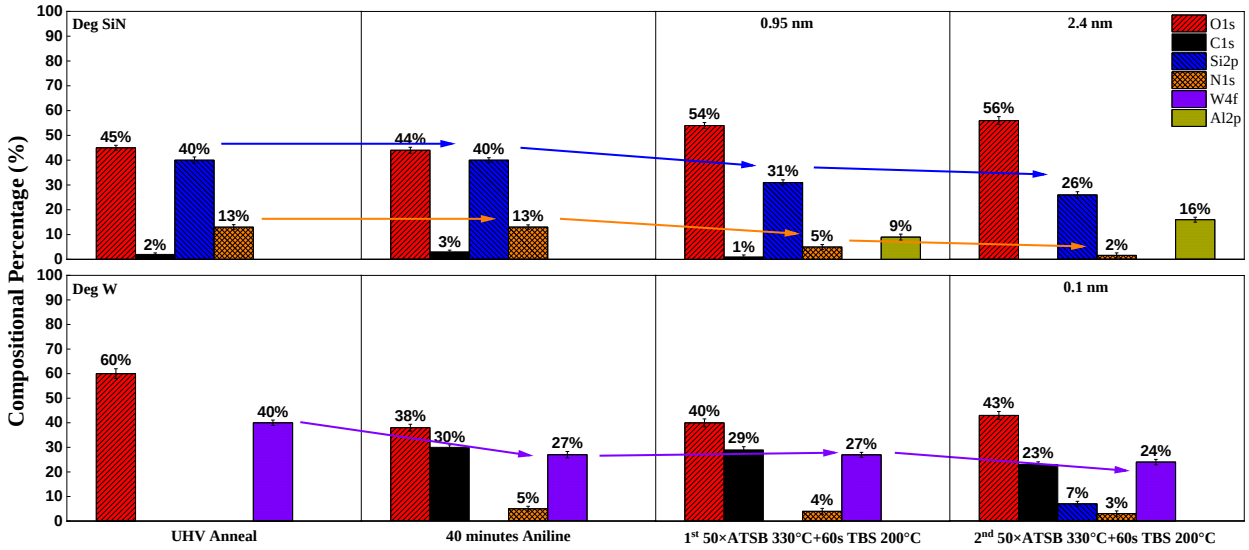

Figure 3.5. Pulsed ATSB at 330 °C followed by continuous TBS exposure at 200 °C on Si_3N_4 vs. aniline passivated W. The process utilized 50 pulses of ATSB at 330 °C and a 60-second continuous TBS at 200 °C. ATSB has a pulse time of 500 ms and 10 s purge time. Scatter plot and raw data can be found in support information Fig. 3.16.

The XPS chemical composition analysis in Fig. 3.5 demonstrated that after the first supercycle, the O_{1s} signal increased to 39% while the C_{1s} signal only decreased to 29%. This indicated that reducing the dosing time resulted in less damage to the aniline layer. After a second supercycle, this recipe achieved a higher selectivity of 2.4 nm of SiO_x/AlO_x deposition on Si_3N_4 in preference to W.

The longer pumping time for pressure recovery and higher residual pressure observed after TBS dosing, in comparison to ATSB, suggested that physiosorbed TBS on the chamber walls might slowly degas even after the dosing process is completed. Therefore, during the purging time between ATSB dosing and TBS dosing, TBS from the chamber walls might continue attacking the aniline passivation layer and result in an early loss of selectivity. The prolonged exposure of TBS during the purging time increased the likelihood of SiO_2 deposition on the W surface, utilizing W/WO_x as the Lewis acid catalytic sites. This explains the presence of a Si_{2p} signal (5%~7%) on W without Al_{2p} after the second supercycle.

A half supercycle consisting of 50 pulses of ATSB CVD at 330 °C followed by an immediate XPS study was conducted. Subsequently, another half supercycle involving a 60-second exposure to TBS at 200 °C was performed for further investigation.

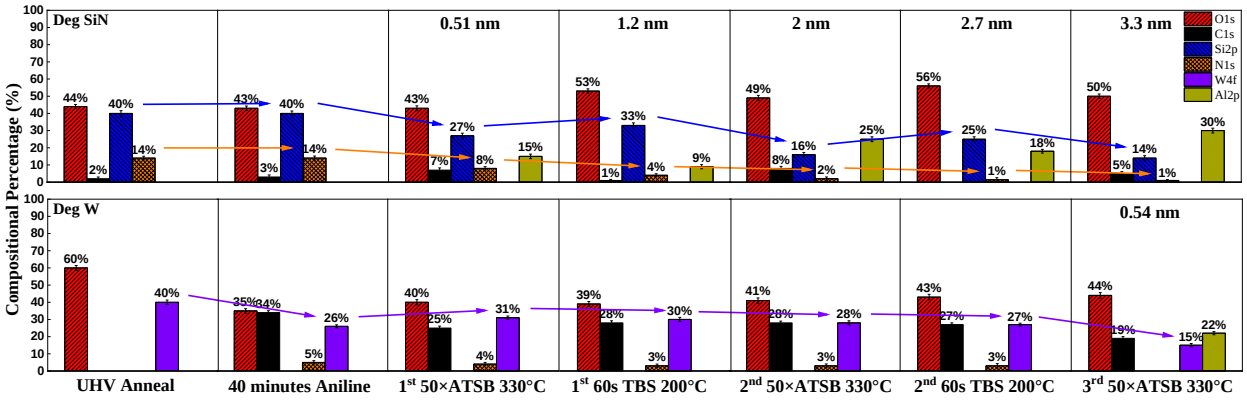

Figure 3.6. Half-supercycle hybrid pulsed ATSB at 330 °C with half-supercycle continuous TBS exposure at 200 °C on Si_3N_4 vs. aniline passivated W. The process utilized 50 pulses of ATSB at 330 °C and a 60-second continuous TBS at 200 °C. ATSB has a pulse time of 500 ms and 10 s purge time. Scatter plot and raw data can be found in support information Fig. 3.17.

As shown by the XPS study in Fig. 3.6, each half cycle process contributed around a monolayer thickness of AlO_x or SiO_x interlayer, resulting in the formation of a nanolaminate structure. Around 2.7 nm of selective SiO_x/AlO_x deposition was deposited only on degreased Si_3N_4. Atomic force microscopy (AFM) measurement showed a smooth deposition with an RMS

roughness of 0.8 nm (shown in Fig. 3.18). By moving the sample back to UHV chamber for XPS after each half supercycle, no Si_{2p} signal was detected after the second round of the TBS dosing. However, during the subsequent 50 pulses of the ATSB half supercycle, selectivity was lost and approximately 0.54 nm of pure AlO_x was deposited on the W. This can be attributed to the high hydroxyl content and the decrease in aniline passivation on the W surface. Introducing TBS resulted in a selectivity loss of approximately 2 nm compared to the pure pulsed ATSB CCVD process described in the previous research [9].

The hybrid half supercycle process with a lower TBS dosing substrate temperature at 150 °C was investigated, along with a similar half supercycle process involving a 120-second TBS dosing at the same temperature. The XPS chemical composition charts for these experiments can be found in the support information Fig. 3.19 and Fig. 3.20. Lowering the TBS dosing temperature allows for a higher number of half supercycles to be dosed. Despite a slightly lower half supercycle TBS growth rate, similar selectivity was achieved compared to the previous conditions. From Fig. 3.20, longer half supercycle TBS dosing (120 seconds) did not significantly impact selectivity. The increase in TBS dosing time did not result in an increase in SiO_2 laminate growth. This suggests that the 60-second half supercycle TBS is saturated and does not compromise aniline passivation.

The effect of ATSB thickness on selectivity was also examined by altering the number of ATSB pulses per half supercycle while keeping the TBS dosing at 60 seconds and the temperature at 200 °C. Support information Fig. 3.21 and Fig. 3.22 depict the study conducted with lower (25 pulses) and higher (100 pulses) number of ATSB pulses, respectively. Both experiments showed a lower selectivity than the process shown in Fig. 3.6. The results indicate that a lower number of ATSB pulses result in lower selectivity due to the formation of thinner AlO_x layers, while TBS

remains the dominant factor contributing to the loss in selectivity. Conversely, with a higher number of ATSB pulses, the deposition of thicker ATSB layers leads to a loss in selectivity.

Tris(tert-pentoxy) silanol (TPS) is a common alternative precursor for SiO_x/AlO_x deposition. The half supercycle process involving 50 pulses ATSB at 330 °C and 60-second TPS at 150 °C was also studied (shown in support information Fig. 3.23). The XPS chemical compositional chart showed a selectivity of 1.6 nm SiO_x/AlO_x achieved on Si_3N_4 in preference to aniline passivated W. During the second-round half supercycle TPS dosing, around 0.3 nm of pure SiO_2 was deposited on the W surface. This early loss in selectivity might be due to the higher reactivity of liquid phase TPS compared to solid phase TBS. Burton et al. demonstrated this increased reactivity by showing that TPS exhibits a substantially higher growth rate than TBS [18]. After thorough optimization efforts, the highest observed selectivity achieved is 2.7 nm using the hybrid half supercycle process involving 50 pulses of ATSB at 330 °C and a 60-second TBS dosing at 200 °C.

SiO_x/AlO_x nanolaminates nanoselectivity and capacitance-voltage measurement

A proposed mechanism of the hybrid half supercycle pulsed CVD process with aniline passivation is shown in Fig. 3.7. Due to the long duration of air exposure, there are Si-OH groups generated on the Si_3N_4 substrate surface. The aniline selectively passivates the W surface through W-C bonds (horizontal configuration) and W-N bonds (vertical configuration) while leaving Si_3N_4/SiO_2 unaffected. The detailed selective bonding of aniline to a metal surface has been previously studied by Tezsevin et al. [21]. The hydrophobic phenyl ring and steric shielding of the aniline layer prevent the initial ATSB precursor from chemisorbing on W, causing it to only weakly physisorb and subsequently desorb at 330°C.

The ATSB precursor decomposes when it physiosorbs on the 330°C Si_3N_4/SiO_2 substrate surface; a 2-butene byproduct desorbs, generating $Al(OH)(O\text{-}sec Bu)_2$, $Al(OH)_2(O\text{-}sec Bu)$, and maybe even some $Al(OH)_3$ species. Based on the low growth rate (~0.01 nm per ATSB cycle), ATSB most likely decomposed into $Al(OH)(O\text{-}sec Bu)_2$ or $Al(OH)_2(O\text{-}sec Bu)$. The presence of carbon associated with the O-*sec*-butyl ligands was confirmed through the previous XPS studies shown in Fig. 3.6. $Al(OH)(O\text{-}sec Bu)_2$, $Al(OH)_2(O\text{-}sec Bu)$, and $Al(OH)_3$ can chemisorb on the Si_3N_4/SiO_2 surfaces by reacting with a surface isolated hydroxyl site or two adjacent hydroxyl sites. Given that the pKa of surface Si-OH groups are 4.5, pKa of $Al(OH)_3$ is 11.2, and the pKa of CH_3CH_2OH ligand (similar to sec-butanol groups) is 15.9, protonation of Al-OH and Al-OR (Al-O-*sec*Bu) groups by the more acidic Si-OH groups is favorable during the chemisorption process [22-24]. The possible chemical reaction of the Si-OH groups with the Al-OH and Al-OR groups are shown below as equations 1 and 2. Additional hydroxyl groups from $Al(OH)_2(O\text{-}sec Bu)$, and $Al(OH)_3$ species allow continuous growth for subsequent pulses.

$$\text{Si-OH(surface)} + \text{Al-OH} \rightarrow \text{Si-O-Al} + H_2O\uparrow \quad (1)$$

$$\text{Si-OH(surface)} + \text{Al-OR} \rightarrow \text{Si-O-Al} + \text{ROH}\uparrow \quad (2)$$

For the second half supercycle, the 60-second TBS dosing only reacts with the deposited AlO_x initial layer. With a pKa of 10 for H_3SiO_3 and 11.2 for $Al(OH)_3$, the protonation reaction illustrated in equation 3 below is favorable [25].

$$\text{Al-OH(surface)} + (RO)_3\text{Si-OH} \rightarrow \text{Al-O-Si}(OR)_3 + H_2O\uparrow \quad (3)$$

This equation 3 demonstrates that TBS (TPS) might undergo protonation with Al-OH group to form Al-O-Si(O^tBu)$_3$. Moreover, TBS might also undergo protonation with Al-O-*sec*Bu groups, resulting in the formation of Al-O-Si(O^tBu)$_3$ with the release of HO-*sec*Bu ligands.

A dditional TBS molecules will be subjected to Al-O-Si(O^tBu)$_2$-O-Si(O^tBu)$_3$ polymerization and release HO^tBu as the byproduct. A general chemical equation for this step is depicted below as equation 4.

$$\text{Si-OR(surface)}+(RO)_3\text{Si-OH}\rightarrow\text{Si-O-Si}(OR)_3+ROH\uparrow \quad (4)$$

Remaining Si-O^tBu groups undergo 2-methyl-propene group loss and lead to the formation of Si-OH bonds [26]. These Si-OH can then cross-link to form Si-O-Si bonds and emit water (shown in equation 5 and 6, where R'= alkene derived from starting R group in equation 5).

$$\text{Si-OR}\rightarrow\text{Si-OH}+R'\uparrow \quad (5)$$

$$\text{Si-OH}+\text{Si-OH}\rightarrow\text{Si-O-Si}+H_2O\uparrow \quad (6)$$

Once Si-O-Si crosslinking bonds reach approximately a monolayer thickness (~0.5 nm), TBS (TPS) can no longer come into proximity to the AlO_x layer and become harder to be protonated. This hindered proximity ultimately results in the termination of the reaction. Additionally, the presence of an excess number of O-*sec*-butyl groups branching out from the Al center results in a significant incorporation of carbon into the deposition film and the film exhibits high porosity. The combination of a high carbon content and a high level of porosity leads to the formation of a low-k dielectric film.

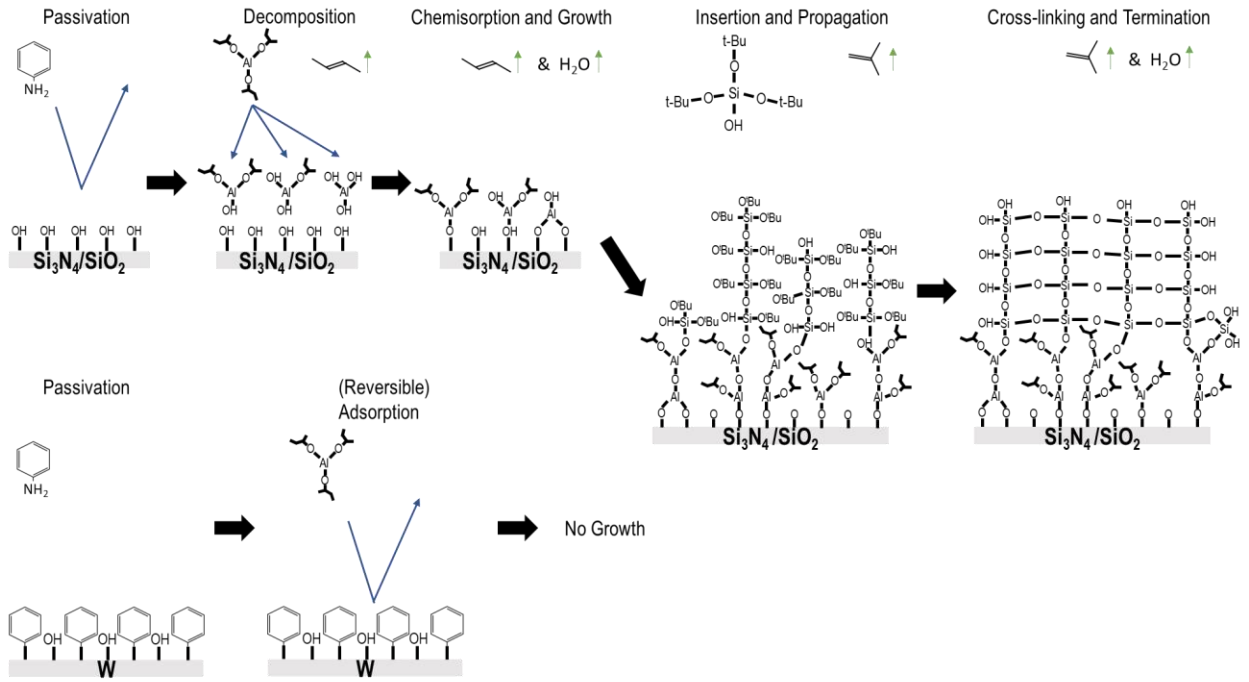

Figure 3.7. Proposed mechanism of hybrid half supercycle pulsed CVD process on Si_3N_4/SiO_2 in preferent to W with aniline passivation.

The optimized hybrid half supercycle process, utilizing 50 pulses of ATSB at 330 °C and a 60-second TBS dosing at 200 °C, demonstrated the highest observed selectivity of 2.7 nm. The same process was applied on a nanoscale W/SiO_2 patterned sample with a pitch size of 55 nm and a linewidth of 30 nm. By conducting the optimized hybrid pulsed CVD SiO_x/AlO_x process on the patterned sample, selectivity was quantified at the nanoscale level.

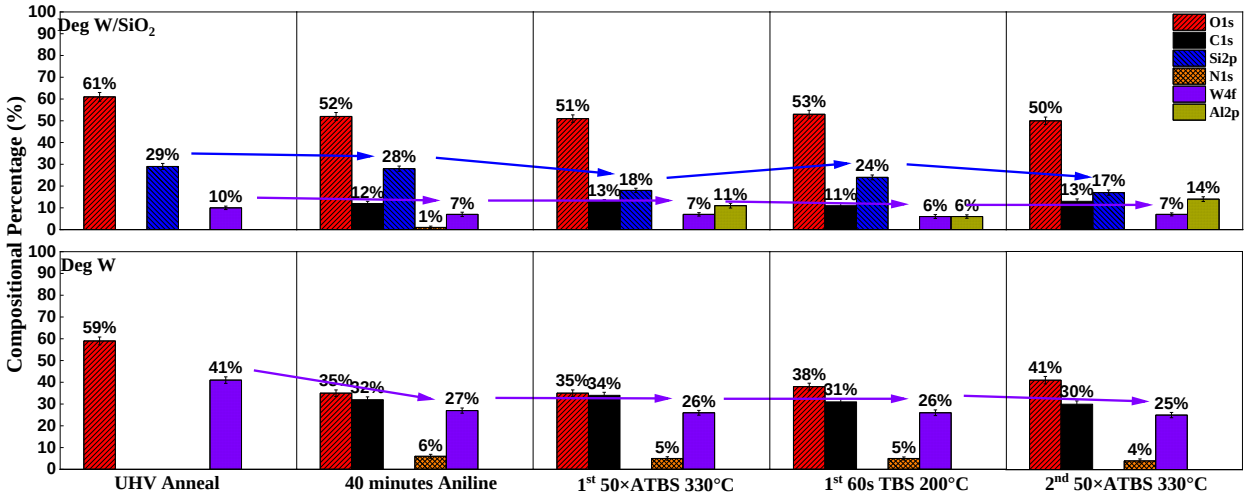

Figure 3.8. Selective hybrid pulsed SiO_x/AlO_x CVD on SiO_2 region of W/SiO_2 patterned sample with aniline passivation. The process utilized 50 pulses of ATSB at 330 °C and a 60-second TBS dosing at 200 °C. Raw data can be found in support information Fig. 3.24.

In Fig. 3.8, XPS analysis was performed during the hybrid pulsed SiO_x/AlO_x CVD on both W/SiO_2 patterned sample and the blanket W sample. Initially, no carbon content was detected on the surface of either sample. After a 40-minute aniline passivation step, the patterned surface exhibited approximately 12% carbon content, while the blanket W showed a monolayer of aniline passivation. The process was stopped after the second round of the ATSB half supercycle to prevent overgrowth on the W region of the patterned sample. Following the initial ATSB half supercycle, the Si_{2p} signal from the patterned sample decreased from 28% to 18%, Al_{2p} signal increased from 0% to 11%. The W_{4f} signal remained unchanged. Subsequently, during the TBS half supercycle, the Si_{2p} signal from the patterned sample increased from 18% to 24%, indicating the deposition of SiO_2, while Al_{2p} signal decreased from 11% to 6%. Lastly, samples were finished with another half supercycle of ATSB.

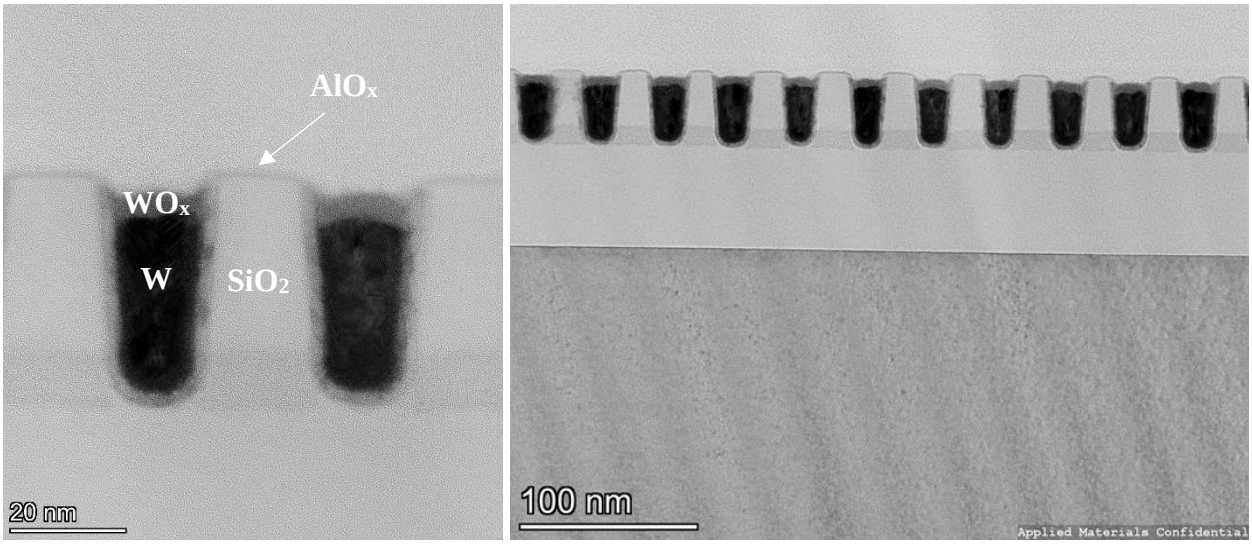

Figure 3.9. TEM images of the selective hybrid pulsed SiO_x/AlO_x CVD on SiO_2 region of W/SiO_2 patterned sample. The process utilized 50 pulses of ATSB at 330 °C and a 60-second TBS dosing at 200 °C. EELS study showed in support information Fig. 3.25

TEM analysis was conducted on the W/SiO_2 patterned sample after the deposition, as depicted in Fig. 3.9. The images showed a SiO_x/AlO_x deposition of approximately 2 nm on the SiO_2 surface, while the W surface remained pristine.

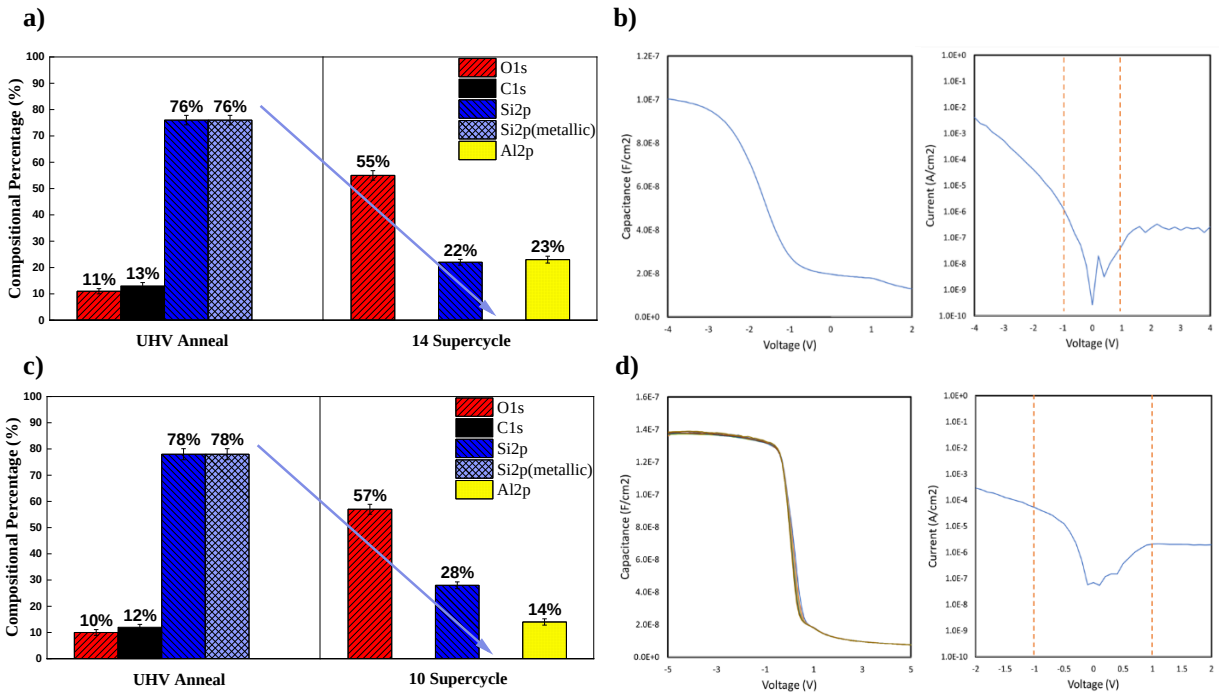

Figure 3.10. a) Selective hybrid pulsed SiO_x/AlO_x CVD on Si for capacitance study. 14 supercycles of 50 pulses of ATSB at 330 °C and a 60-second TBS dosing at 200 °C were employed. Raw data can be found in support information Fig. 3.26. b) CV and IV measurement of the selective hybrid pulsed SiO_x/AlO_x CVD on Si. c) Selective hybrid pulsed SiO_x/AlO_x CVD on Si for capacitance study. 10 supercycles of 25 pulses of ATSB at 330 °C and a 60-second TBS dosing at 200 °C were employed. Raw data can be found in support information Fig. 3.27. d) CV and IV measurement of the selective hybrid pulsed SiO_x/AlO_x CVD on Si with the 25 pulses of ATSB at 330 °C and a 60-second TBS dosing at 200 °C process.

To ensure the deposition of a thick and non-leaky SiO_x/AlO_x film suitable for capacitance-voltage (CV) and current-voltage (IV) study, 14 supercycles of the same deposition recipe (50 pulses of ATSB at 330 °C and a 60-second TBS dosing at 200 °C) were applied to a HF-cleaned Si substrate. From Fig. 3.10 a), the XPS data showed a 1:1 Si:Al ratio after the deposition. The as-deposited SiO_x/AlO_x thickness was measured to be approximately 29.3 nm by ellipsometry. Subsequently, a 30-minute 450 °C O_2 anneal was performed, followed by a stepped forming gas anneal at 330 °C, 350 °C, 380 °C for 15 minutes each. After these annealing steps, the thickness of the SiO_x/AlO_x deposition was reduced to around 28 nm. For electrical contact, the backside of the Si substrate was coated with sputtered gold and a nickel dot electrode with a diameter of 145

μm was deposited. A separate HF-cleaned Si substrate sample was dosed with 10 supercycles following the identical deposition recipe involving 50 pulses of ATSB at 330 °C and a 60-second TBS dosing at 200 °C. This sample underwent identical annealing procedures and Ni dot deposition. Subsequently, cross-sectional TEM analysis was carried out to confirm that the deposition thickness observed matched the ellipsometry thickness measurement. In the TEM image Fig. 3.28, nanolaminate structure was clearly observed.

Fig. 3.10 b) presents the single frequency 1MHz CV and IV measurements conducted on the deposited SiO_x/AlO_x film. Based on the measurements of capacitance, area, and thickness, the dielectric constant (k) value was calculated, yielding a value of 3.3. This low k value achieved by SiO_x/AlO_x nanolaminate could be due to high porosity and carbon incorporation in the deposition film. The catalytic growth of SiO_2 using TBS involves two competing factors: insertion and cross-linking. Fast insertion combined with rapid cross-linking can potentially lead to a disorderly arrangement of molecules and increased porosity in the SiO_2 interlayer. Furthermore, the IV measurement showed that within the voltage range of ±1V, the current was measured to be less or equal to 1×10^{-6} A/cm^2, indicating low leakage current, valid CV measurement and satisfactory electrical properties of the deposited film for BEOL DOD application.

10 supercycles of the 25 pulses of ATSB at 330 °C and a 60-second TBS dosing at 200 °C was also performed on a HF-cleaned Si to study the effect of Si ratio in the SiO_x/AlO_x nanolaminate on the CV performance. From Fig. 3.10 c), 25 pulses of ATSB at 330 °C and a 60-second TBS dosing at 200 °C process rendered a 2:1 Si:Al ratio. The as-deposited SiO_x/AlO_x thickness was measured to be approximately 15.7 nm by ellipsometry. Sample underwent a 30-minute 450 °C O_2 anneal was performed, followed by a stepped forming gas anneal at 330 °C, 350 °C, 380 °C for 15 minutes each. After these annealing steps, the thickness of the deposition became

15.6 nm. The backside of the sample was sputtered with gold and a nickel dot electrode with a diameter of 145 µm was deposited on the deposition surface.

In Fig. 3.10 d), the multi-frequency CV measurement and IV measurement were conducted on the deposited SiO_x/AlO_x film with 25 pulses ATSB process to study the effect of frequency on the CV and calculate its k value. A minor frequency dependent CV shift was observed in the depletion region. This minimal frequency dependent CV shift would not affect the intended use of the film for the DOD application. Based on the measured capacitance, area, and thickness, the k value was calculated to be 2.5. The IV measurement of this thinner SiO_x/AlO_x nanolaminate showed a leakage current less or equal to 1×10^{-4} A/cm^2 within the voltage range of ±1V, indicating low leakage current and valid CV measurement. The rise in leakage current observed in this 2:1 Si:Al ratio sample in comparison to the Si:Al ratio of 1:1 sample in Fig. 3.10b) is primarily attributed to the reduction in thickness. Nonetheless, it should be noted that the nanolaminates tend to absorb water from the atmosphere, leading to an increase in the k value up to 4.3 (2:1 Si:Al ratio shown in Fig. 3.29 in the supporting information) and 5 (1:1 Si:Al ratio shown in Fig. 3.30 in the supporting information). With additional UHV anneal, k value of 2.5 of the 2:1 Si:Al ratio nanolaminate could be restored by extracting the water molecules out (shown in Fig. 3.31). This indicates that further carbon incorporation may be needed to make the film more hydrophobic or a simple encapsulation may be required to inhibit water adsorption.

3.3 Conclusion

A novel approach combining selectivity of the pulsed ATSB CVD process with catalytic reactions using TBS/TPS was employed to achieve a low-k dielectric deposition for DOD applications. Aniline demonstrated selective passivation of the W surface over SiO_2 and Si_3N_4. TBS exhibited no growth in the absence of ATSB below or at 200 °C, preventing deposition in the

absence of AlO_x. However, prolonged exposure to TBS could potentially compromise the aniline passivation layer by introducing hydroxyl groups. Additionally, the data is consistent with TBS utilizes W/WO_x as a Lewis acid site for catalyzing the SiO_2 reaction, leading to an early loss in selectivity compared to the pulsed AlO_x (ATSB) CVD. By incorporating aniline passivation and employing a hybrid half-cycle process involving 50 pulses of ATSB at 330 °C followed by a 60-second TBS exposure, a selective SiO_x/AlO_x nanolaminate with a thickness of approximately 2.7 nm was successfully deposited on Si_3N_4 while preserving a clean W surface. The same process was also applied to a nanoscale W/SiO_2 patterned substrate, resulting in a selective deposition of approximately 2 nm on SiO_2 only, as confirmed by the TEM analysis. CV and IV measurements validated the ability of this process to deposit a low-k dielectric nanolaminate with a dielectric constant (k) value of 3.3 with a 1:1 Si:Al ratio and a k value of 2.5 with a 2:1 Si:Al ratio. The lower k value measured compared to pure SiO_2 can be attributed to the presence of porous SiO_2 interlayers. This is the first report of a further thermal CVD process for deposition of low-k dielectric and the first report for a selective low-k process on the nanoscale.

3.4 Methods

Reactor

A custom-built vacuum chamber system was utilized for all passivation, CVD processes, and deposition characterization (see chamber schematic diagram Fig. 3.32). The system consisted of three main chambers: the load-lock chamber (for sample loading and unloading), the deposition chamber, and the ultra-high vacuum (UHV) chamber. To facilitate a direct selectivity comparison, two or three samples were loaded simultaneously into the load-lock chamber.

The deposition chamber, which maintained a base pressure of $2e10^{-6}$ Torr, served as the primary space for all passivation and CVD experiments. It was equipped with a Pfeiffer TPH060 turbo

pump and an Edwards RV3 rotary backing pump for effective evacuation. Samples were affixed to a copper sample block on a manipulator with a cartridge heater. During the passivation and CVD processes, samples were heated and positioned at the center of the deposition chamber. Within the deposition chamber, there were several dosing lines for precursors. These included a N_2 purge line, an ATSB dosing line, an aniline dosing line, a TBS dosing line, and a TPS dosing line. These dosing lines were connected to the deposition chamber and directed towards the sample stage at a distance of 8 cm. This setup allowed controlled delivery of the respective precursors to the sample during the process.

Deposition Process

Blanket SiO_2, blanket Si_3N_4, blanket W, and W/SiO_2 patterned were used as the substrate materials. The W/SiO_2 patterned sample was obtained from Applied Materials. The W/SiO_2 pattern has a pitch of ~55 nm and an average linewidth of ~30 nm. A barrier layer of TiN was employed between W and SiO_2. Prior to loading, all samples underwent a degreasing process using acetone, methanol, and HPLC water. Each rinse lasted for approximately 10 s. After each 10 s rinse, an N_2 air gun was used to blow off any residual solution on the surface of the samples. This step was performed to ensure complete removal of the rinsing solution. An additional 30 s 0.5% hydrofluoric acid clean followed by an HPLC water 30 s rinse was conducted only on the SiO_2 substrates.

Tris(tert-butoxy)aluminum (ATSB, 97%), tris(tert-butoxy)silanol (TBS, 99.999%), tris(tert-pentoxy)silanol (TPS, ≥99.99%), and aniline (ACS reagent 99.5%) were purchased from Sigma Aldrich (ATSB, TBS, and TPS chemical structures shown in supporting information Fig. 3.33). Each precursor dosing line was operated with no carrier gas and had one pneumatic ALD valve and one shut off valve. A leak valve was installed in the N_2 purge line to regulate the purging

pressure. Heating tapes were employed to maintain a 150 °C uniform temperature for both chamber wall and the dosing lines.

Prior to any CVD processes, aniline passivation was conducted by placing the samples inside the deposition chamber without pumping. The sample and aniline gas were trapped in the chamber at a temperature of 300 °C for a duration of 40 minutes. The passivation process was carried out under a constant trapping pressure of 780 mTorr.

Previously, ATSB pulsed CVD process was optimized at 330 °C substrate temperature for faster growth and improved selectivity [8]. The ATSB precursor bottle was heated to 110 °C. The opening time of ATSB pneumatic valve was set to 500 ms followed by a 10 s purge time between pulses which rendered a pressure spike of 0.02 mTorr. During the CVD process, a continuous flow of N_2 purge gas was employed.

For SiO_x/AlO_x nanolaminate hybrid pulsed CVD, samples were dosed with the optimized ATSB pulses at 330 °C followed by TBS or TPS exposure (1. Pulsed exposure: 500 ms opening time with 10 s purge time between pulses; 2. Continuous exposure). During the experiment, the TBS bottle was kept at 88 °C while TPS bottle was kept at 90 °C. Both TBS and TPS provide a pressure spike up to 1 mTorr. Various substrate temperatures were tested during TBS exposure. Both pulsed and continuous TBS exposure modes were examined in the result and discussion section.

Deposition Characterization

X-ray photoelectron spectroscopy (XPS) was conducted *in-vacuo* to study as-deposited film composition in the UHV chamber. The XPS system has a monochromatic Al Kα X-ray source (E = 1487 eV) and a hemispherical analyzer (XM 1000 MkII/SPHERA, Omicron Nanotechnology) configured with a pass energy of 50 eV. The XPS anode voltage was set to 10 kV, and the filament

emission current was set to 25 mA. All XPS data collected was analyzed by the Casa XPS v2.3 program. *Ex-situ* characterization studies include atomic force microscopy (AFM), ellipsometry, transmitted electron microscopy (TEM) and electron energy loss spectroscopy (EELS).

3.5 Supporting Information

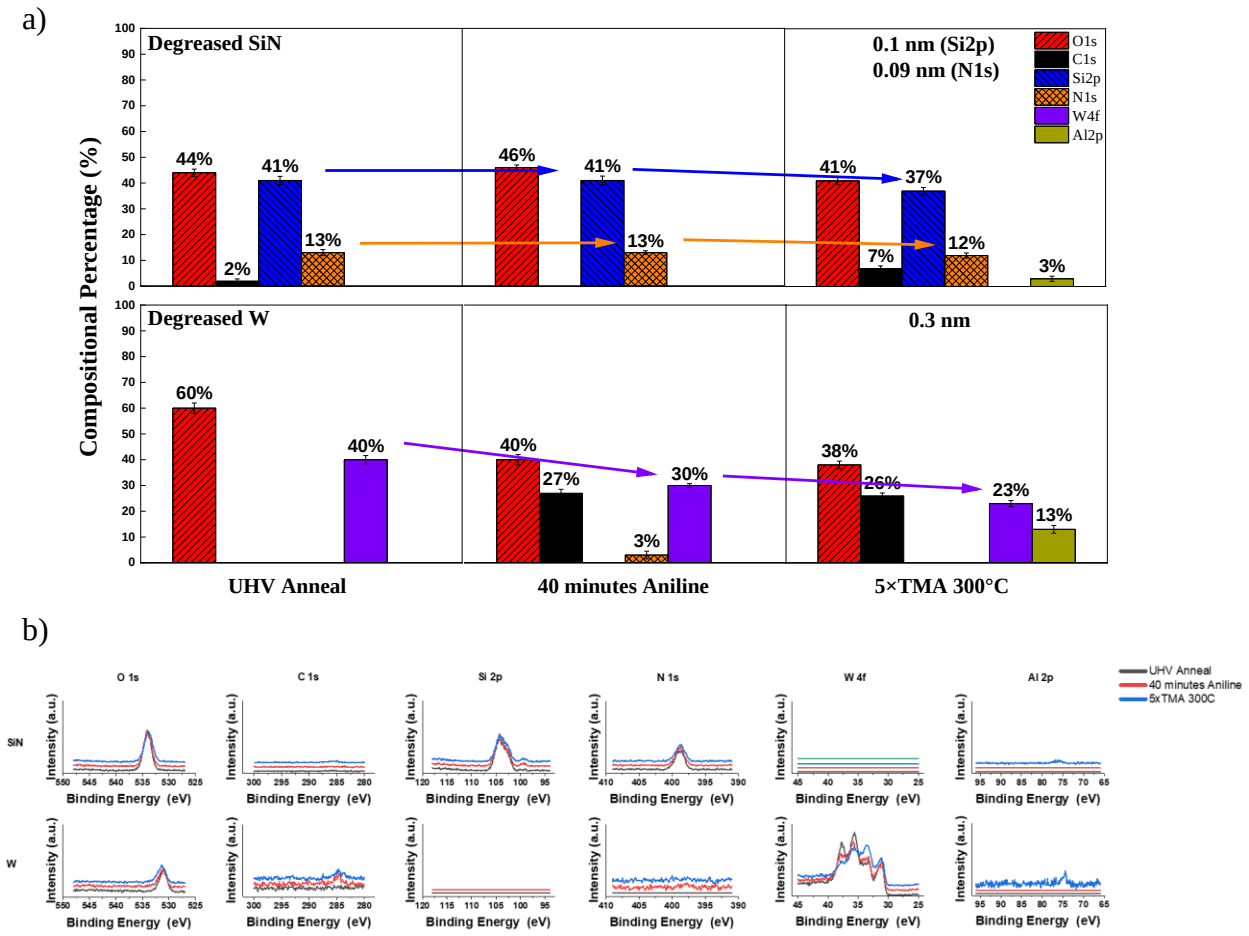

Figure 3.11. a) XPS showed aniline unable to passivate W against TMA dosing. b) XPS raw spectra.

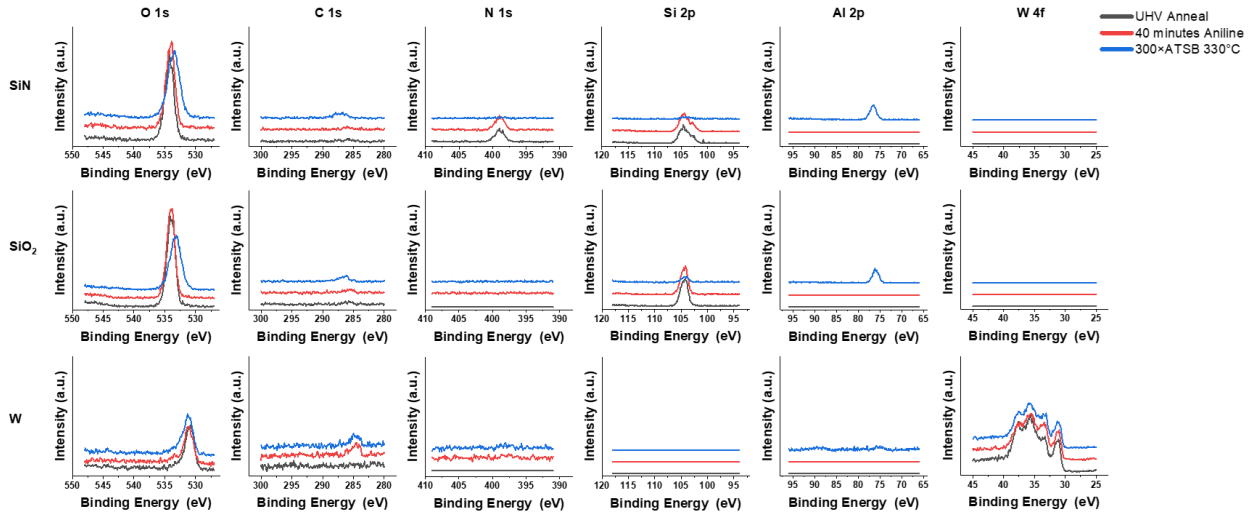

Figure 3.12. Raw XPS spectra of the AlO_x growth on aniline passivated SiO_2, SiN, and W.

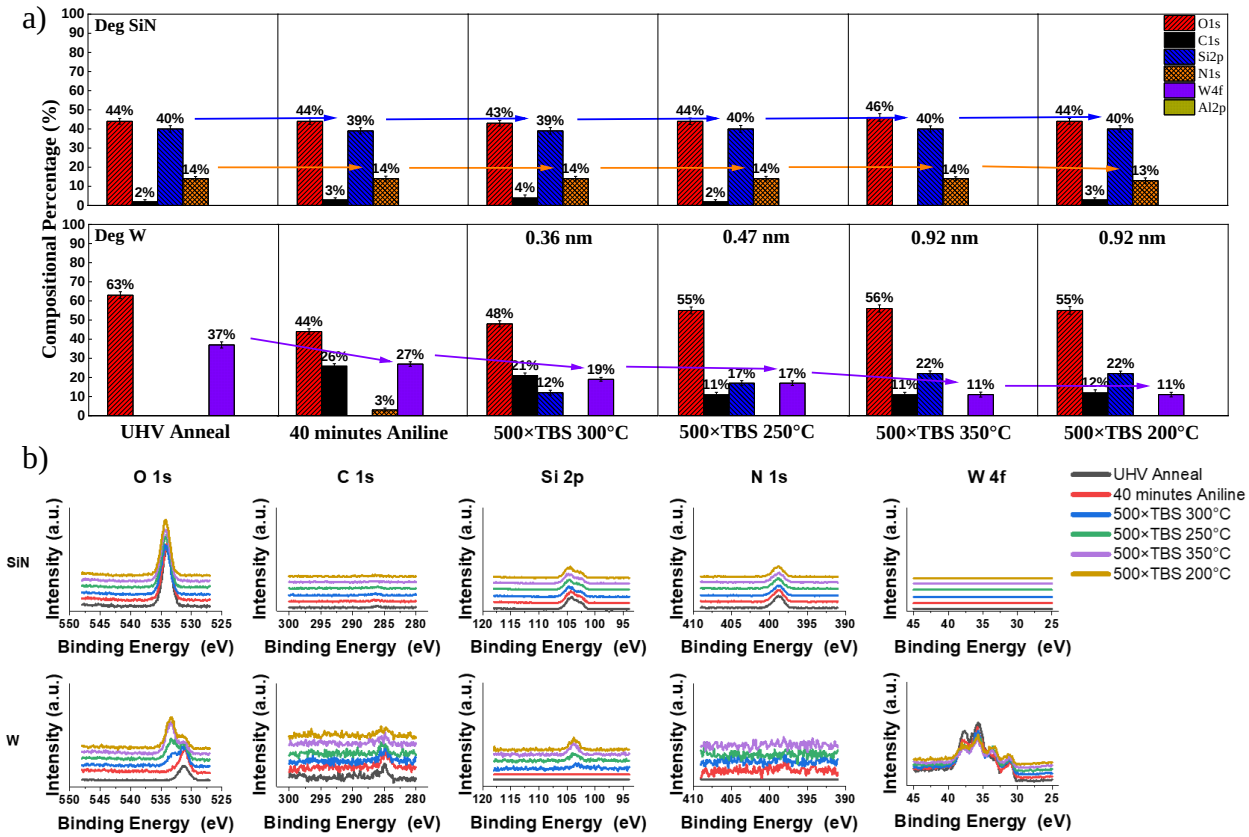

Figure 3.13. a) XPS composition analysis of the TBS reactivity test on SiN vs. aniline passivated W at various substrate temperature. b) Raw XPS spectra.

a)

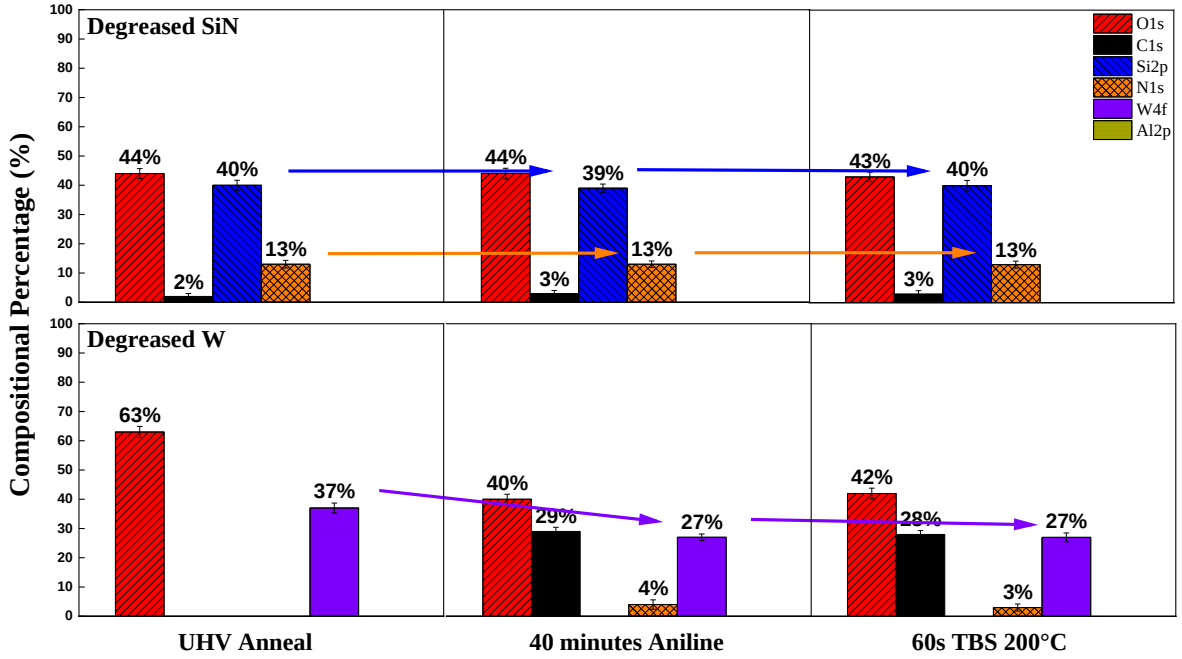

b)

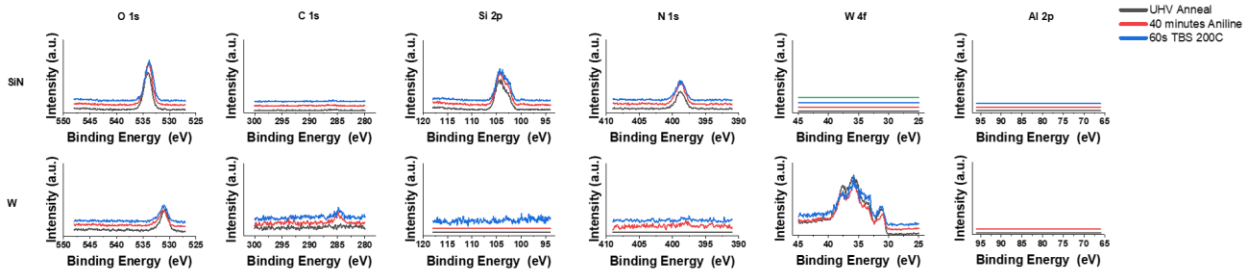

Figure 3.14. a) Reactivity study of 60-second TBS exposure on SiN and aniline passivated W at 200 °C. b) Raw XPS spectra.

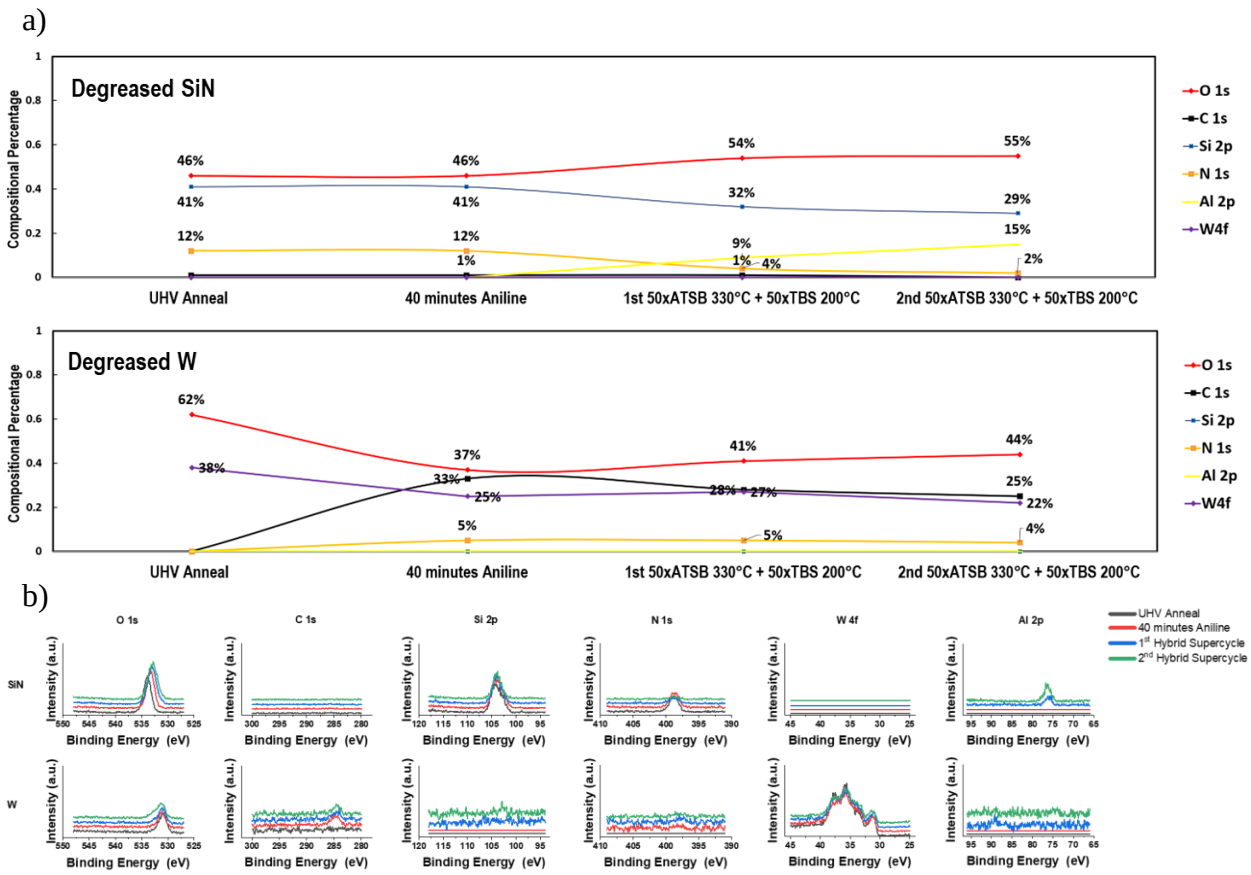

Figure 3.15. Scatter plot and raw XPS spectra of pulsed ATSB followed by pulsed TBS on SiN vs. aniline passivated W at binary substrate temperature.

a)

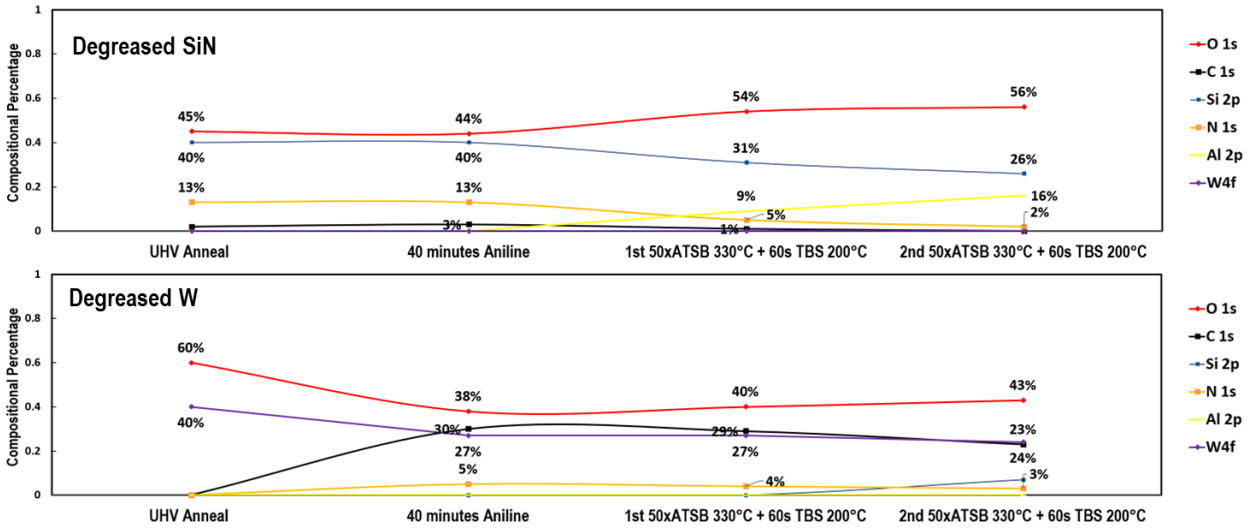

b)

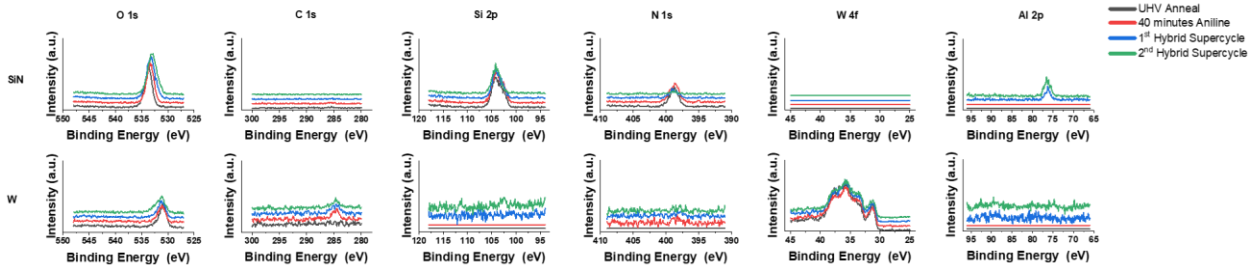

Figure 3.16. Scatter plot and raw XPS spectra of the pulsed ATSB followed by continuous TBS exposure on SiN vs. aniline passivated W at binary substrate temperature.

a)

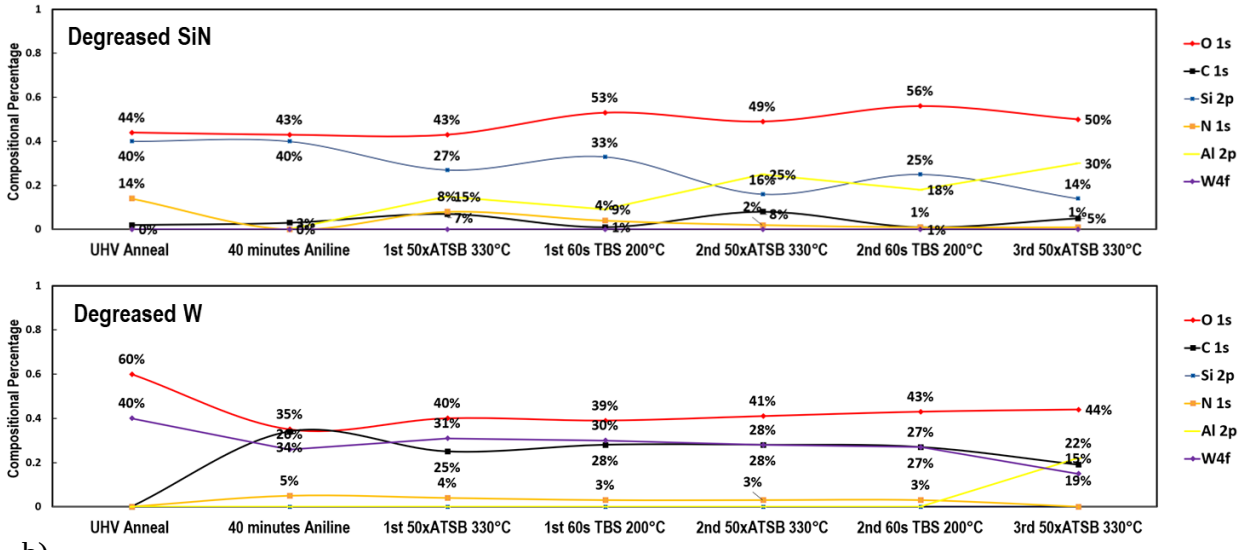

b)

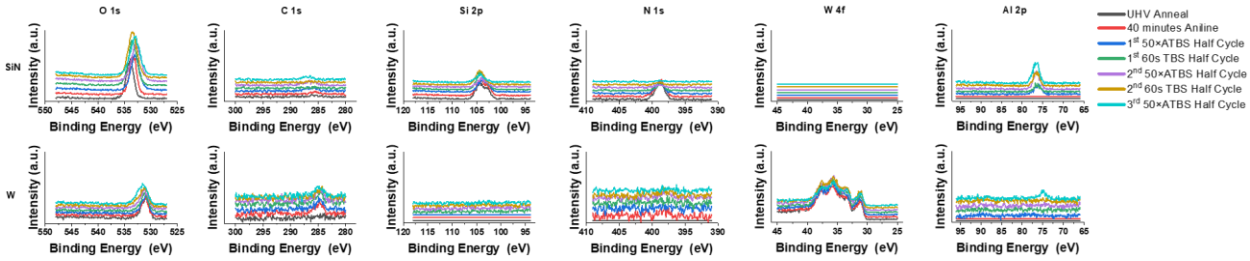

Figure 3.17. Scatter plot and raw XPS spectra of half-supercycle hybrid pulsed ATSB with half-supercycle continuous TBS exposure on SiN vs. aniline passivated W at binary substrate

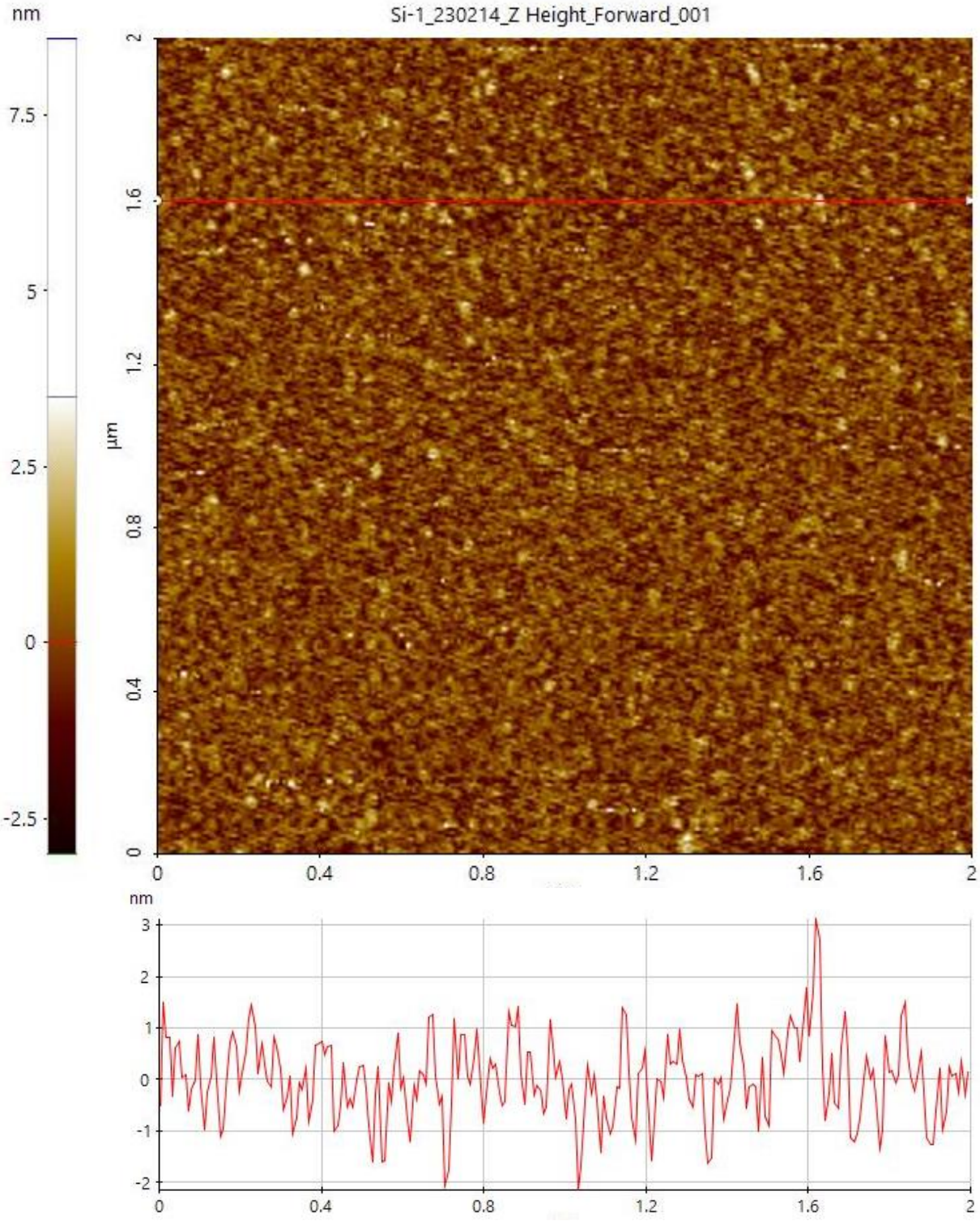

Figure 3.18. AFM measurement of the half-supercycle hybrid pulsed CVD sample shown in Fig. 6. AFM showed a smooth deposition surface with an RMS roughness of 0.81 nm.

a)

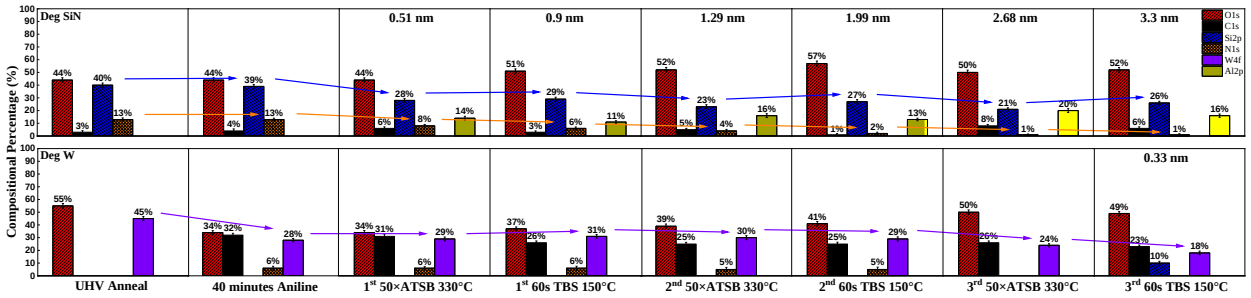

b)

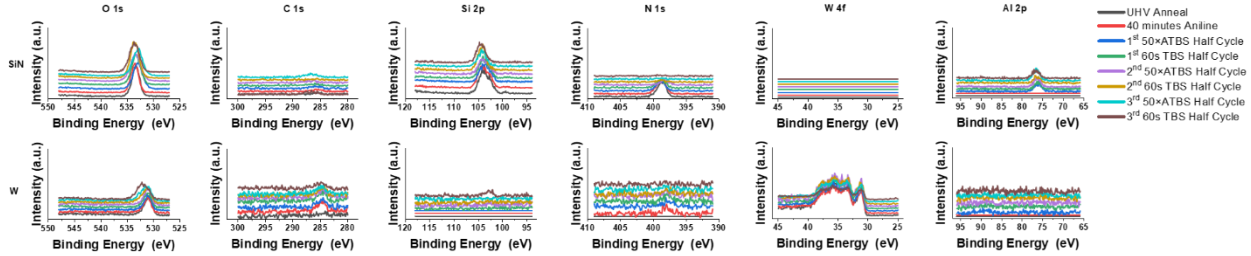

Figure 3.19. a) Selectivity study of half-supercycle hybrid pulsed CVD with TBS exposure at 150 °C. b) Raw XPS spectra.

a)

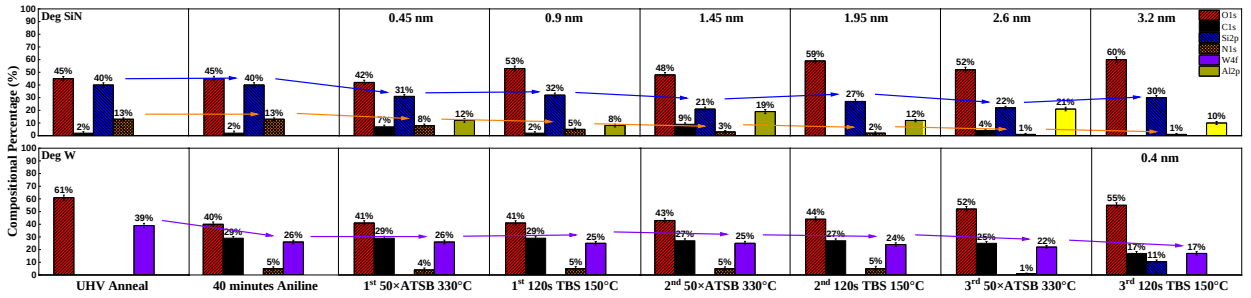

b)

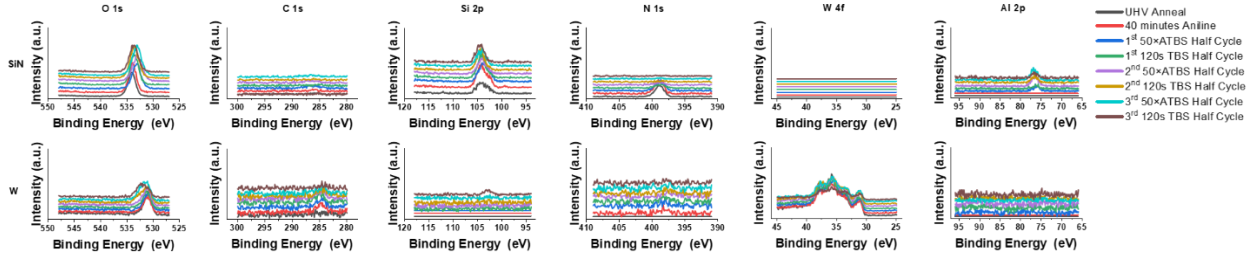

Figure 3.20. a) Selectivity study of half-supercycle hybrid pulsed CVD with 120-second TBS exposure at 150 °C. b) Raw XPS spectra.

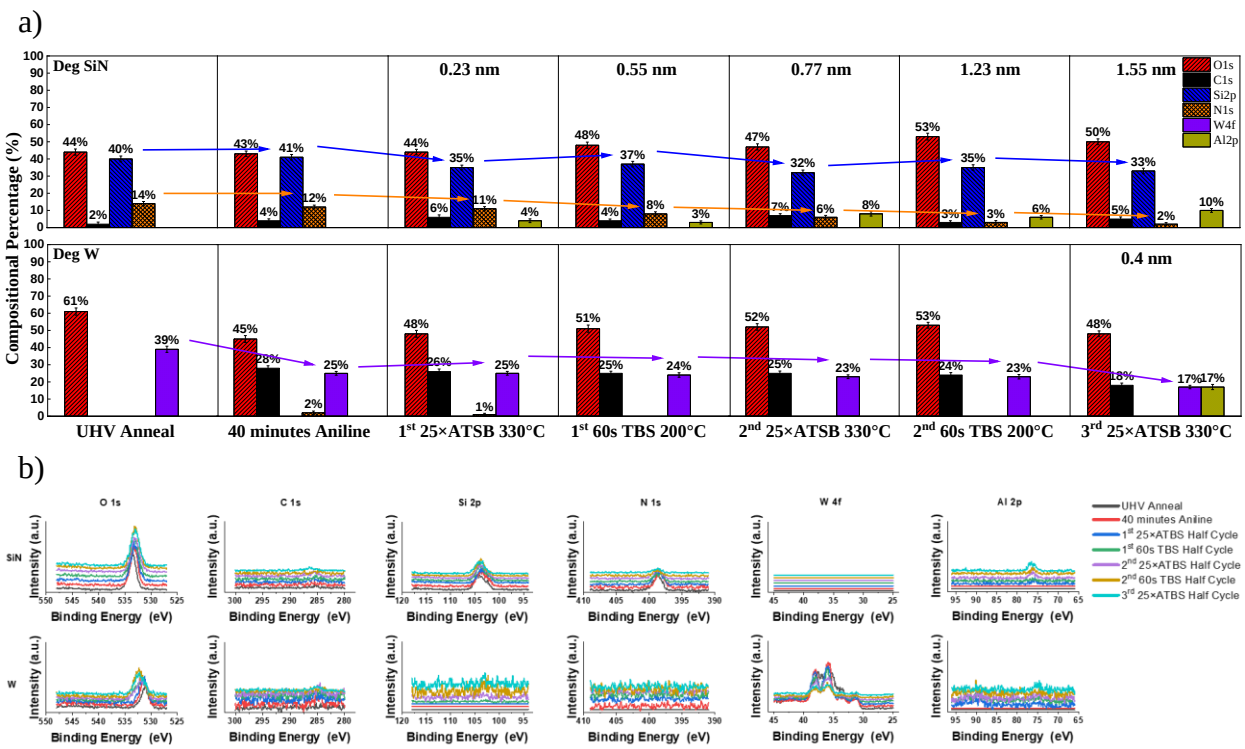

Figure 3.21. a) Selectivity study of half-supercycle hybrid pulsed CVD with 25 pulses of ATSB at 330 °C and 60-second TBS exposure at 200 °C. b) Raw XPS spectra.

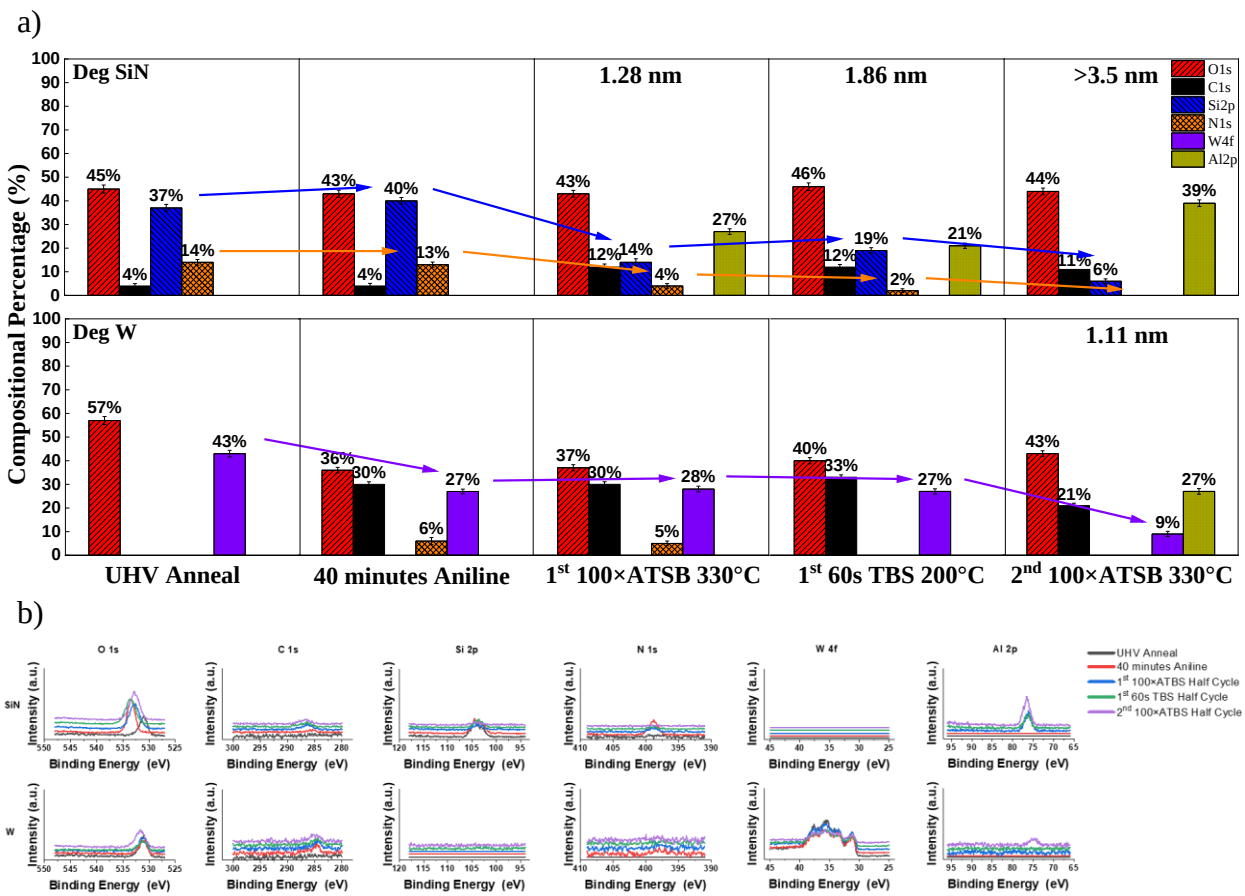

Figure 3.22. a) Selectivity study of half-supercycle hybrid pulsed CVD with 100 pulses of ATSB at 330 °C and 60-second TBS exposure at 200 °C. b) Raw XPS spectra.

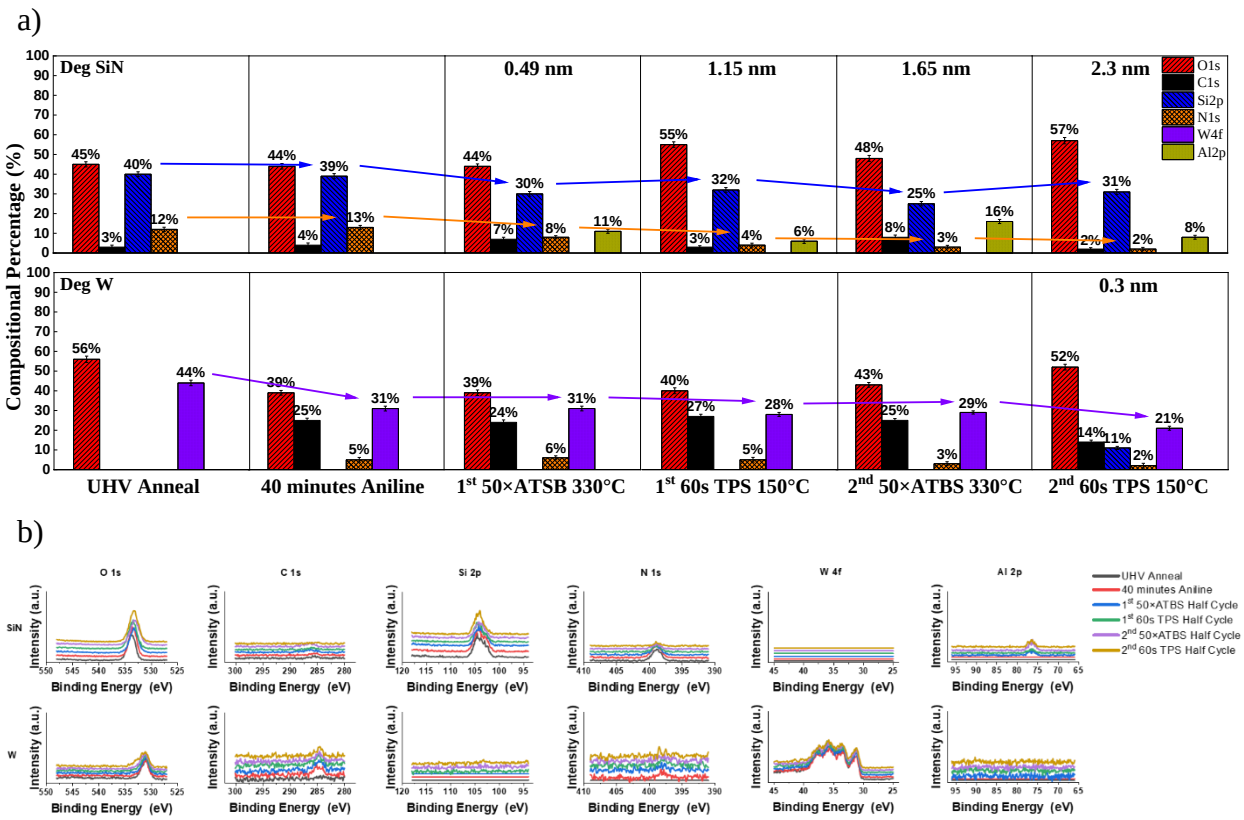

Figure 3.23. a) Selectivity study of half-supercycle hybrid pulsed CVD with 50 pulses of ATSB at 330 °C and 60-second TPS exposure at 150 °C. b) Raw XPS spectra.

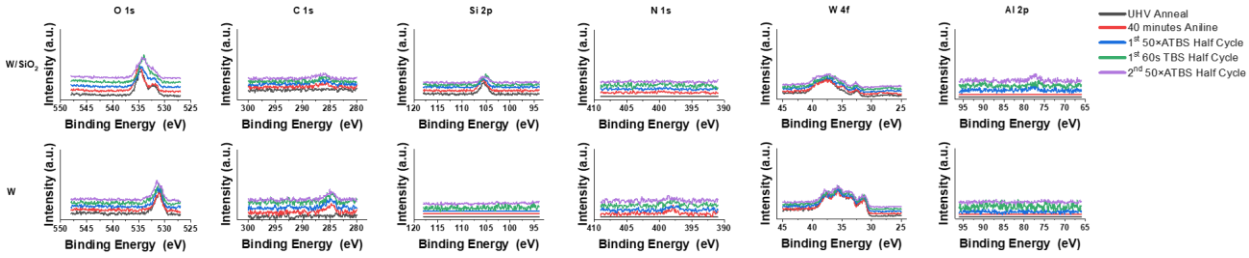

Figure 3.24. Raw XPS spectra of selective hybrid pulsed SiO_x/AlO_x CVD on SiO_2 region of W/SiO_2 patterned sample with aniline passivation.

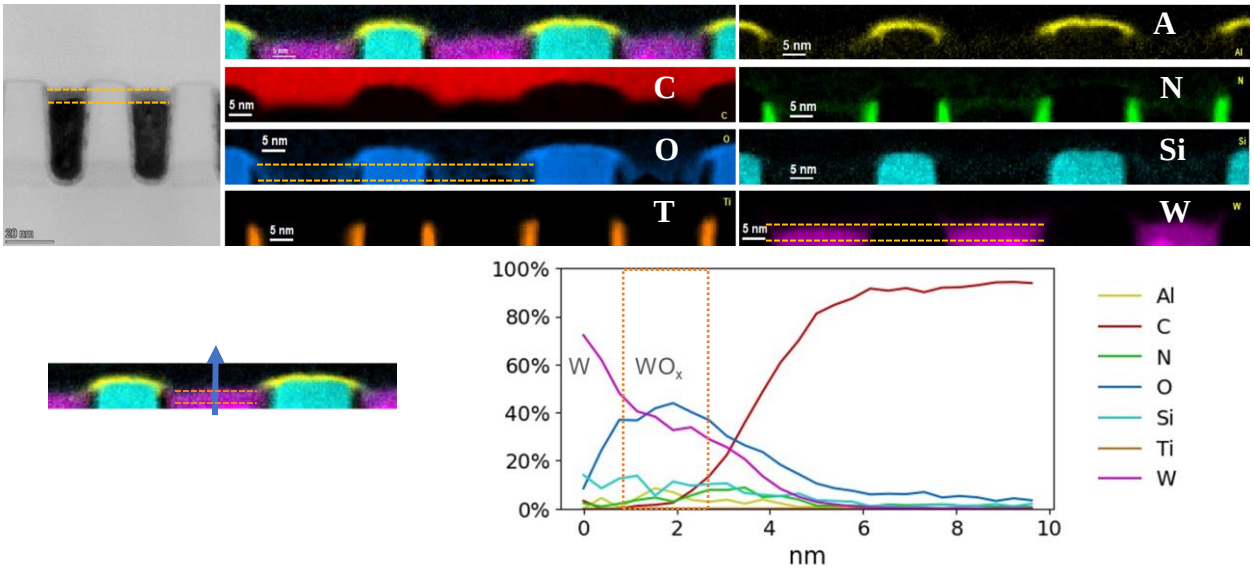

Figure 3.25. Electron energy loss spectroscopy (EELS) study of the W/SiO_2 patterned sample.

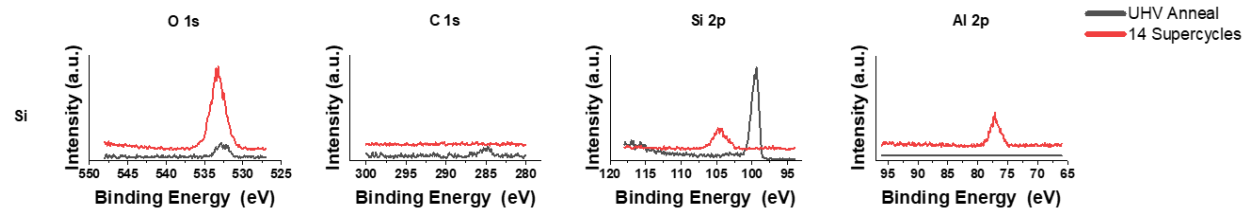

Figure 3.26. Raw XPS spectra of selective hybrid pulsed SiO_x/AlO_x CVD on Si for capacitance study.

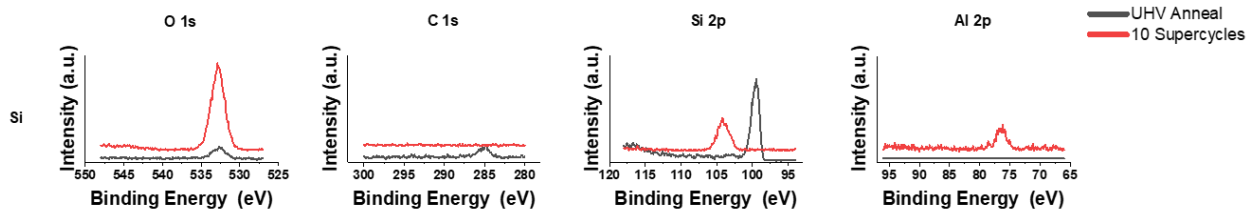

Figure 3.27. Raw XPS spectra of selective hybrid pulsed SiO_x/AlO_x CVD on Si for capacitance study with the 25 pulses of ATBS at 330 °C with 60-second TBS at 200 °C process.

a) b)

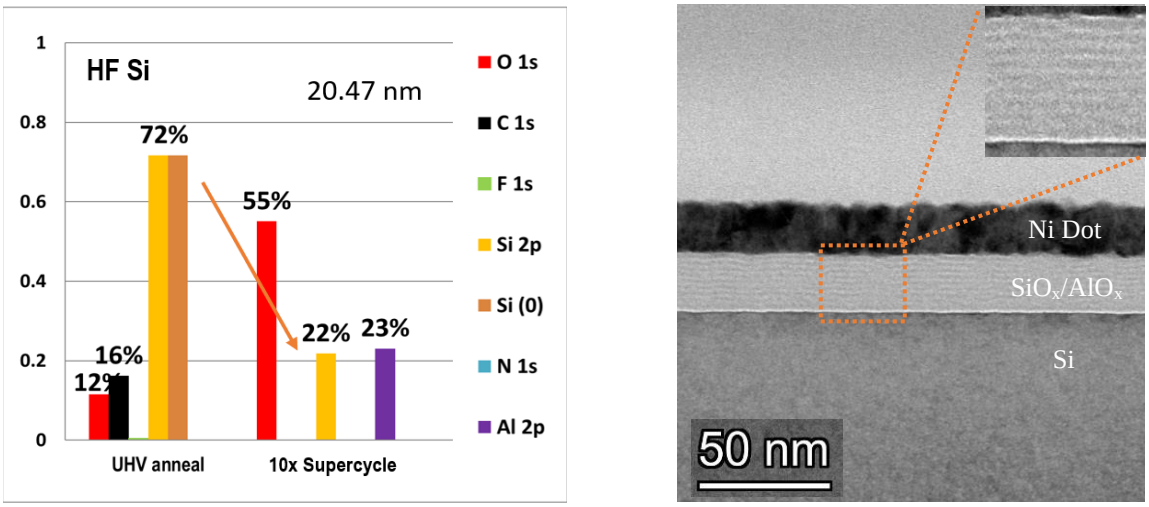

Figure 3.28. a) Selective hybrid pulsed SiO_x/AlO_x CVD on Si for capacitance study. 10 supercycles of 50 pulses of ATSB at 330 °C and a 60-second TBS dosing at 200 °C were employed. Thickness was measured by ellipsometry to be 20.47nm. b) TEM image proved similar thickness of SiO_x/AlO_x nanolaminate was deposited.

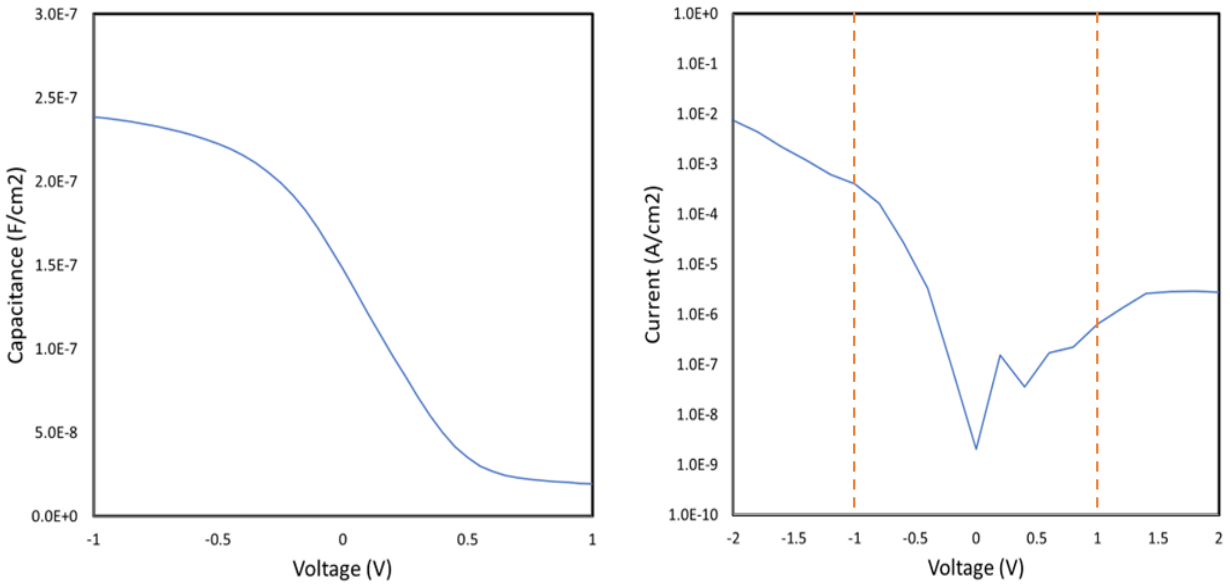

Figure 3.29. CV and IV remeasurement of the SiO_x/AlO_x (2:1) on Si with the 25 pulses of ATSB at 330 °C and a 60-second TBS dosing at 200 °C process after three days left in the atmospheric condition.

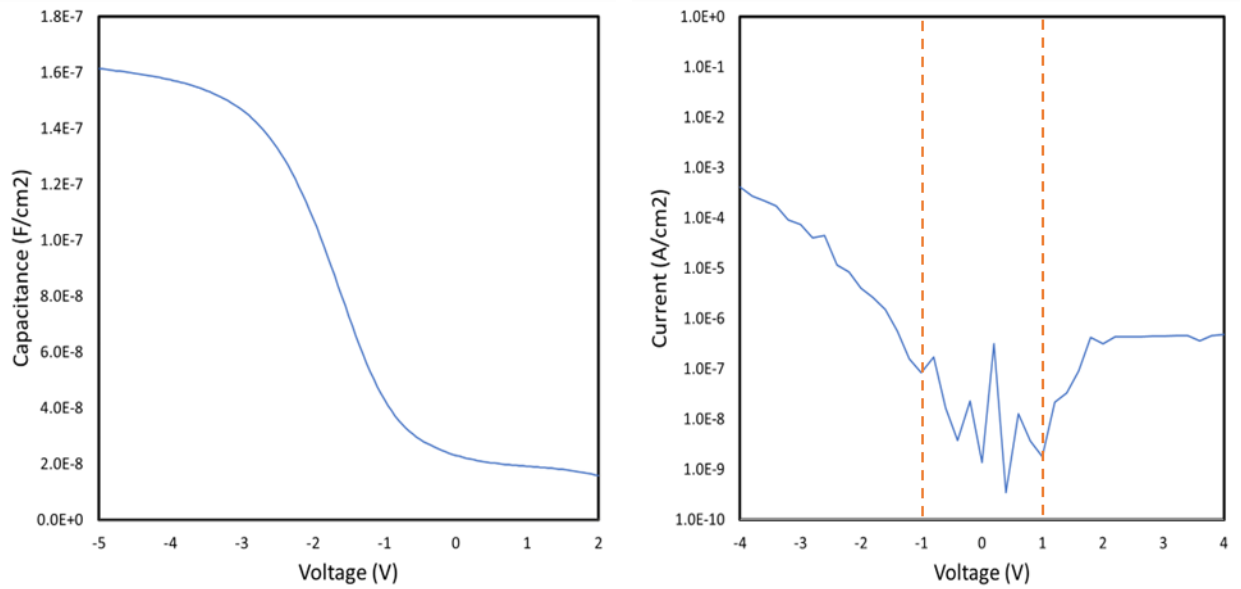

Figure 3.30. CV and IV remeasurement of the SiO_x/AlO_x (1:1) on Si with the 50 pulses of ATSB at 330 °C and a 60-second TBS dosing at 200 °C process after three days left in the atmospheric condition.

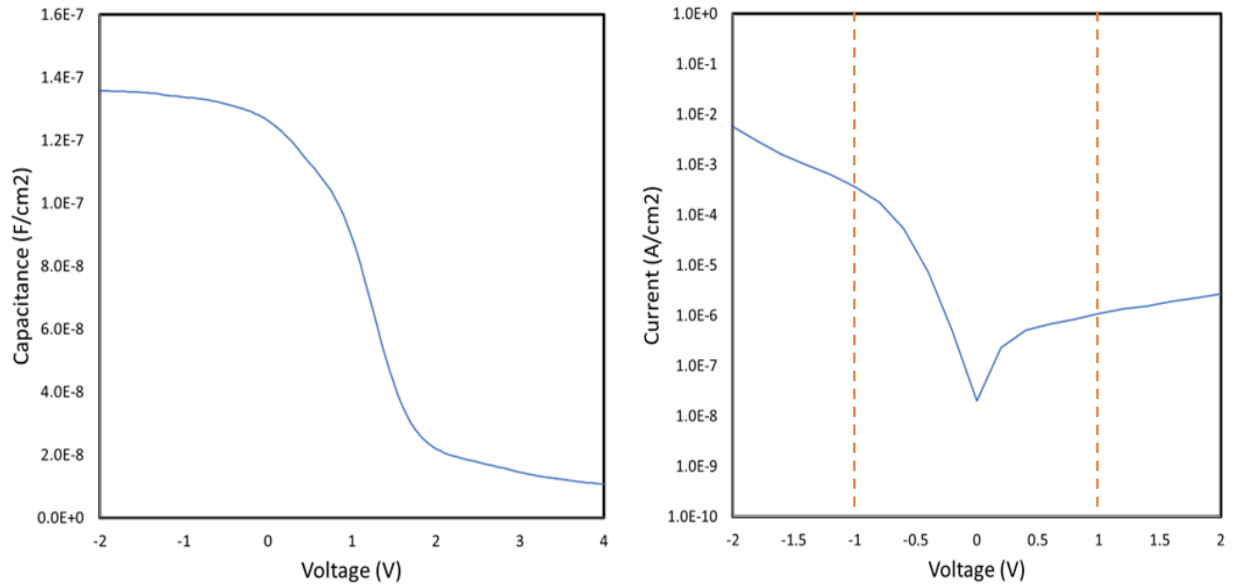

Figure 3.31. CV and IV remeasurement of the SiO_x/AlO_x (2:1) on Si with the 25 pulses of ATSB at 330 °C and a 60-second TBS dosing at 200 °C process right after additional UHV 300°C anneal.

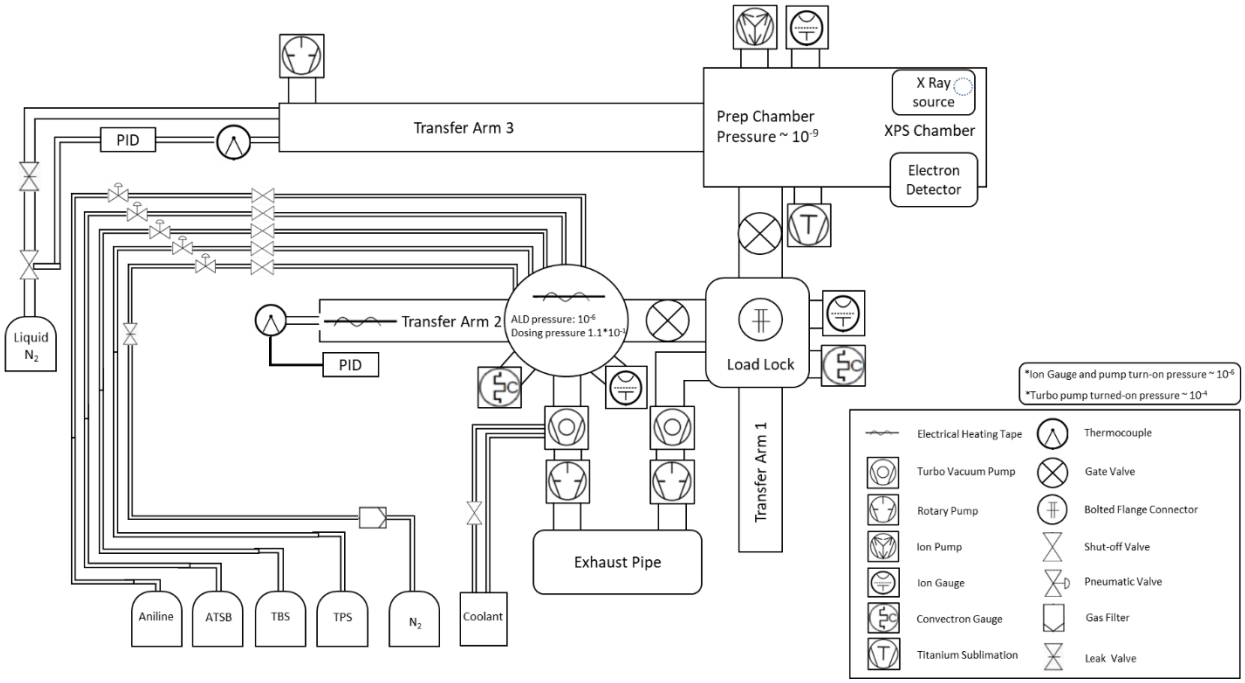

Figure 3.32. Schematic diagram illustrates the custom-built ALD/CVD with in-situ XPS system.

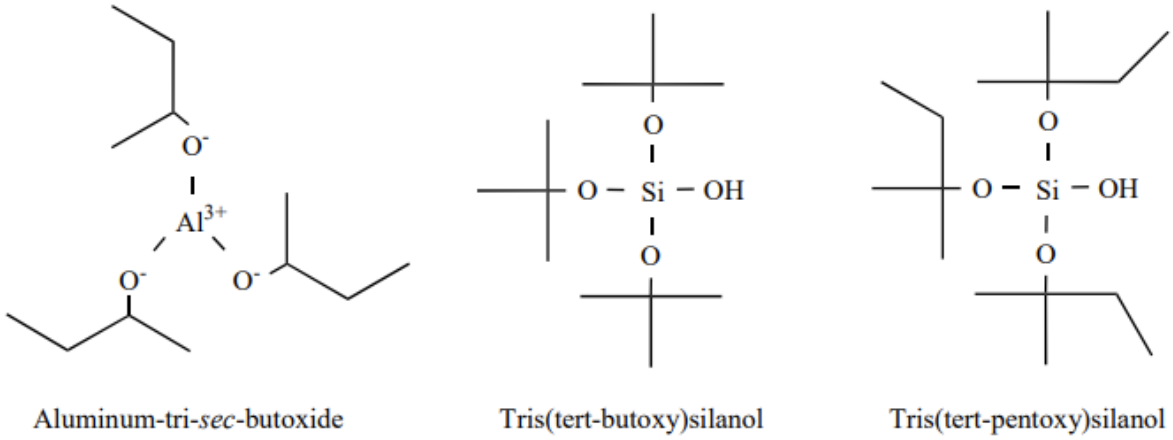

Figure 3.33. Chemical structures from left to right: Aluminum-tri-sec-butoxide (ATSB, 97%), tris(tert-butoxy)silanol (TBS, 99.999%), tris(tert-pentoxy)silanol (TPS, ≥99.99%).

3.6 References

1. Chen, H.; Wu, Y.; Huang, H.; Tsai, C.; Lee, S.; Lee, C.; Wei, T.; Yao, H.; Wang, Y.; Liao, C.; Chang, H.; Lu, C.; Shue, W.; Cao, M. Fully Self-Aligned Via Integration for Interconnect Scaling Beyond 3nm Node. *2021 IEEE International Electron Devices Meeting (IEDM)*, 2021, pp. 22.1.1-22.1.4, doi: 10.1109/IEDM19574.2021.9720600.

2. Hashemi, S. M.; Prasittichai, C.; Bent, S. (2014). A New Resist for Area Selective Atomic and Molecular Layer Deposition on Metal–Dielectric Patterns. The Journal of Physical Chemistry C, 118(20), 10957–10962. https://doi.org/10.1021/jp502669f.

3. Pasquali, M.; Gendt, S. D.; Armini, S. (2019). Area-Selective Deposition by A Combination of Organic Film Passivation and Atomic Layer Deposition. ECS Transactions, 92(3), 25–32. https://doi.org/10.1149/09203.0025ecst.

4. Liu, T. L.; Nardi, K. L.; Draeger, N.; Hausmann, D. M.; Bent, S. (2020). Effect of Multilayer Versus Monolayer Dodecanethiol on Selectivity and Pattern Integrity in Area-Selective Atomic Layer Deposition. ACS Applied Materials and Interfaces, 12(37), 42226–42235. https://doi.org/10.1021/acsami.0c08873.

5. Shearera, A.; Bent, S. (2022). Area-Selective Atomic Layer Deposition Using Nitrogenous Aromatic Small Molecule Inhibitors. ASD2022.

6. Merkx, M. J. M.; Vlaanderen, S.; Faraz, T.; Verheijen, M. A.; Kessels, W. M. M.; MacKus, A. J. M. (2020). Area-Selective Atomic Layer Deposition of TiN Using Aromatic Inhibitor Molecules for Metal/Dielectric Selectivity. Chemistry of Materials, 32(18), 7788–7795. https://doi.org/10.1021/acs.chemmater.0c02370.

7. Oszinda, T.; Schaller, M.; Schulz, S. E. (2010). Chemical Repair of Plasma Damaged Porous Ultra Low-K SiOCH Film Using a Vapor Phase Process. Journal of The Electrochemical Society, 157(12), H1140. https://doi.org/10.1149/1.3503596.

8. Huang, J., Cho, Y., Wang, V., Zhang, Z., Mu, J., Yadav, A., Wong, K., Nemani, S., Yieh, E., & Andrew, K. (2023). Dielectric-on-Dielectric Achieved on SiO_2 in Preference to W by Water-free Chemical Vapor Depositions with Aniline Passivation. *ACS Applied Materials & Interfaces*, *15*(21), 26128–26137. https://doi.org/10.1021/acsami.3c02278.

9. Cho, Y.; Huang, J.; Zhang, Z.; Wang, K.; Lee, P.; Kim, C.; Wong, K., Nemani, S.; Yieh, E.; Kummel, A. C. (2023). Inherent Selective Pulsed Chemical Vapor Deposition of Aluminum Oxide in nm Scale. Applied Surface Science, 622, 156824. https://doi.org/10.1016/j.apsusc.2023.156824.

10. Cho, Y.; Ahles, C. F.; Choi, J. Y.; Huang, J.; Jan, A.; Wong, K.; Nemani, S.; Yieh, E.; Kummel, A. C. (2022). Inherently Selective Water-Free Deposition of Titanium Dioxide on the Nanoscale: Implications for Nanoscale Patterning. ACS Applied Nano Materials, 5(1), 476–485. https://doi.org/10.1021/acsanm.1c03311.

11. Huang, J.; Cho, Y.; Zhang, Z.; Jan, A.; Wong, K. T.; Nemani, S. D.; Yieh, E.; Kummel, A. C. (2022). Selective Pulsed Chemical Vapor Deposition of Water-Free TiO2/Al2O3 and HfO2/Al2O3 Nanolaminates on Si and SiO_2 in Preference to SiCOH. ACS Applied Materials and Interfaces, 14(13), 15716–15727. https://doi.org/10.1021/acsami.1c19810.

12. Ovanesyan, R. A., Filatova, E. A., Elliott, S. D., Hausmann, D. M., Smith, D. C., & Agarwal, S. (2019). Atomic Layer Deposition of Silicon-Based Dielectrics for Semiconductor Manufacturing: Current Status and Future Outlook. *Journal of Vacuum Science & Technology A*, *37*(6), 060904. https://doi.org/10.1116/1.5113631.

13. Han, B., Zhang, Q., Wu, J., Han, B., Karwacki, E. J., Derecskei, A., Xiao, M., Lei, X., O'Neill, M. L., & Cheng, H. (2012). On the Mechanisms of SiO2 Thin-Film Growth by the Full Atomic Layer Deposition Process Using Bis(t-butylamino)silane on the Hydroxylated SiO_2 (001) Surface. *Journal of Physical Chemistry C*, *116*(1), 947–952. https://doi.org/10.1021/jp2094802.

14. Fang, G., Xu, L., Ma, J., & Li, A. (2016). Theoretical Understanding of the Reaction Mechanism of SiO_2 Atomic Layer Deposition. *Chemistry of Materials*, *28*(5), 1247–1255. https://doi.org/10.1021/acs.chemmater.5b04422.

15. Kim, D. H., Lee, H. J., Jeong, H., Shong, B., Kim, W. H., & Park, T. J. (2019). Thermal Atomic Layer Deposition of Device-Quality SiO_2 Thin Films under 100 °C Using an Aminodisilane Precursor. *Chemistry of Materials*, *31*(15), 5502–5508. https://doi.org/10.1021/acs.chemmater.9b01107.

16. Choi, D., Kim, B. K., Chung, K. B., & Park, J. S. (2012). Studies on Optical, Chemical, and Electrical Properties of Rapid SiO_2 Atomic Layer Deposition Using Tris(tert-butoxy)silanol and Trimethyl-aluminum. *Materials Research Bulletin*, *47*(10), 3004–3007. https://doi.org/10.1016/j.materresbull.2012.04.093.

17. Choi, D. W., Chung, K. B., & Park, J. S. (2013). Rapid Vapor Deposition SiO_2 Thin Film Deposited at a Low Temperature Using Tris(tert-pentoxy)silanol and Trimethyl-aluminum. *Materials Chemistry and Physics*, *142*(2–3), 614–618. https://doi.org/10.1016/j.matchemphys.2013.08.004.

18. Burton, B. B., Boleslawski, M. P., Desombre, A. T., & George, S. M. (2008). Rapid SiO_2 Atomic Layer Deposition Using Tris(tert-pentoxy)silanol. *Chemistry of Materials*, *20*(22), 7031–7043. https://doi.org/10.1021/cm801738z.

19. Fang, G., & Ma, J. (2013). Rapid Atomic Layer Deposition of Silica Nanolaminates: Synergistic Catalysis of Lewis/Brønsted Acid Sites and Interfacial Interactions. *Nanoscale*, *5*(23), 11856–11869. https://doi.org/10.1039/c3nr02086j.

20. Won, S. J., Kim, J. R., Suh, S., Lee, N. I., Hwang, C. S., & Kim, H. J. (2011). Effect of Catalyst Layer Density and Growth Temperature in Rapid Atomic Layer Deposition of Silica Using Tris(tert-pentoxy)silanol. *ACS Applied Materials and Interfaces*, *3*(5), 1633–1639. https://doi.org/10.1021/am200176j.

21. Tezsevin, I., F. W. Maas, J., J. M. Merkx, M., Lengers, R., M. M. Kessels, W., E. Sandoval, T., & J. M. Mackus, A. (2023). Computational Investigation of Precursor Blocking during

Area-Selective Atomic Layer Deposition Using Aniline as a Small-Molecule Inhibitor. *Langmuir*, *39*(12), 4265–4273. https://doi.org/10.1021/acs.langmuir.2c03214.

22. Leung, K., M. B. Nielsen, I., & J. Criscenti, L. (2009). Elucidating the Bimodal Acid−Base Behavior of the Water−Silica Interface from First Principles. *Journal of the American Chemical Society*, *131*(51), 18358–18365. https://doi.org/10.1021/ja906190t.

23. Ballinger, P., & A. Long, F. (2002). Acid Ionization Constants of Alcohols. II. Acidities of Some Substituted Methanols and Related Compounds1,2. *Journal of the American Chemical Society*, *82*(4), 795–798. https://doi.org/10.1021/ja01489a008.

24. Lingane, J. (1960). Treatise on Analytical Chemistry. Volume 1 of Part 1, Theory and Practice (Kolthoff, I. M.; Elving, Philip J.; Sandell, Ernest B.; eds.). *Journal of Chemical Education*, *37*(2). https://doi.org/10.1021/ed037p108.1.

25. Clark, A. (1932). Principles of Chemistry. Third edition (Hildebrand, Joel H.). *Journal of Chemical Education*, *9*(8). https://doi.org/10.1021/ed009p1495

Chapter 3, in full, is a reprint of the material which has been submitted to ACS Applied Materials & Interfaces for publication:

Huang, J., Mu, J., Cho, Y., Winter, C., Wang, V., Zhang, Z., Wang, K., Kim, C., Yadav, A., Wong, K., Nemani, S., Yieh, E., & Kummel, A. (2023). Low-k SiOx/AlOx Nanolaminate Dielectric on Dielectric Achieved by Hybrid Pulsed Chemical Vapor Deposition. *ACS Applied Materials & Interfaces*, *0*(0). https://doi.org/10.1021/acsami.3c13973

The dissertation author was the primary researcher and author of this paper.